THÈSE

Pour obtenir le grade de

DOCTEUR DE L'UNIVERSITÉ GRENOBLE ALPES

École doctorale : STEP - Sciences de la Terre de l'Environnement et des Planètes
Spécialité : Sciences de la Terre et de l'Environnement
Unité de recherche : Laboratoire des Ecoulements Géophysiques et Industriels

Evolution et développement des courants gravitaires en rotation

The Turbulent Life of Rotating Downslope Gravity Currents

Présentée par :

Sévan RETIF

Direction de thèse :

Maria Eletta NEGRETTI DIRECTRICE DE RECHERCHE, CNRS Délégation Alpes	Directrice de thèse
Achim WIRTH DIRECTEUR DE RECHERCHE, CNRS Délégation Alpes	Co-directeur de thèse

Rapporteurs :

Paul BILLANT
DIRECTEUR DE RECHERCHE, CNRS Délégation Ile-de-France Sud
Romain VOLK
MAITRE DE CONFERENCES HDR, ENS de Lyon

Thèse soutenue publiquement le **16 mars 2026**, devant le jury composé de :

Julien CHAUCHAT, DIRECTEUR DE RECHERCHE, INRAE Lyon-Grenoble Auvergne-Rhône-Alpes	Président
Maria Eletta NEGRETTI, DIRECTRICE DE RECHERCHE, CNRS Délégation Alpes	Directrice de thèse
Achim WIRTH, DIRECTEUR DE RECHERCHE, CNRS Délégation Alpes	Co-directeur de thèse
Paul BILLANT, DIRECTEUR DE RECHERCHE, CNRS Délégation Ile-de-France Sud	Rapporteur
Romain VOLK, MAITRE DE CONFERENCES HDR, ENS de Lyon	Rapporteur
Louis GOSTIAUX, CHARGE DE RECHERCHE, CNRS Délégation Rhône Auvergne	Examinateur
Annunziata PIRRO, SCIENTIST, Istituto Nazionale di Oceanografia e di Geofisica Sperimentale	Examinatrice

Remerciements

En premier lieu, j'aimerais sincèrement remercier Maria-Eletta Negretti et Achim Wirth, qui ont été respectivement ma directrice et mon co-directeur de thèse. Merci de m'avoir offert l'opportunité de travailler en dynamique des océans malgré mon manque d'expérience dans ce domaine. Merci également de m'avoir, à plusieurs reprises, poussé à participer à des communications ambitieuses autour de mon travail, que ce soit lors de conférences ou à travers nôtre publication.

Je tiens également à remercier les membres de mon jury de thèse d'avoir accepté de lire et d'évaluer mon manuscrit. Merci aussi pour la discussion passionnante et bienveillante qui a suivi la soutenance. Merci donc à Julien Chauchat, Annunziata Pirro, Louis Gostiaux, Romain Volk et Paul Billant.

Je remercie également les membres de mon CSI, Martin Obligado et David Cébron, qui ont toujours fait preuve de bienveillance lors de nos réunions. Merci pour vos précieux conseils.

Pour les nombreux badges égarés et autres soucis informatiques, je remercie sincèrement Gabriel Moreau et Olivier De Marchi pour leur réactivité ! Plus généralement, je remercie l'ensemble des services du LEGI de m'avoir épargné un grand nombre de procédures administratives et de m'avoir permis de vivre ces années de thèse avec beaucoup plus de sérénité.

Je remercie Nathanael Connesson, du DLST, pour cette première expérience d'enseignement dans le supérieur, qui a renforcé mon envie d'en faire mon métier. Plus particulièrement, merci à Guillaume Maitrejean ainsi qu'à tous les responsables d'enseignement de Polytech Grenoble de m'avoir offert l'opportunité d'enseigner pendant deux ans en tant qu'ATER. Un grand merci également à Cécile Darie, directrice de Polytech Grenoble, qui m'a beaucoup épaulé avant ma soutenance.

Merci à mes compagnon.nes doctorant · es pour tous ces moments de convivialité. Me faire jouer au football pendant quelque temps ne fut pourtant pas une mince affaire, tant mon appétence innée pour ce sport est... limitée ! Merci pour tous ces midis passés à la salle d'escalade, et merci à ceux qui m'ont initié à la coinche.

En particulier, merci à Axel Tassigny, mon co-bureau, avec qui j'ai partagé énormément de pauses café et que j'ai sollicité plus d'une fois lorsque certaines notions mathématiques de ma thèse dépassaient mes compétences... c'est-à-dire souvent ! Au plaisir de retourner sous terre avec toi et Thibault Leduc, grâce à qui j'ai particulièrement rentabilisé l'option "bris de glace" de mon assurance auto... espèce de chat noir ! Merci également à mes autres collègues qui m'ont particulièrement inspiré et conseillé, et avec lesquels j'ai pu partager mes nombreux moments de doute : Benjamin Arrondeau, Béatrice Janiaud, Ivan Ernesto Montero Siles. Et merci à Emmanuel, Narendra, Manuari, Jacobo, Félix, Romain... J'en oublie sûrement beaucoup d'autres !

Je ne serais sûrement pas allé au bout de cette aventure sans pouvoir m'épanouir dans

mes passions aux côtés de personnes qui ont littéralement bouleversé mon existence à des moments clés.

Je remercie donc Laurent Navaro et Rachel Hayat, d'Alpes ULM, de me donner l'opportunité d'assurer des baptêmes de l'air et donc de voler bien plus souvent que je n'aurais osé l'espérer ! Merci à David et Patrick pour nos discussions aéronautiques et vos conseils.

Aux antipodes de mon activité aérienne, le monde de la spéléologie a été une véritable soupape et m'apporte autant sur le plan sportif et exploration que sur le plan humain. Cette communauté est hors du commun, et je tenais à remercier tout particulièrement Dominique Frank ("Doumdoum") et Harry Lancaster, que je considère comme ma tata et mon tonton adoptifs de spéléo et qui m'inspirent énormément par leur humanité.

Je remercie également tous mes copains spéléos avec qui je partage d'innombrables aventures et que je considère comme de proches ami · es. Merci à Youen Taldu, Solveig Reymond, Léo Bouvier, Nolween Arribart, Johann Monnerie, Jeff Wade, Timothée Fuzeau, Louisa Jackob, Marie Chapard, Gilbert Chapard, Laurent Montagny, Rémy Limagne, Édouard Dessein, Léo Perrez, Augustin Madelène, Camille Bérenger, Clara Pierantoni... J'en oublie sûrement énormément !

Je remercie chaleureusement Stéphane Muh et Isabel De Santos Pilot pour tout ce qu'ils m'ont apporté à travers le théâtre. J'ai adoré me dépasser à vos côtés en travaillant des rôles qui m'ont profondément sorti de ma zone de confort. Merci d'avoir cru en moi et de m'avoir poussé à revenir après des périodes difficiles qui m'avaient conduit à presque abandonner.

Je veux aussi remercier mes ami · es de Grenoble ainsi que mes vieux ami · es de Paris, qui m'ont toujours soutenu et ont été d'un réconfort salvateur dans les moments les plus compliqués. Merci Samuel Benhamou, Esther Marand, Ardelia Ferlat (et Yuka!!), Alix Faguel, Claire Izedine, Meryem Dogan. Merci à Mr Kananjo pour nos jam sessions. Merci à Vince, Dirty, Sasa T1000, Ruda, Piwate... et aux Pas (trop) Relous des Catacombes!

Enfin, je remercie mes deux mamans. Aline Manoukian, qui m'a donné la vie, qui m'a fait confiance et qui m'a toujours laissé expérimenter et apprendre de mes erreurs par moi-même. Marion Moulin, qui a su me recadrer à des moments clés de mon existence et qui m'a permis d'acquérir un minimum de rigueur pour affronter le monde de fous dans lequel je dois faire mon bonhomme de chemin. Merci à mon père, Paul Rétif, de m'avoir toujours laissé rêver et d'avoir pris le temps de répondre à mes nombreuses questions sans jamais les minimiser. J'apprécie énormément que tu m'aies toujours parlé comme à un adulte ; cela m'a aidé à me sentir rapidement responsable de mes pensées et de mes actions. Merci à vous trois de m'avoir transmis la curiosité, l'amour des arts, la compassion, l'ouverture d'esprit, la capacité d'adaptation et cette pointe de naïveté qui permet de garder foi en la vie dans bien des circonstances. Merci pour votre folie! Merci, tonton Jean-Marie, de m'avoir transmis une partie de ton amour inconditionnel pour la physique. Merci, tonton François, de m'avoir donné envie de devenir aviateur.

Enfin, merci à Renato Guilardi, toi, le maçon qui m'a enseigné l'art du pilotage. Ton souvenir m'accompagne très souvent, et j'essaie d'appliquer tes conseils dans ma vie du mieux que je peux : oser jouer avec les filets d'air tout en gardant toujours assez d'eau sous la quille.

Abstract

Studying the dynamics of rotating downslope gravity currents and their interaction with stratified environments is essential for understanding their influence on the large-scale ocean structure and circulation. The large-scale laboratory experiments conducted in the Coriolis Rotating Platform made it possible to reproduce these dynamics in a controlled environment, while simultaneously measuring (i) the vertical density structure using a conductivity probe, (ii) the three-dimensional velocity field near the slope using an Acoustic Doppler Velocimetry Profiler (ADVP), and (iii) the horizontal velocity field over the full domain using Particle Image Velocimetry (PIV).

A first part of this work focused on the intrusion of dense gravity currents into a two-layer stratified ambient. Density and velocity measurements collected in the central deep area show that, once detached from the slope, the current undergoes no significant interior mixing. The vertical density structure reveals two distinct intrusion regimes: a laminar regime, governed by Ekman dynamics, and a turbulent regime, associated with intermittent dense-water cascades. In turbulent cases, vertical density gradients display a piecewise-linear dependence on the density anomaly, consistent with the underlying advection–diffusion balance from Munk and Wunsch 1998[65], and producing an exponential intrusion profile. From the exponential solutions, an e-folding scale height is defined. An analytical model based on a critical Froude number of about $F \approx 0.8$ accurately predicts this scale height over more than three decades of Rossby number, with the total intrusion thickness averaging 2.5 times this value. In laminar cases, the scale height formally diverges, yet the intrusion thickness remains only a few times the Ekman layer thickness. Several independent criteria, based on vorticity, local density-gradient plateaus, and a Peclet number, provide consistent identification of laminar versus turbulent intrusions.

The second part of this work examines the Ekman boundary layer (EBL) formed by rotating downslope gravity currents, where buoyancy, Coriolis acceleration, and viscosity jointly control the near-bottom flow. Velocity profiles recorded by the ADVP display clear Ekman spirals. To quantify the EBL, three independent methods were used to estimate its thickness δ_{Ek}: one based on velocity fluctuations, one based on azimuthal velocity maxima, and one based on higher-order derivatives. All methods yield consistent orders of magnitude and confirm that the EBL thickness generally aligns with laminar Ekman theory. A turbulent viscosity ν_t inferred from measured δ_{Ek} gives $\nu_t \approx 5\nu$, using the fluctuation-based method, $\nu = 10^{-6}\,\mathrm{m^2\,s^{-1}}$ being the molecular water viscosity, $\nu_t \approx 0.5\nu$ from velocity extrema, and $\nu_t \approx \nu$ from the derivative-based method. Finally, the measurements confirm that the friction velocity follows the scaling $V/u^* \propto \sqrt{Re_\delta}$, supporting the theoretical law proposed by Sous et al. 2013[95].

Résumé

Étudier la dynamique des courants gravitaires sur pente et en rotation, et leur interaction avec des environnements stratifiés est essentiel pour comprendre leur influence sur la structure et la circulation à grande échelle de l'océan. Les expériences menées sur la Plateforme Rotative Coriolis ont permis de reproduire ces dynamiques dans un environnement contrôlé, tout en mesurant simultanément (i) la structure verticale de densité à l'aide d'une sonde de conductivité, (ii) le champ de vitesse tridimensionnel près de la pente à l'aide d'un profileur de vitesse acoustique par effet Doppler (ADVP), et (iii) le champ de vitesse horizontal sur l'ensemble du domaine à l'aide de vélocimétrie par images de particules (PIV).

Une première partie de ce travail s'est concentrée sur l'intrusion de ces courants de gravité en rotation dans un environnement stratifié bi-couches. Les mesures de densité et de vitesse recueillies dans la zone profonde centrale montrent qu'une fois détaché de la pente, le courant ne subit presque aucun mélange avec l'eau environante. La structure verticale de densité révèle deux régimes d'intrusion distincts : un régime laminaire, gouverné par la dynamique d'Ekman, et un régime turbulent, associé à des cascades intermittentes d'eau dense. Dans les cas turbulents, les gradients verticaux de densité présentent une dépendance linéaire par morceaux à l'anomalie de densité, cohérente avec l'équilibre advection–diffusion sous-jacent décrit par Munk et Wunsch 1998[65], et produisant un profil d'intrusion exponentiel. À partir des solutions exponentielles, une épaisseur charactéristique est définie. Un modèle analytique basé sur un nombre de Froude critique d'environ $F \approx 0.8$ prédit avec précision cette épaisseur sur plus de trois décades du nombre de Rossby, l'épaisseur réelle de l'intrusion étant en moyenne 2.5 fois cette valeur. Dans les cas laminaires, l'épaisseur charactéristique diverge formellement, mais l'épaisseur de l'intrusion reste de seulement quelques fois l'épaisseur de la couche d'Ekman. Plusieurs critères indépendants, basés sur la vorticité, des plateaux locaux du gradient de densité, et un nombre de Péclet, fournissent une identification cohérente des intrusions laminaires versus turbulentes.

La seconde partie de ce travail examine la Couche Limite d'Ekman (CLE) formée par les courants gravitaires descendants une pente en rotation, où la flottabilité, l'accélération de Coriolis et la viscosité contrôlent conjointement l'écoulement proche du fond. Les profils de vitesse enregistrés par l'ADVP présentent des spirales d'Ekman nettes. Pour quantifier la CLE, trois méthodes indépendantes ont été utilisées pour estimer son épaisseur δ_{Ek} : une basée sur les fluctuations de vitesse, une basée sur les maximum locaux de vitesse azimutale, et une basée sur des dérivées d'ordre supérieur. Toutes les méthodes donnent des ordres de grandeur cohérents et confirment que l'épaisseur de l'CLE s'aligne généralement avec la théorie laminaire d'Ekman. Une viscosité turbulente ν_t déduite de la δ_{Ek} mesurée donne $\nu_t \approx 5\nu$ en utilisant la méthode basée sur les fluctuations, $\nu = 10^{-6}\,\mathrm{m^2\,s^{-1}}$ étant la viscosité moléculaire de l'eau, $\nu_t \approx 0.5\nu$ à partir des extrema de vitesse, et $\nu_t \approx \nu$ à partir de la méthode basée sur les dérivées. Enfin, les mesures confirment que la vitesse de frottement suit le comportement $V/u^* \propto \sqrt{Re_\delta}$, soutenant la loi théorique proposée par Sous et al. 2013[95].

Contents

Remerciements **iii**

1 Introduction **1**
1.1 Context . . . 1
1.2 Impact of dense overflows on climate system . . . 2

2 Preliminary concepts **5**
2.1 Introduction . . . 5
2.2 A stratified and rotating environment . . . 5
2.2.1 Stratification . . . 5
2.2.2 Rotational Effects . . . 6
2.3 Few words about ocean dynamics . . . 7
2.3.1 From rotating Navier-Stokes to Shallow Water equations . . . 7
2.3.2 Frictional effects and rotation: the Ekman layer . . . 9
2.3.3 Large scale circulation systems . . . 12
2.3.4 Ocean observation technics . . . 14

3 Gravity Currents (Literature Review) **19**
3.1 Observations . . . 19
3.1.1 Mediterranean Outflow . . . 19
3.1.2 Denmark Strait Overflow DSO . . . 22
3.1.3 Weddell sea . . . 24
3.1.4 Other sites around the world . . . 25
3.2 Physical insight of ocean Gravity Currents . . . 27
3.2.1 The non-rotating lock-exchange experiment . . . 27
3.2.2 A main geostrophic current . . . 28
3.2.3 Intrusion . . . 35
3.2.4 Mixing . . . 37

4 Experimental method and data processing **41**
4.1 The role of experimental studies . . . 41
4.2 The TUBE Experiment . . . 42
4.2.1 The Coriolis Platform . . . 42
4.2.2 Experimental set up . . . 43

4.3 Experimental measurement techniques 44
4.3.1 Conductivity probe for density measurements 44
4.3.2 The Acoustic Doppler Velocimetry profiler (ADVP) 46
4.3.3 Particle Image Velocimetry (PIV) 48
4.4 Experiments and their characteristics 50
4.4.1 Experimental parameters 50
4.4.2 Derived parameters 52
4.4.3 Dimensionless parameters 52

5 Density Structure of Gravity Currents Intrusions 55
5.1 Two regimes of intrusion 55
5.1.1 First observation 55
5.1.2 Model for the vertical density profile 56
5.1.3 Detection of Laminar and Turbulent intrusions 58
5.2 Predicting the thickness of turbulent intrusions 60
5.3 Richardson number analysis in the central area 62
5.4 Conclusions 65

6 Determining the Ekman-layer thickness 67
6.1 Introduction 67
6.2 Experiments 69
6.3 Results 69
6.3.1 Near-slope vertical velocity profiles 69
6.3.2 Estimation of the Ekman layer thickness 71
6.3.3 A measure of the Ekman layer thickness 75
6.4 Discussion and Conclusions 80

7 General conclusion and perspectives 83
7.1 Conclusions 83
7.2 Perspectives 84

8 Appendix 87
8.1 A) Numerical error from Method 3. 87
8.2 B) Predicting the vertical density structure of oceanic gravity current intrusions 88

Chapter 1

Introduction

1.1 Context

The Earth's climate system is composed of interconnected components. This complex system is primarily powered by the sun but is also influenced by geothermal energy: heat and pressure generated by radioactive reactions near the Earth's core shape the lithosphere, which interacts with both the atmosphere and the oceans, while solar radiation heats the atmosphere directly or indirectly through the warmed surface. Because solar heating is unequally distributed across the Earth's surface, temperature gradients arise and drive large-scale convective circulations within the atmosphere. Moreover, near the poles, the freezing and melting processes of the cryosphere generate additional gradients, particularly within the ocean, which is warmer near the equator. Alongside these feedback interactions, the biosphere and the ocean regulate greenhouse gases that trap heat in the atmosphere. This delicate equilibrium is strongly affected by human activity within the anthroposphere. For example, burning fossil fuels and deforestation release greenhouse gases that enhance atmospheric heat retention, thus intensifying global warming.

The world ocean acts as an immense heat reservoir, exchanging energy and matter with both the atmosphere and the cryosphere through the sea surface. These interactions lead to pronounced spatial inhomogeneities in temperature, salinity, and density, as illustrated in fig. 1.1.

The surface density map in fig. 1.1 reveals gradients. In polar regions, sea ice formation increases salinity; combined with low temperatures, this yields high surface densities ($\geq 1027\,\mathrm{kg\,m^{-3}}$). In contrast, equatorial regions are warm and experience high rainfall, resulting in less dense surface waters ($\leq 1023\,\mathrm{kg\,m^{-3}}$). Localised density gradients are also visible. For instance, a marked contrast exists between the Mediterranean Sea and the Atlantic Ocean: the hot, dry Mediterranean climate enhances evaporation, producing saltier and denser water. This semi-enclosed sea is connected to the Atlantic through a narrow strait, restricting exchange. A similar process occurs in the Red Sea and the Persian Gulf, which exchange dense, saline water with the Indian Ocean.

Large-scale density gradients drive one of the principal global ocean circulation systems, the Thermohaline Circulation (THC), so named because it depends on both temperature and salinity differences. The THC ventilates the deep ocean, transporting heat, salt, and nutrients on a characteristic timescale of roughly a thousand years. Smaller-scale density contrasts also drive water exchange processes, such as the Mediterranean outflow into the North Atlantic. Dense waters formed in polar or marginal seas participate in regional convective and overflow processes. For example, dense Mediterranean waters overflow into the

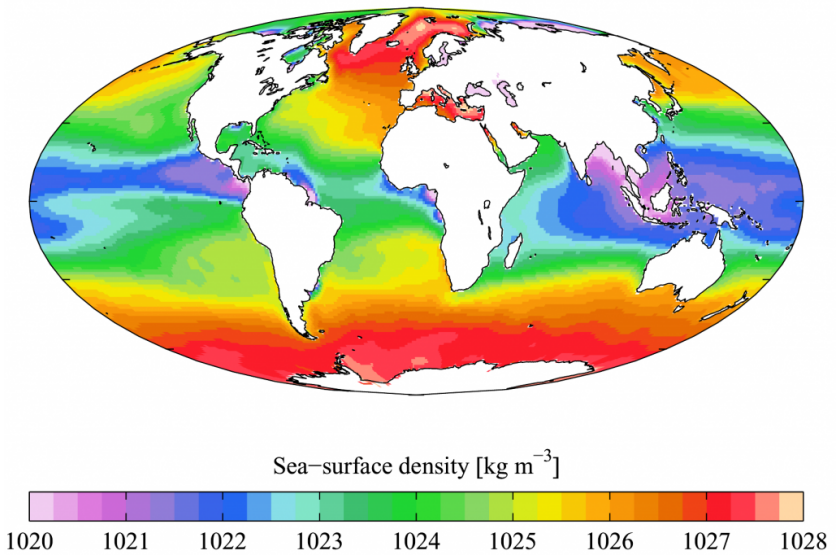

Figure 1.1: Global sea surface density. Higher densities are observed in colder polar regions compared to the warmer tropical zones. Adapted from original work by Plumbago [CC BY-SA 3.0 or GFDL], via Wikipedia Commons.

North Atlantic through the Strait of Gibraltar, and dense water masses from the Nordic Seas flow through the Denmark Strait Overflows. These smaller-scale processes strongly influence the structure and circulation of the global ocean.

Such localised dense overflows are commonly observed, and the most significant examples are reviewed in the following chapter. The present study focuses on the behaviour of dense water masses flowing downslope over topography, and their interaction with the ambient fluid before intruding into deeper ocean layers. Special attention is given to cases where these gravity currents evolve on time-scales of several days and are therefore affected by the Earth's rotation. The next section presents evidence of the profound influence of rotating oceanic gravity currents on the climate system.

1.2 Impact of dense overflows on climate system

The IPCC (Intergovernmental Panel on Climate Change) reports are comprehensive scientific assessments synthesising the latest research on climate change. Each assessment cycle, approximately 5–7 years, consists of three working-group reports produced by leading scientists worldwide: Working Group I: The Physical Science Basis; Working Group II: Impacts, Adaptation and Vulnerability; and Working Group III: Mitigation of Climate Change. A synthesis report is also produced to inform policymakers and the public on the current state of the climate. The latest edition, the Sixth Assessment Report (AR6), was released in 2023. In Chapter 9, *Ocean, Cryosphere and Sea Level Change* [72], the report highlights how these interconnected systems respond to climate change and the potential consequences for global climate stability, ecosystems, and human societies. This ocean-oriented chapter refers multiple times to "overflows", and emphasises their contribution to the climate system.

As the ocean constitutes a major component of the Earth's energy reservoir, the increasing Ocean Heat Content (OHC) strongly affects the planet's overall energy balance (Bindoff et al. 2019[4]). Focusing on ocean heat transfers, recent meta-analyses highlight the role of

Antarctic Bottom Water (AABW) and North Atlantic Deep Water (NADW) in maintaining the global Thermohaline Circulation (THC), and point to their ongoing warming (Purkey et al. 2019[81]). Indeed, the Atlantic Meridional Overturning Circulation (AMOC), which represents the global conveyor belt of the THC (see section *THC*), drives warm surface waters northward from the tropics through the Gulf Stream and the North Atlantic Drift. Observations show that the AMOC has weakened from 18.8 Sv to 16.1 Sv between 2004 and 2008 (Smeed et al. 2018 [91]). Although the causes of this decline are not yet fully understood, they may involve increasing surface freshwater input from melting ice shelves or shifts in wind-driven gyre circulation patterns (see section *Gyre circulation*). The AMOC is projected to further weaken during the 21st century due to global warming (Collins 2019[71]). Such changes in the global THC are expected to alter the distribution of heat and nutrients, and to reduce CO_2 sequestration, thereby amplifying global warming (Liu et al. 2023[56]). The AABW, being the densest water mass, forms on the Antarctic continental shelves and sinks to fill the abyssal layers, contributing to the lower branch of the AMOC (Abrahamsen et al. 2019[1]). Although it is not considered as the main driver of the AMOC weakening (Smeed et al. 2018[91]), reductions in either AABW or NADW formation would inevitably lead to decreased deep-ocean ventilation and potential disruptions of global climate patterns (Zhou et al. 2023[122], Snow et al. 2015[94]). Mesoscale processes such as dense overflows play a critical role in ocean mixing and structure, and are essential for the formation and renewal of both AABW and NADW. These overflows transport cold, dense water from continental shelves into the deep ocean (Legg et al. 2009[52]). However, because dense overflows remain under-resolved in numerical ocean models, current interpretations of AABW production, and more generally of deep-ocean mixing and stratification, remain incomplete (Snow et al. 2015[94], Dufour et al. 2017[16], Heuzé 2021[37]).

Recognising their importance for the global climate, Legg et al. 2009[52] identified several major dense overflows and generalised their structure, as illustrated in fig. 1.2. Due to evaporation or ice formation, seawater density increases, particularly in shallow regions such as continental shelves or semi-enclosed seas. The resulting density contrast causes dense water to spill over ridges or sills toward the open ocean. As depicted in fig. 1.2, this hydraulically controlled overflow descends along the continental slope toward the abyssal plain, where it experiences bottom friction, shear instabilities, and entrainment with overlying layers. In other words, overflows can be viewed as downslope gravity currents. Furthermore, when these mesoscale processes occur away from the equator, the Coriolis force due to Earth's rotation significantly influences their dynamics, profoundly affecting how such flows should be represented in numerical models. This thesis aims to improve our understanding of the dynamics of rotating downslope gravity currents, which are fundamental to the complex mechanisms governing dense overflows. A better understanding of these mesoscale processes is crucial for improving their parameterisation in climate models.

As shown in fig. 1.2, a downslope gravity current is a buoyancy-driven flow in which a dense layer, i.e., denser than the ambient, develops over a sloping topography. From this definition, snow avalanches or katabatic winds can also be considered as gravity currents: in the former case, the dense fluid (a snow–air mixture) flows downslope, while in the latter, cold moist air accumulated on a plateau overflows into a warmer, drier valley. However, the overflows described by Legg evolve within a rotating environment, where the Coriolis force introduces an entirely different dynamical balance. The next chapter introduces the key theoretical concepts and assumptions that will be used throughout this manuscript.

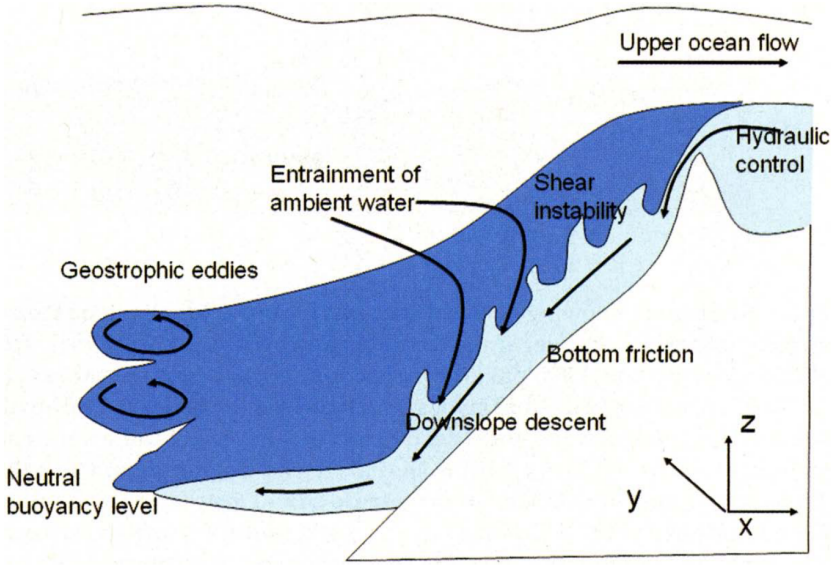

Figure 1.2: Fig. 2 from [52]: "Physical processes acting in overflows."

Chapter 2

Preliminary concepts

2.1 Introduction

This chapter introduces the key physical assumptions and theoretical tools used to study oceanic rotating gravity currents. First, the characteristic physical scales and parameters governing stratified and rotating flows are presented. Then, starting from the incompressible Navier–Stokes equations, we outline the main assumptions used to model large-scale ocean dynamics and derive the rotating shallow-water equations. By assuming an inviscid and steady-state flow, we obtain the geostrophic equilibrium. By accounting for frictional effects near boundaries, we introduce the classical Ekman theory. Finally, the principal features of large-scale ocean circulation are briefly reviewed, followed by a summary of common ocean observation techniques.

2.2 A stratified and rotating environment

2.2.1 Stratification

We describe a stratified fluid domain by introducing its characteristic physical scales and parameters. First, consider the density field ρ, which, for a fluid, may depend on pressure P, temperature T°, and chemical composition, such as the salinity S in ocean physics. In a non-uniform fluid domain, density variations can be quantified through the density gradient $\nabla\rho = (\partial_x\rho, \partial_y\rho, \partial_z\rho)$, where $\partial_x\rho$, $\partial_y\rho$, and $\partial_z\rho$ are the partial derivatives of ρ along the directions x, y, and z of a right-handed Cartesian coordinate system $(\boldsymbol{e_x}, \boldsymbol{e_y}, \boldsymbol{e_z})$.

Stratification generally refers to a non-homogeneous fluid under the influence of gravity, $g \approx 9.81\,\mathrm{m^2\,s^{-1}}$. Under this gravitational field, the non-uniform fluid tends to arrange itself into horizontal layers, such that the density gradient is primarily vertical, i.e. $\nabla\rho \approx \partial_z\rho$.

To quantify this vertical density variation, some simplifying assumptions can be made regarding the influence of P, S, and T° on ρ. First, the hydrostatic pressure increases with depth according to $\partial_z P = -\rho g$. For oceanic flows, the incompressibility assumption is usually valid, since the density of water changes very little with pressure (the compressibility is $\beta_P \approx 10^{-10}\,\mathrm{Pa^{-1}}$). Assuming $\rho = \rho(T^\circ, S)$, and considering small variations ΔT° and ΔS, the resulting $\Delta\rho$ remains small compared with the reference value $\rho_0 \approx 10^3\,\mathrm{kg\,m^{-3}}$ for freshwater, such that $\Delta\rho/\rho_0 \ll 1$. Under these conditions, a linear dependence of ρ on the tracers T° and S can be assumed:

$$\rho = \rho_0(1 - \beta_T(T^\circ - T_0^\circ) + \beta_S(S - S_0)), \tag{2.1}$$

where T_0° and S_0 are the reference temperature and salinity, respectively. eq. 2.1 shows that ρ decreases with increasing temperature and increases with salinity. This relationship, however, does not hold for freshwater below 4°C, where ρ and T° become positively correlated.

Let now consider the vertical displacement δz of a fluid parcel with density ρ_0. The parcel conserves its own density, while the surrounding density $\rho(z + \delta z)$ varies linearly over a small displacement, such that:

$$\rho(z + \delta z) - \rho_0 = \partial_z \rho \delta z. \tag{2.2}$$

We then consider the vertical motion of this displaced parcel, subject to a buoyancy force per unit volume:

$$\partial_{tt}\delta z = \frac{g}{\rho_0}\partial_z \rho \cdot \delta z \Longrightarrow \partial_{tt}\delta z + N^2 \cdot \delta z = 0, \tag{2.3}$$

which is recognised as a harmonic oscillator equation, where the frequency N is the Brunt–Väisälä (or buoyancy) frequency, defined as:

$$N = \sqrt{-\frac{g}{\rho_0}\partial_z \rho}. \tag{2.4}$$

This parameter quantifies the local stratification and is real when the environment is stably stratified, i.e. when $\partial_z \rho < 0$. In the absence of external forcing, stable stratification can only be altered by diffusive effects. Typical values are $\kappa_T \approx 10^{-7}\,\mathrm{m^2\,s^{-1}}$ for the thermal diffusion and $\kappa \approx 10^{-9}\,\mathrm{m^2\,s^{-1}}$ for the molecular diffusion.

When $\partial_z \rho > 0$, N becomes imaginary, and the hydrostatic equilibrium between horizontal layers becomes unstable: any small perturbation disrupts the balance, leading to fluid motion. In general, locally unstable stratification induces a buoyancy-driven flow.

2.2.2 Rotational Effects

Newton's Law in a rotating frame

In a rotating reference frame, inertial effects such as the centrifugal and Coriolis forces come into play. The former is intuitive and can easily be experienced as a lateral acceleration during a car turn; this apparent force acts on fixed objects in the rotating frame and depends on their distance from the rotation axis. The latter, the Coriolis force, is less intuitive: it acts only on moving objects within the rotating frame and does not depend on their position.

Because a rotating frame is non-inertial, Newton's second law cannot be directly applied. Many physical phenomena can be analysed by considering the Earth as an inertial frame, for example, the free fall of an object or the turbulent flow around an airfoil are not significantly affected by Earth's rotation. However, to study large-scale atmospheric or oceanic circulations that evolve over several days, it is essential to adopt a rotating reference frame. The following matrix equation (eq. 2.5) expresses the transformation between an inertial and a rotating coordinate system:

$$\boldsymbol{X_I} = \begin{pmatrix} x_I \\ y_I \end{pmatrix} = \begin{pmatrix} \cos(\Omega t) & -\sin(\Omega t) \\ \sin(\Omega t) & \cos(\Omega t) \end{pmatrix} \cdot \boldsymbol{X_r}, \tag{2.5}$$

where Ω is the rotation rate in $\mathrm{rad\,s^{-1}}$. Multiplying Ω by time t gives the rotation angle. Here, a constant rotation is assumed, so the Poincaré acceleration is neglected. From a position vector $\boldsymbol{X_I}$ in the inertial frame, this equation expresses the position $\boldsymbol{X_r}$ in the frame rotating at an angular displacement Ωt.

Applying this transformation to Newton's second law, without introducing any external forces,

$$\partial_t \boldsymbol{U_I} = \partial_t \boldsymbol{U_r} + 2\boldsymbol{\Omega} \times \boldsymbol{U_r} + \boldsymbol{\Omega} \times (\boldsymbol{\Omega} \times \boldsymbol{X_r}), \tag{2.6}$$

where $\boldsymbol{U_I}$ and $\boldsymbol{U_r}$ are the velocity vectors in the inertial and rotating frames, respectively. Therefore, without additional forces due to inertial acceleration, a motion in a rotating frame experiences apparent forces, written here per unit of mass: the Coriolis force, $2\boldsymbol{\Omega} \times \boldsymbol{U_r}$, and the centrifugal force, $\boldsymbol{\Omega} \times (\boldsymbol{\Omega} \times \boldsymbol{X_r})$. Thus, the dynamics in a rotating frame can be treated as inertial if these apparent forces are included.

The case of the Earth system

The Earth rotates at $\Omega = 7.3 \times 10^{-5}\,\mathrm{rad\,s^{-1}}$. However, for locally horizontal fluid flow, only the local vertical component of this rotation is dynamically relevant. This component is defined as the Coriolis parameter $f = 2\Omega \sin(\Theta)$, with Θ being the latitude, which reaches its maximum magnitude at the poles, vanishes at the equator, and changes sign between the two hemispheres.

The centrifugal force is given by $\boldsymbol{\Omega} \times (\boldsymbol{\Omega} \times \boldsymbol{X_r}) = \boldsymbol{\Omega}(\boldsymbol{\Omega} \cdot \boldsymbol{X_r}) - \Omega^2 \boldsymbol{X_r}$. Assuming purely horizontal motion, this simplifies to $-\Omega^2 \boldsymbol{X_r}$. In geophysical flows, the effect of the centrifugal force is fully balanced by the pressure gradient and is therefore neglected in the dynamical equations.

This can be understood by considering a rotating glass of water: due to the centrifugal effect, a particle within the glass experiences an apparent force $-\Omega^2 \boldsymbol{X_r}$. After sufficient time, the system reaches a steady state in which the water is at rest. This indicates that another force balances this centrifugal acceleration, specifically, a pressure gradient associated with the free-surface elevation $\eta_0(x, y)$, which rises outward from the rotation axis. At equilibrium, $g\nabla\eta_0$ exactly balances $-\Omega^2 \boldsymbol{X_r}$.

Finally, applying eq. 2.5 to the oceanic system leads to:

$$\partial_t \boldsymbol{U_I} = \partial_t \boldsymbol{U_r} + f \cdot \boldsymbol{e_z} \times \boldsymbol{U_r}, \tag{2.7}$$

2.3 Few words about ocean dynamics

2.3.1 From rotating Navier-Stokes to Shallow Water equations

For ocean dynamics, it is appropriate to start from the incompressible Navier–Stokes equations, which express conservation of mass and momentum. The mass conservation is given by the continuity equation in eq. 2.8 for incompressible fluids. For momentum conservation, we consider a rotating reference frame, which introduces the apparent forces described in eq. 2.6. In the following, we denote $\boldsymbol{U} = \boldsymbol{U_r}$. The total pressure is defined as P_T, and we absorb the centrifugal potential into the pressure term by setting $P = P_T - \frac{1}{2}|\boldsymbol{\Omega} \times \boldsymbol{X_r}|^2$. This leads to the incompressible Navier–Stokes equations in a rotating frame:

$$\nabla \cdot \boldsymbol{U} = 0, \tag{2.8}$$

$$\partial_t \boldsymbol{U} + \boldsymbol{U} \cdot \nabla \boldsymbol{U} = -\frac{1}{\rho_0}\nabla P + \nu \nabla^2 \boldsymbol{U} - g\frac{\rho}{\rho_0}\boldsymbol{e_z} + f \cdot \boldsymbol{e_z} \times \boldsymbol{U_r}, \tag{2.9}$$

where ρ_0 is the reference density. The viscous term, valid for a Newtonian incompressible fluid, involves the constant kinematic viscosity ν and the Laplacian operator ∇^2.

To simplify these equations for oceanic applications, two standard assumptions are made: 1. The ocean is very thin compared to its horizontal extent (hundreds to thousands of kilometres wide, but only a few kilometres deep). 2. Density variations are small, such that ρ can be considered homogeneous ($\nabla \rho = 0$).

Under these hypotheses, the vertical velocity and its variations with height are neglected, and the vertical momentum equation reduces to the hydrostatic balance $\partial_z P = -\rho g$. The horizontal momentum equations then become:

$$\partial_t u + u\partial_x u + v\partial_y u = -\frac{1}{\rho}\partial_x P + \nu \nabla^2 u + fv, \tag{2.10}$$

$$\partial_t v + u\partial_x v + v\partial_y v = -\frac{1}{\rho}\partial_y P + \nu \nabla^2 v - fu. \tag{2.11}$$

Since $\nabla \rho = 0$, the pressure gradients are entirely due to the free-surface elevation η, so that $\partial_x P = \rho g \partial_x \eta$ and $\partial_y P = \rho g \partial_y \eta$. At this stage, we have two equations for the three unknowns u, v, and η which are independent of the vertical direction ($\boldsymbol{e_z}$). To close the system, an additional equation describing the evolution of η is required.

The Lagrangian evolution of a fluid particle at the surface can be expressed using the material derivative as $\frac{D}{Dt}(H+\eta) = w(H+\eta)$, where H is the mean water depth. Alternatively, $w(\eta)$ can be obtained by integrating the continuity equation (eq. 2.8) between the bottom and the free surface:

$$\int_0^{H+\eta} \nabla \cdot \boldsymbol{u_h}\, dz + \int_0^{H+\eta} \partial_z w\, dz = 0, \tag{2.12}$$

where $\boldsymbol{u_h}$ denotes the horizontal velocity components, assumed vertically uniform. This gives:

$$(H+\eta)\nabla \cdot \boldsymbol{u_h} + w(H+\eta) - w(0) = 0. \tag{2.13}$$

Assuming no vertical velocity at the bottom ($w(0) = 0$), we obtain the evolution equation for the free surface:

$$\partial_t(H+\eta) + u\partial_x(H+\eta) + v\partial_y(H+\eta) + (H+\eta)\partial_x u + (H+\eta)\partial_y v = 0, \tag{2.14}$$

which simplifies to:

$$\partial_t \eta + \partial_x[(H+\eta)u] + \partial_y[(H+\eta)v] = 0. \tag{2.15}$$

eq. 2.10, eq. 2.11, and eq. 2.15 together form the shallow-water equations in a rotating frame:

$$\partial_t u + u\partial_x u + v\partial_y u - fv + g\partial_x \eta = \nu \nabla^2 u, \tag{2.16}$$

$$\partial_t v + u\partial_x v + v\partial_y v + fu + g\partial_y \eta = \nu \nabla^2 v. \tag{2.17}$$

When rotational effects dominate, nonlinear advection terms can be neglected. The resulting linearised shallow-water equations are:

$$\partial_t u - fv + g\partial_x \eta = \nu \nabla^2 u, \tag{2.18}$$

$$\partial_t v + fu + g\partial_y \eta = \nu \nabla^2 v, \tag{2.19}$$

$$\partial_t (H + \eta) + H(\partial_x u + \partial_y v) = 0. \tag{2.20}$$

Finally, for steady-state, inviscid flow conditions, appropriate far from boundaries where $\nu \approx 10^{-6}\,\mathrm{m^2\,s^{-1}}$, the balance reduces to the geostrophic relations:

$$fv = g\partial_x \eta, \tag{2.21}$$

$$fu = -g\partial_y \eta, \tag{2.22}$$

$$\partial_x u + \partial_y v = 0. \tag{2.23}$$

Combining eq2.21 and eq. 2.22 yields the geostrophic balance:

$$\boldsymbol{u_h} = \frac{g}{f} \boldsymbol{e_z} \times \nabla \eta, \tag{2.24}$$

which shows that $\boldsymbol{U} \cdot \nabla \eta = 0$, i.e. the geostrophic flow is tangent to contours of constant surface elevation η in the case of a barotropic flow. In such flows, where density depends only on pressure and is uniform on horizontal planes, which is the case for shallow water assumptions, surfaces of constant pressure (isobars) are parallel to the free surface, so the flow follows isobars everywhere. Because η is depth-independent, the vertical shear of the horizontal velocity vanishes ($\partial_z \boldsymbol{U} = 0$), a property known as the Proudman theorem. As a result, the water moves in columns, and the geostrophic flow tends to follow isobaths, linking surface elevation to bottom topography. In summary, geostrophy represents an equilibrium between the Coriolis and pressure-gradient forces in a steady, inviscid, and Boussinesq flow dominated by rotation.

2.3.2 Frictional effects and rotation: the Ekman layer

So far, friction has been ignored. It becomes significant when approaching boundaries, where the interaction between frictional forces and rotation gives rise to the *Ekman layer*, first theorised in Ekman 1905[19], who studied the effect of wind stress on the ocean surface.

Near boundaries, we consider a thin layer in a steady-state configuration, where vertical viscosity dominates, such that $\nu \nabla^2 u \approx \nu \partial_{zz} u$ and $\nu \nabla^2 v \approx \nu \partial_{zz} v$. Thus, the linearised stationary equations eq. 2.18 and eq. 2.19 reduce to the following system:

$$-fv + g\partial_x \eta = \nu \partial_{zz} u \tag{2.25}$$

$$fu + g\partial_y \eta = \nu \partial_{zz} v. \tag{2.26}$$

Outside the boundary layer, the flow is geostrophic and satisfies the same pressure gradient, giving:

$$-fv_g + g\partial_x \eta = 0 \tag{2.27}$$

$$fu_g + g\partial_y \eta = 0, \tag{2.28}$$

where u_g and v_g are the x and y components of the geostrophic velocity $\boldsymbol{V_g}$. To isolate the *ageostrophic* (shear) velocity, we subtract eq. 2.27 and eq. 2.27 from eq. 2.25 and eq. 2.26, yielding:

$$-f(v - v_g) = \nu \partial_{zz} u \tag{2.29}$$

$$f(u - u_g) = \nu \partial_{zz} v. \tag{2.30}$$

This system summarises the Ekman dynamics within a thin viscous layer, involving the *ageostrophic velocity components* $u' = u - u_g$ and $v' = v - v_g$. To derive expressions for $u'(z)$ and $v'(z)$, we introduce the complex variable $\mathcal{U}(z) = u' + iv'$, where $i^2 = -1$, so that $\partial_{zz}\mathcal{U} = \partial_{zz}u + i\partial_{zz}v$. From eq. 2.29 and eq. 2.30, we obtain:

$$\nu \partial_{zz} \mathcal{U} = -fv' + ifu' = if\mathcal{U}, \tag{2.31}$$

which gives:

$$\partial_{zz}\mathcal{U} - \frac{if}{\nu}\mathcal{U} = 0. \tag{2.32}$$

The general solution of this linear second-order ODE is an exponential, $\mathcal{U} \propto e^{kz}$. Substituting this form into eq. 2.32 gives $k^2 = \frac{if}{\nu}$. For $f > 0$ (Northern Hemisphere), this yields the complex roots:

$$k = \pm \frac{1+i}{\sqrt{2}} \sqrt{\frac{f}{\nu}} = \pm \frac{1+i}{\delta_{Ek}}, \tag{2.33}$$

where $\delta_{Ek} = \sqrt{2\nu/f}$ is the *Ekman layer thickness*. Hence, the general solution is:

$$\mathcal{U}(z) = \mathcal{A}e^{kz} + \mathcal{B}e^{-kz}. \tag{2.34}$$

The coefficients $\mathcal{A}$ and $\mathcal{B}$ are determined from the boundary conditions. Let us consider the classical case of a surface Ekman layer due to wind forcing: at depth, the velocity must approach the background flow (u_g, v_g), so that the shear vanishes as $z \to -\infty$. Thus,

$$\lim_{z \to -\infty} \mathcal{U}(z) = 0 \Rightarrow \mathcal{B} = 0. \tag{2.35}$$

At the surface, the flow is directly driven by a wind stress τ_x applied along x. For a Newtonian fluid, the shear stress is proportional to the vertical gradient of velocity:

$$\tau_x = \rho \nu \partial_z u. \tag{2.36}$$

Assuming $\partial_z v = 0$ at $z = 0$, we find:

$$\partial_z \mathcal{U}(0) = k_0 \mathcal{A} = \frac{\tau_x}{\rho\nu} \Rightarrow \mathcal{A} = \frac{\tau_x \delta_{Ek}}{\rho\nu} \frac{1}{1+i} = \frac{\tau_x \delta_{Ek}}{2\rho\nu}(1-i). \tag{2.37}$$

Since $e^{iz/\delta_{Ek}} = \cos(z/\delta_{Ek}) + i\sin(z/\delta_{Ek})$, the solution becomes:

$$\mathcal{U}(z) = \frac{\tau_x \delta_{Ek}}{2\rho\nu}(1-i)e^{z/\delta_{Ek}}(\cos z/\delta_{Ek} + i \sin z/\delta_{Ek}), \tag{2.38}$$

which gives the real velocity components:

$$u'(z) = \frac{\tau_x \delta_{Ek}}{2\rho\nu} e^{z/\delta_{Ek}} (\cos z/\delta_{Ek} + \sin z/\delta_{Ek}) \tag{2.39}$$

$$v'(z) = \frac{\tau_x \delta_{Ek}}{2\rho\nu} e^{z/\delta_{Ek}} (\sin z/\delta_{Ek} - \cos z/\delta_{Ek}). \tag{2.40}$$

At the surface ($z = 0$), $u'(0) = \frac{\tau_x \delta_{Ek}}{2\rho\nu} > 0$ and $v'(0) = -u'(0)$. Thus, for an eastward wind stress, the surface current is deflected by 45 ° to the right (northward) in the Northern Hemisphere. With increasing depth, the current speed decays exponentially while its direction rotates clockwise, forming the characteristic *Ekman spiral*, as illustrated in fig. 2.1.

The net effect of this spiral can be evaluated by integrating the velocity profiles eq. 2.39 and eq. 2.40 over depth. Letting $\mathcal{V} = \frac{\tau_x \delta_{Ek}}{2\rho\nu}$ and $\mathcal{Z} = z/\delta_{Ek}$ ($dz = \delta_{Ek} d\mathcal{Z}$), we define the zonal and meridional *Ekman transports*:

$$\mathcal{T}_x = \int_{-\infty}^{0} u'(z) dz = \int_{-\infty}^{0} \delta_{Ek} \mathcal{V} e^{\mathcal{Z}} (\cos \mathcal{Z} + \sin \mathcal{Z}) d\mathcal{Z} \tag{2.41}$$

$$\mathcal{T}_y = \int_{-\infty}^{0} v'(z) dz = \int_{-\infty}^{0} \delta_{Ek} \mathcal{V} e^{\mathcal{Z}} (\sin \mathcal{Z} - \cos \mathcal{Z}) d\mathcal{Z}. \tag{2.42}$$

Evaluating these integrals yields:

$$\mathcal{T}_x = \delta_{Ek} \mathcal{V} [e^{\mathcal{Z}} \sin \mathcal{Z}]_{-\infty}^{0} = 0 \tag{2.43}$$

$$\mathcal{T}_y = -\delta_{Ek} \mathcal{V} [e^{\mathcal{Z}} \cos \mathcal{Z}]_{-\infty}^{0} = -\delta_{Ek} \mathcal{V}, \tag{2.44}$$

so that:

$$(\mathcal{T}_x, \mathcal{T}_y) = \left(0, -\frac{\tau_x}{f\rho}\right). \tag{2.45}$$

This result shows that the net Ekman transport is directed 90 ° to the right of the wind stress in the Northern Hemisphere (northward for an easterly wind).

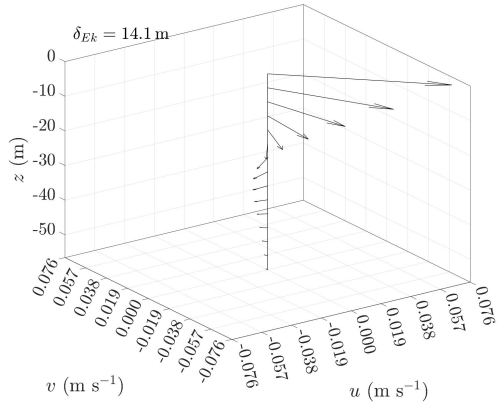

Figure 2.1: Schematic illustration of the Ekman spiral: surface flow directed 45° to the right of the wind, with speed decaying and direction rotating clockwise with depth. Case computed with the following parameters: $f = 10^{-4}\,\mathrm{s}^{-1}$, $\nu = 10^{-2}\,\mathrm{m}^2\,\mathrm{s}^{-1}$, $\tau_x = 0.1\,\mathrm{N/m}^2$.

In the next section, we examine how this surface Ekman transport drives the large-scale *wind-driven ocean circulation*, before moving to a brief description of the *Global Thermohaline Circulation*.

2.3.3 Large scale circulation systems

Gyre circulation

We have seen so far that the surface wind drives the upper-layer flow through the Ekman spiral, transporting water 90 ° to the right when $f > 0$ (Northern Hemisphere). From the linear shallow-water equations eq. 2.18, eq. 2.19, and eq. 2.20, let us now consider a steady, inviscid flow subject to wind stress forces $\frac{\tau_x}{\rho H}$ and $\frac{\tau_y}{\rho H}$ along x and y. These considerations reduce eq. 2.18 and eq. 2.19 to:

$$-fv + g\partial_x \eta = \frac{\tau_x}{\rho H}, \tag{2.46}$$

$$fu + g\partial_y \eta = \frac{\tau_y}{\rho H}. \tag{2.47}$$

Computing the curl of the velocity field, that is $\partial_x(2.47) - \partial_y(2.46)$, gives:

$$\partial_x(fu) + \partial_y(fv) = \frac{1}{\rho H}(\partial_x \tau_y - \partial_y \tau_x). \tag{2.48}$$

We now assume that f varies linearly with latitude, such that $\partial_x f = 0$ and $\partial_y f = \beta$, which defines the so-called β-plane approximation. From the steady-state configuration of eq. 2.20, we also have $\partial_x u + \partial_y v = 0$. Combining these relations yields the *Sverdrup balance*:

$$H\beta v = \frac{1}{\rho}(\partial_x \tau_y - \partial_y \tau_x), \tag{2.49}$$

where $(\partial_x \tau_y - \partial_y \tau_x) = (\nabla \times \boldsymbol{\tau})$ is the curl of the wind stress $\boldsymbol{\tau} = (\tau_x, \tau_y)$.

To better visualise how this relation drives ocean circulation, we introduce the depth-integrated transports Hu and Hv and define a streamfunction Ψ such that its 90° rotated gradient,

$$\begin{pmatrix} 0 & -1 \\ 1 & 0 \end{pmatrix} \nabla \Psi,$$

describes a velocity field satisfying the continuity equation:

$$\partial_x(Hu) + \partial_y(Hv) = 0. \tag{2.50}$$

From the Sverdrup relation eq. 2.49, it follows that:

$$Hv = \partial_x \Psi = \frac{1}{\rho\beta}(\partial_x \tau_y - \partial_y \tau_x). \tag{2.51}$$

Let us now consider an idealised model of the North Atlantic, where the wind stress is predominantly zonal ($\tau_y = 0$) and varies only with latitude. We assume that the zonal wind stress is maximal and eastward at the southern boundary $\tau_x(y_S) = \tau_0$, minimal and westward at the northern boundary $\tau_x(y_N) = -\tau_0$, and vanishes at mid-latitude $y_M = \frac{y_S + y_N}{2}$. We represent this variation by a sinusoidal profile:

$$\tau_x(y) = -\tau_0 \cos\left(\pi \frac{y - y_N}{y_S - y_N}\right), \quad \tau_y = 0. \tag{2.52}$$

Thus, integrating the Sverdrup relation eq. 2.49 yields the streamfunction Ψ:

$$\Psi = \int_{x_E}^{x} H v dx = -\frac{1}{\rho\beta} \int_{x_E}^{x} \partial_y \tau_x dx. \tag{2.53}$$

Since $\tau_x = \tau_x(y)$, we obtain:

$$\Phi = -\frac{x - x_E}{\rho\beta} \partial_y \tau_x dx = \frac{x - x_E}{\rho\beta} \tau_0 \partial_y (\cos(\pi \frac{y - y_N}{L_y})) = -\frac{x - x_E}{\rho\beta} \tau_0 \frac{\pi}{L_y} \sin(\pi \frac{y - y_N}{L_y}). \tag{2.54}$$

To visualise the flow pattern, we consider a square basin of $6000 \times 6000\,\mathrm{km}$ with a depth $H = 4000\,\mathrm{m}$, a β-plane defined by $\beta = 2.3 \times 10^{-11}\,\mathrm{m^{-1}\,s^{-1}}$, a reference wind stress amplitude $\tau_0 = 0.1\,\mathrm{N/^2m}$, and a water density $\rho = 10^3\,\mathrm{kg\,m^{-3}}$. The resulting streamfunction contours $\Psi(x, y)$, shown in fig. 2.2, illustrate the wind-driven circulation in this idealised North Atlantic configuration.

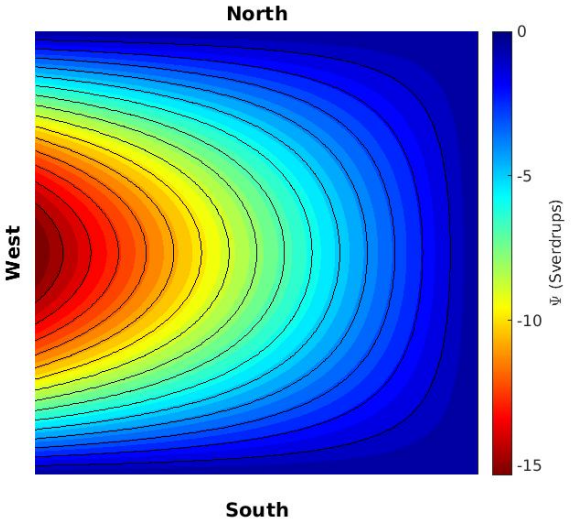

Figure 2.2: Contours of the streamfunction $\Psi(x, y)$ showing the idealised wind-driven circulation in a square North Atlantic–like basin, computed from the Sverdrup balance.

Thermohaline circulation

Before the HMS *Challenger* Expedition (1872–1876), oceanic observations were largely limited to surface currents, as measuring deeper layers from ships subjected to strong winds and surface drift remained extremely challenging. Despite these limitations, the *Challenger* expedition provided the first evidence of non-uniform horizontal distributions of temperature and salinity at depth in various ocean basins. These horizontal density gradients revealed that deep waters are not stagnant but in motion.

Modern measurements from mooring systems anchored to the sea floor have since confirmed this deep circulation, with typical velocities on the order of $10^{-2}\,\mathrm{m\,s^{-1}}$. The deep

current is composed of dense, cold water masses originating from polar regions, forming the lower branch of the Atlantic Meridional Overturning Circulation (AMOC), a key component of the global Thermohaline Circulation (THC). The typical time scale for a parcel of water to complete a full cycle within the THC and return to its initial position is about 1000 years.

At high latitudes, surface cooling and brine rejection during sea-ice formation increase water density, triggering convective instabilities that transport water downward. This process produces the North Atlantic Deep Water (NADW) in the Northern Hemisphere and the Antarctic Bottom Water (AABW) in the Southern Hemisphere. These dense water masses spread equatorward along the ocean floor. Along their path, part of the deep water slowly rises through upwelling regions, reaching warmer, lighter upper layers before being advected poleward again.

The schematic representation in fig. 2.3, adapted from the Ocean Dynamics lecture by A. Wirth [115], summarizes the main features of the global thermohaline circulation.

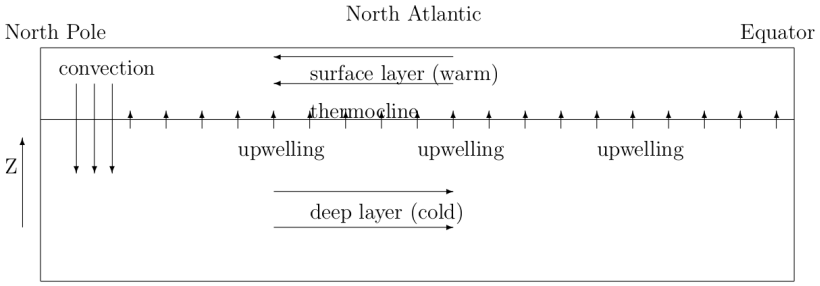

Figure 2.3: Figure 9.1 from [115]: Schematic representation of the Atlantic overturning circulation (Thermohaline Circulation).

At first glance, one might be tempted to view the THC, or at least the AMOC, as a single, large convective cell. However, this is not the case. Let us consider the North Atlantic, as illustrated in fig. 2.3. The various water transports involved can be identified as follows: the downward convective source at high latitudes (S_N), the deep southward flow of bottom water (T_b), the upward transport due to upwelling (T_{up}), and a compensating strong northward return flow along the western boundary (T_W). According to the Stommel–Arons theory (see [115]), these components satisfy the following balance:

$$S_N + T_b + T_{up} + T_W = 0. \tag{2.55}$$

While this conceptual framework captures the large-scale structure of the overturning, the fundamental mechanisms driving the THC remain an open question in oceanography.

2.3.4 Ocean observation technics

The HMS *Challenger* expedition (1872–1876) appears to be pioneer in observing in depth the ocean system, where sea water properties such as temperature, salinity or chemical composition have been measured at different depths in many places around the world. Combined with early bathymetric measurements, these observations provided an unprecedented insight into the ocean's structure and large-scale dynamics.

Since the 1980s, oceanographic satellites have revolutionised observation capabilities by providing global data of sea surface temperature (SST), salinity (SSS), and sea level. In 2022,

the Surface Water and Ocean Topography (SWOT) mission was launched to deliver high-resolution two-dimensional sea surface height (SSH) observations, with a horizontal spatial resolution of 15 –30 km and an accuracy of about 2.7 cm per 1 km^2 pixel. SWOT operates on a 21-day repeat orbit, ensuring global coverage but facing challenges in resolving fast-evolving oceanic processes with timescales shorter than 20 days.

Other missions, particularly those operated by the European Space Agency (ESA), provide complementary datasets. For example, the Sentinel-3A and 3B satellites measure SST using Thermal Infrared Radiometry with a revisit time of about two days, while the SMOS (Soil Moisture and Ocean Salinity) mission retrieves SSS from microwave radiometry.

Satellite observations, however, are limited to the ocean surface. To access subsurface and deep-ocean properties, a variety of autonomous and stationary measurement devices are employed, as illustrated in fig. 2.4. The schematic identifies the major water masses, Subtropical Water (STW), Sub-Antarctic Mode Water (SAMW), Antarctic Intermediate Water (AAIW), Circumpolar Deep Water (CDW), and Antarctic Bottom Water (AABW), together with the observational platforms used to monitor them.

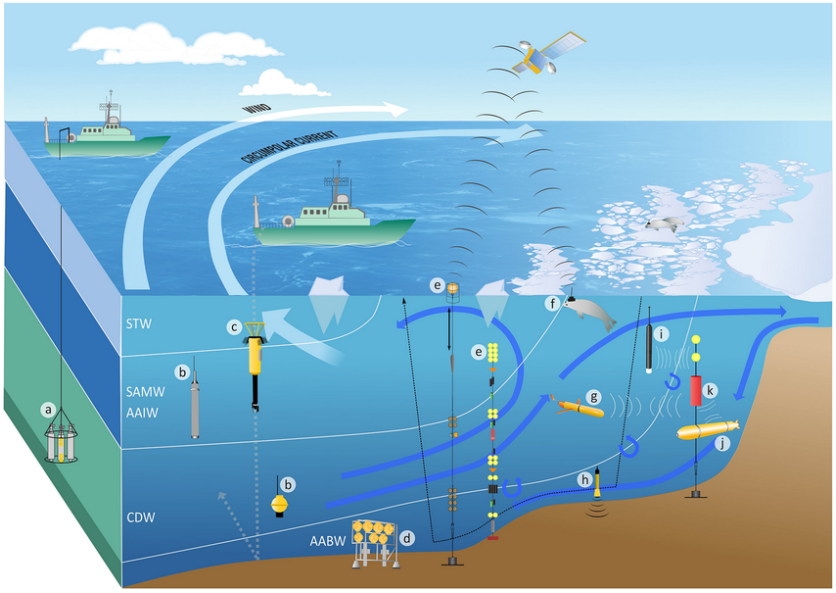

Figure 2.4: From [68]: *A schematic of the observational platforms required to observe Antarctic Bottom Water (AABW) formation. (a) Conductivity–temperature–depth profiler (CTD), often equipped with additional sensors such as dissolved oxygen, horizontal velocity (lowered ADCP – yellow cylinders), and turbulence microstructure sensors; (b) Argo profiler, including core (*$<$ 2000 m*) and deep missions; (c) microstructure profiler measuring energy and material dissipation; (d) bottom lander; (e) mooring system with physical (temperature, salinity, velocity) and biogeochemical (sediment trap, etc.) measurements, some featuring an underwater winch-driven surface buoy for ice avoidance; (f) animal-tagged profiler; (g) glider; (h) bottom drifter targeting AABW; (i) under-ice Argo profiler with acoustic locating capability; (j) autonomous underwater vehicle (AUV); (k) sound source for acoustic float locating. Modified from [62].*

Some platforms, such as Conductivity–Temperature–Depth (CTD) profilers, microstructure profilers, or under-ice Argo floats, are deployed from ships, operate by buoyancy control, or are anchored to the seafloor. These instruments perform vertical profiles of physical and biogeochemical properties, including temperature, salinity, and velocity. Because these

probes remain at fixed positions relative to the flow, their measurements are referred to as *Eulerian*. This category also includes stationary devices such as bottom landers and mooring systems.

Other platforms, such as gliders, Autonomous Underwater Vehicles (AUVs), or animal-tagged profilers, can perform preprogrammed trajectories and provide quasi-Eulerian measurements along three-dimensional paths. In contrast, when the instruments drift with the water mass, the measurements are said to be *Lagrangian*. Such measurements are obtained from drifting buoys or bottom drifters. The main observational platforms shown in fig. 2.4 are summarised in Table 2.1.

Name of Device	**Physical Scales Measured**	**Measurement Location (Path)**
a) Conductivity–Temperature–Depth (CTD) Profiler	Conductivity, Temperature, Depth, Dissolved Oxygen, Velocity	Vertical profiles
b) Argo Profiler	Temperature, Salinity	Vertical profiles (core mission $< 2000\,\mathrm{m}$, deep mission $> 2000\,\mathrm{m}$)
c) Microstructure Profiler	Energy and Material Dissipation Rate	Vertical profiles
d) Bottom Lander	Physical and Chemical Properties of Bottom Water	Stationary on seabed
e) Mooring System	Temperature, Salinity, Velocity, Biogeochemical Properties	Anchored, vertical and horizontal monitoring
f) Animal-Tagged Profiler	Temperature, Salinity, Depth	Various depths via animal movement
g) Glider	Temperature, Salinity, Biogeochemical Properties	Predefined 3D trajectory
h) Bottom Drifter	Bottom Water Properties	Drifting near seabed
i) Under-Ice Argo Profiler	Temperature, Salinity	Vertical profiles under ice
j) Autonomous Underwater Vehicle (AUV)	Physical and Chemical Properties	Predefined 3D trajectory
k) Sound Source	Acoustic Reference for Float Locating	Underwater, typically fixed

Table 2.1: Summary of observational devices represented in fig. 2.4.

Oceanic gravity currents have been observed in many regions worldwide, and their role in regulating deep-sea climate has been widely recognised. However, the small spatial and temporal scales involved in their dynamics pose challenges for global ocean models. These overflows and bottom currents involve highly localised, nonlinear, and often intermittent processes that cannot be fully resolved by current general circulation models, even with modern computational power. Therefore, realistic subgrid-scale parameterisations, grounded

in detailed observations, are essential for improving the simulation of overflow processes and for enhancing our understanding of ocean dynamics and their role in the global climate system.

Chapter 3

Gravity Currents (Literature Review)

As mentioned in the introduction, ocean gravity currents are localised processes that transport dense water from coastal or shelf regions into the ocean interior. These currents play a crucial role in shaping large-scale ocean circulation and stratification. To introduce this bibliography section, it is worth to emphasise the importance of such phenomena in oceanography and climatology, as clearly outlined in the seminal review in Legg et al. 2009[52].

According to Legg's work, ocean gravity currents exert a major influence on the large-scale dynamics and structure of the global ocean by contributing to the formation and distribution of deep and intermediate water masses. Dense overflows, such as the Nordic Seas overflows, the Mediterranean overflow, and the Antarctic overflows, affect ocean stratification through advection, vertical mixing, entrainment and other turbulent processes.

To tackle the complexity of overflow dynamics, the *Climate Process Team* (CPT), active from 2006 to 2009, encourage collaboration between observational, theoretical, and modelling communities. This initiative aimed to improve the representation of overflow processes in climate models by linking ocean observations, process studies, and parameterisation development. The study of Legg et al. 2009[52] highlights the importance of accurately parameterising overflow dynamics, as directly resolving their submesoscale structures remains computationally unfeasible.

Studying oceanic overflows is therefore of paramount importance for understanding and predicting their effects on the global ocean circulation and climate system.

The present state-of-the-art is organised as follows. Major observational studies are discussed in Section 3.1, and their geographical locations are indicated on the world map in fig. 3.1. Theoretical, numerical, and experimental investigations are presented in Section 3.2, which is divided into three parts: (i) the development of rotating gravity currents on downslope topography (Subsection 3.2.2); (ii) their intrusion into a stratified ambient (Subsection 3.2.3); and (iii) the mixing processes induced by such flows (Subsection 3.2.4).

3.1 Observations

3.1.1 Mediterranean Outflow

The Mediterranean Sea, owing to high evaporation and low precipitation, produces water with a high salinity $S_{med} = 38.4\,\text{psu}$ (Practical Salinity Units), corresponding to a density anomaly $\sigma_{med} = 28.95\,\text{kg}\,\text{m}^{-3}$, where σ is the density ρ minus $1000\,\text{kg}\,\text{m}^{-3}$. By contrast, the North Atlantic Ocean has a lower salinity and is therefore less dense, with $\sigma_{NA} =$



Figure 3.1: World map from *https://www.nationsonline.org*, modified with red circles to localise dense overflows discussed within this chapter.

$27.95\,\mathrm{kg\,m^{-3}}$. This density contrast drives the Mediterranean overflow through the Strait of Gibraltar into the Gulf of Cádiz, passing over the Camarinal Sill. This process has been widely observed and studied (Price et al. 1993[78], Pingree and Le Cann 1993[76], Swallow 1969[97], Farmer and Armi 1988[22]). The resulting outflow forms a gravity-driven current descending the continental slope. As it begins its downslope motion, the current is deflected to the right by the Coriolis force.

Price et al. 1993[78] conducted a comprehensive field survey of the Mediterranean outflow in the Gulf of Cádiz in 1988. Vertical profiles of conductivity and density were obtained at 99 locations, horizontal velocity was measured at 56 sites, and turbulence intensity profiles at 26 sites. Volume transport of salinity and density was estimated across several sections, showing that most of the mixing occurs where the current begins to descend the continental slope (section C in fig. 3.2). These observations highlight the strong link between mixing and bottom topography.

In situ data revealed that the dense overflow continues westward and descends the slope until reaching neutral buoyancy at depths of about 800 m to 1300 m. During this descent, the bottom flow entrains less saline North Atlantic water, reducing its salinity and density from $\sigma = 28.95\,\mathrm{kg\,m^{-3}}$ to $\sigma = 27.6\,\mathrm{kg\,m^{-3}}$.

Price et al. 1993 further describe the dynamics of the Mediterranean outflow as it enters the Gulf of Cádiz and interacts with bottom topography, which can be summarised as follows. Initially, the outflow is confined within a narrow channel that extends the Strait of Gibraltar (sections A and B in fig. 3.2). Here, the bottom slope is typical of a continental shelf (about 10^{-3}), and the flow is relatively steady, with a Froude number $Fr = \frac{U}{\sqrt{g'h}} \leq 1$. Note that Fr compares the flow velocity U with the shallow-water reduced-gravity wave speed $\sqrt{g'h}$, where h is the current thickness and $g' = \frac{\Delta\rho}{\rho_0}$ the reduced gravity.

Once the outflow begins its downslope descent, entrainment and bottom friction become significant, causing strong mixing within the overflow (section C in fig. 3.2). The Coriolis force, acting through Earth's rotation, also limits acceleration, forcing the current to follow

isobaths (contour line of equal water depth)poten rather than descending directly downslope (section D in fig. 3.2). In this region, mixing is particularly intense, and the outflow eventually equilibrates within the pycnocline (interface between the bottom and top layers) instead of sinking further, while the Froude number reaches a maximum value of $Fr = 1.3$.

As the outflow progresses into the final region (sections E and F in fig. 3.2), it approaches geostrophic balance. Mixing with Atlantic water is reduced, turbulence intensity decreases, and bottom stress becomes the main damping mechanism. The current then continues westward along the Portuguese continental slope as a damped geostrophic flow, eventually entering the open North Atlantic. The Mediterranean outflow generates submesoscale struc-

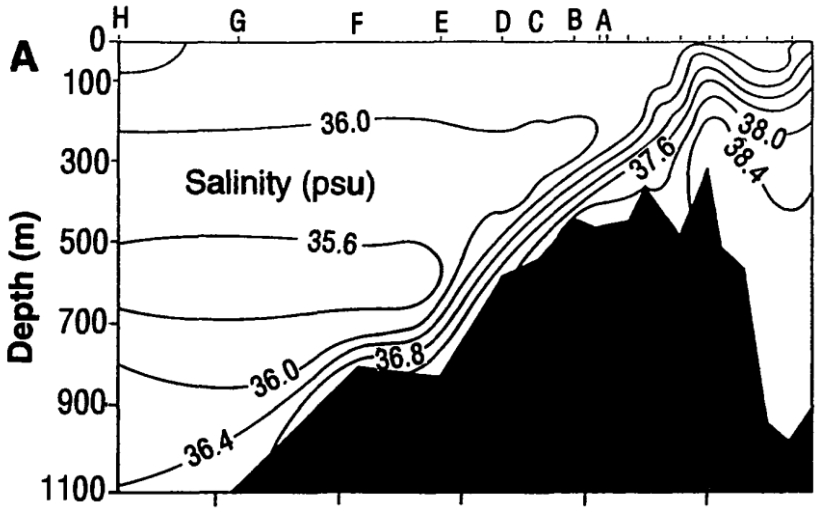

Figure 3.2: From Price et al. 1993[78]: *lateral section of the Camarinal sill showing isosalinity lines. Sections of measured region are also displayed (From upstream A to Downstream H).*

tures that are transported into the open North Atlantic. Among these, Mediterranean eddies (commonly called Meddies) have been widely observed. One such feature, the Meddy named "Bobby", was discovered in March 1992 during a survey conducted by the R.R.S. *Charles Darwin*, and its study enabled a detailed characterisation of Meddy properties, as reported in Pingree and Le Cann 1993[76].

Based on observations of Bobby, Meddies are anticyclonic oceanic eddies containing Mediterranean Water. They were first identified in Swallow 1969[97] near Cape St. Vincent. These structures transport Mediterranean water into the North Atlantic while retaining their distinctive properties over long distances, sometimes travelling more than 1500 km from their origin. Meddies are typically found at depths of 1100 m to 1500 m and possess a core diameter of around 25 km, with their influence extending radially up to 40 km.

Their vertical structure is characterised by a thickness of 775 m to 900 m, while their vertical influence can be detected over more than 3000 m. The core contains warmer, saltier water, with maximum salinity reaching 36.531 psu at a depth of 1320 m. Meddies exhibit near solid-body rotation with a rotation period of approximately 3.7 days and a relative vorticity normalised by f of about $\zeta/f = -0.5$. Their maximum velocity is measured at $30\,\mathrm{cm\,s^{-1}}$, and, as already noted, they preserve their potential vorticity owing to minimal diffusion and mixing.

3.1.2 Denmark Strait Overflow DSO

In the North Atlantic, between southern Greenland and northern Iceland, the bathymetry rises from approximately −3000 m to a sill at −600 m in the Denmark Strait, as shown in fig. 3.3. Cold, saline water originating in the Greenland Sea overflows the sill from depths of about 600 m and descends to nearly 2500 m near Cape Farewell, before intruding into the Atlantic Ocean.

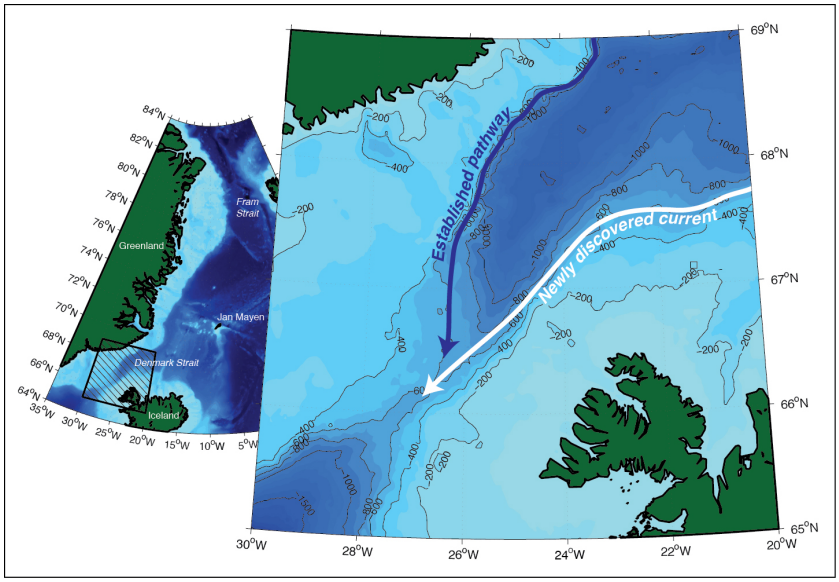

Figure 3.3: Northern Denmark Strait showing newly discovered deep current in relation to the known pathway. Credit: WHOI.

The first measurements of Denmark Strait Overflow (DSO) transport were performed by Worthington (1969) [117]. These early data revealed strong fluctuations in the overflow relative to the mean values. Worthington reported mean velocities of only a few centimetres per second, yet instantaneous fluctuations reaching up to $1\,\mathrm{m\,s^{-1}}$.

Significant progress was made during the ICES expedition *OVERFLOW'73*, which provided an extensive dataset of mooring and hydrographic measurements. Analyses in Smith 1975[92] and Ross 1984[83] revealed high variability in the DSO on short time scales (2–5 days) within a 37-day mooring record. Later, in 1997–1998, Expendable Current Profilers (XCPs) were deployed from the research vessels *Aranda* (Girton and Sanford 1999[29]) and *Poseidon* (Krauss and Käse 1998[46]), providing high-resolution velocity and structural observations of the overflow plumes.

In the context of overflows, the term *plume* refers to a narrow, dense, downwelling water mass generated at a source, such as over a sill (e.g., the Mediterranean overflow across the Camarinal Sill) or beneath an ice shelf (e.g., the Weddell Sea outflow discussed in Subsection 3.1.3).

Girton and Sanford 2003[28] compared the *OVERFLOW'73* dataset with more recent surveys, identifying universal characteristics of the DSO and the processes controlling descent and entrainment. The DSO plays a key role in the thermohaline overturning circulation, transporting about 5.2 Sv (1 Sv = $10^6\,\mathrm{m^3\,s^{-1}}$), corresponding to roughly half of the dense water formed in the Greenland, Iceland, and Norwegian Seas. Mean transport near the sill is approximately 2.9 Sv, increasing downstream to about 5.2 Sv near the Dohrn Bank (160 km away) due to entrainment of ambient water into the overflow plume. The study revealed little

change in the magnitude or variability of the transport between 1973 and 1998, suggesting robust and reproducible behaviour: the overflow pathway and plume descent are well defined over the first 250 km, strongly constrained by bottom topography and interfacial stresses. The Denmark Strait Overflow Water (DSOW) is a major source of North Atlantic Deep Water (NADW), contributing roughly two-thirds of the total NADW flux.

At submesoscales (10 km–100 km), overflow-driven structures have a marked influence on the thermohaline structure of the deep ocean. Downstream of the DSO, some of these features appear as dense lenses known as *boluses*. Morozov et al. 2020[63] described boluses about 70 km wide and 300 m thick, extending to 500 m depth and reaching velocities up to 60 $\mathrm{cm\,s^{-1}}$, compared with a background velocity of about 40 $\mathrm{cm\,s^{-1}}$. Von Appen et al. 2017[108] distinguished two recurring DSO-generated structures: (i) a bolus, interpreted as a local thickening of the overflow layer caused by a cold, cyclonic lens observed every 3–5 days, and (ii) a thinning event of the overflow layer, from 300 m to 90 m, occurring approximately every 5 days and associated with flow accelerations up to 25 $\mathrm{cm\,s^{-1}}$.

The DSO is one of two major pathways through which dense Nordic Seas water enters the Atlantic; the other is the Faroese Channels system. These shallow passages ($\leq$ 500 m) separate the Nordic Seas from the North Atlantic Ocean (fig. 3.4). The primary connection occurs via the Faroe Bank Channel, located between the Faroe Bank and the Faroe Islands. Dense, cold water from the Nordic Seas flows across the Wyville–Thomson Basin, is channelled northward to the Faroe Bank, and finally overflows a sill 850 m deep (labelled D in fig. 3.4).

Mauritzen et al. 2005[60] investigated the circulation and pathways of dense water through the Faroese Channels, identifying regions of enhanced mixing and frictional drag. Observations were collected during the RRS *Discovery* cruise in June 2000 (Price et al. 2000[79]), which covered ten cross-channel sections (A, B, D, G, H in fig. 3.4).

A total of 218 Conductivity–Temperature–Depth (CTD) stations provided vertical profiles, complemented by nutrient sampling for calibration. Velocities were recorded every 10 m using a Lowered Acoustic Doppler Current Profiler (LADCP), and 130 Expendable Current Profilers (XCPs) provided higher-resolution measurements (2 m). Historical data from campaigns such as *Overflow '60* (Harvey 1965[36]), *Overflow '73* (Dooley and Meincke 1981[15]), *NANSEN* (Borenäs and Lundberg 1998[5], Saunders 1990[85], Saunders 1992[86]), and *VEINS* (Hansen and Turrell 2001[34]) were also used for comparison.

Quantifying the total volume transport was challenging because of strong tidal variability in the Faroese Channels, where tidal currents can reach 20 $\mathrm{cm\,s^{-1}}$, a significant fraction of the mean sill velocity, about (1 $\mathrm{m\,s^{-1}}$). To reduce this, instantaneous LADCP and XCP velocities were corrected using barotropic tidal models (Egbert et al. 1995[18]). Following the dense-water pathway from section A to H (fig. 3.4), Mauritzen's analysis examined densities, temperatures, velocities, transports, and mixing. Mixing intensity was estimated using the Thorpe-scale method (Thorpe and Deacon 1977[101]), which quantifies overturns in vertical density profiles.

Upstream in the Faroe–Shetland Channel, dense water flows slowly ($\leq$ 20 $\mathrm{cm\,s^{-1}}$), comparable to tidal velocities, with average transports around 2.5 Sv. The water remains cold ($<$ 2.5 °C) but shows limited plume development or mixing. Approaching the Faroe Bank sill, the flow accelerates ($\geq$ 1 $\mathrm{m\,s^{-1}}$) as the dense layer thins to about100 m. Mean transport here is about 1.8 Sv (ranging from 1.5 to 3.5 Sv), and mixing intensifies. Downstream, mixing continues to increase as the plume descends the slope. At section G, 150 km downstream, transport reaches about 3.6 Sv and diapycnal diffusivity peaks at $5 \times 10^{-2}\,\mathrm{m^2\,s^{-1}}$. Consequently, the vertical density structure becomes more homogenised, with the densest waters

($\sigma > 28.035\,\mathrm{kg\,m^{-3}}$) progressively diluted into the surrounding ambient.

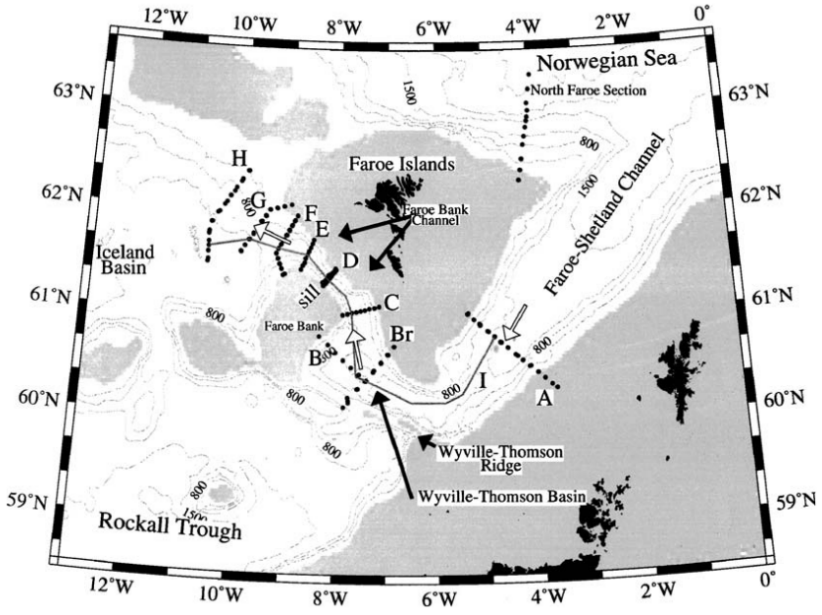

Figure 3.4: From Mauritzen et al. 2005[60]: Map of the Faroese Channels showing bathymetry and measurement sections. Water depths shallower than 500 m are shaded. Isobaths are shown every 500 m (650, 800, and deeper). Dots indicate station locations, and letters mark the cross-sections. Open arrows schematically indicate the main circulation.

3.1.3 Weddell sea

The Filchner Depression (see fig. 3.5), located in the southern Weddell Sea, is a major source of dense, cold, and saline water, and plays a crucial role in the formation of Antarctic Bottom Water (AABW) (Nicholls et al. 2004[69], Foldvik et al. 2004[24]). This process is particularly important because AABW is a key driver of the Global Thermohaline Circulation (GTHC) (Orsi et al. 1999[73]), which strongly influences the global climate.

One of the main components of the water originating from the Filchner Depression is Ice Shelf Water (ISW). ISW is formed when High Salinity Shelf Water (HSSW), generated by sea-ice formation on the continental shelf, flows beneath the Filchner Ice Shelf. There, it is further cooled by contact with the ice base, reaching potential temperatures as low as $-2.3\,^{\circ}\mathrm{C}$. Potential temperature is the temperature a water parcel would have after being brought adiabatically to the surface. This is below the surface freezing point of seawater (about $-1.9\,^{\circ}\mathrm{C}$) owing to the increased pressure at depth. For instance, at a depth of 1500 m, the typical draft of the Filchner Ice Shelf, seawater with a salinity of 34 psu, a representative value at this site, would have a freezing point near $-3\,^{\circ}\mathrm{C}$ according to the UNESCO equation of state (1983) [23].

This extremely cold ISW exits from beneath the Filchner Ice Shelf and subsequently descends the continental slope. As it flows northward, it entrains and mixes with overlying water masses, contributing to the formation of Weddell Sea Bottom Water (WSBW), which is itself a precursor of AABW.

Foldvik et al. 2004[24] quantified the ISW contribution to WSBW formation using data collected over a 30-year period (1968–1999) from current meters at various depths and

Conductivity–Temperature–Depth (CTD) measurements. Their analysis estimated that the WSBW formation rate is about 4.3 ± 1.4 Sv, with the transport of cold ISW contributing approximately 1.6 ± 0.5 Sv.

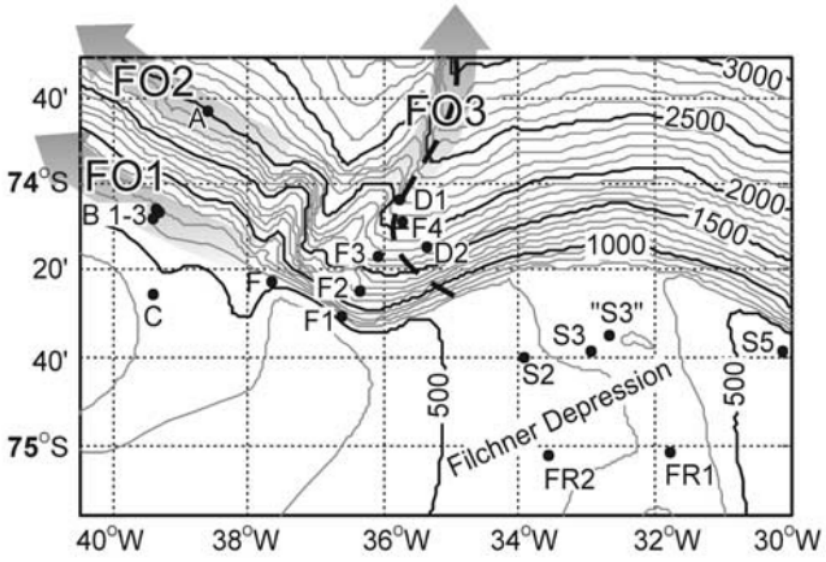

Figure 3.5: From Foldvik et al. 2004[24]: *Bathymetric map of the study area, including mooring locations. The dashed line indicates the CTD section, and shaded arrows indicate the pathways of cold shelf water.*

The study also examined frequency distributions of potential temperature as an indicator of mixing between water masses. These distributions were derived from different mooring sites in the Filchner Depression (fig. 3.5, from Foldvik et al. 2004[24]). For example, along the downslope transect from F1 to F4 in 1998, histograms showed a cut-off at $-2\,^{\circ}\mathrm{C}$, consistent with the presence of cold ISW. At F1, near the shelf break (100 m depth), the maximum potential temperature reached $0.5\,^{\circ}\mathrm{C}$, corresponding to the ambient Weddell Deep Water (WDW). At deeper sites (F2–F4), the ambient WDW temperature decreased to about $0\,^{\circ}\mathrm{C}$. At F2 and F3, a distinct peak at $-2\,^{\circ}\mathrm{C}$ was visible in the potential temperature distributions, but this peak shifted to $0\,^{\circ}\mathrm{C}$ at F4. This suggests that the ISW plume no longer descends downslope beyond F3.

However, earlier measurements from 1985 indicated that ISW occasionally penetrates to deeper layers. At site D2 (1800 m), a peak at $-2\,^{\circ}\mathrm{C}$ was observed in the distribution, consistent with the presence of an ISW plume. At greater depth, however, measurements at D1 (2100 m) revealed no such peak. This pattern was interpreted as evidence of ISW mixing with the ambient WDW.

3.1.4 Other sites around the world

The dynamics of water exchange through semi-enclosed marginal seas, such as the Persian Gulf and the Red Sea, are known to significantly influence both the structure and the principal circulation pathways of the Arabian Sea (Schott and McCreary 2001[87], Bower et al. 2000[7]). Overflow from the Strait of Hormuz primarily introduces warm, saline water from the Persian Gulf, particularly during winter, creating a distinct Persian Gulf Water (PGW) layer (Johns et al. 2003[43]). High evaporation rates over the Persian Gulf lead to the formation of dense, hypersaline water that exits through the deeper layers of the

strait. This outflow is balanced by a surface inflow of fresher Indian Ocean water, primarily along the northern part of the strait. The vertical overturning exchange is modulated by atmospheric forcing and mesoscale processes, resulting in episodic high-salinity outflows during winter. The PGW layer typically sinks below the surface and contributes to the thermohaline structure of the Arabian Sea by forming intermediate water masses.

A detailed analysis of the seasonal exchange between the Persian Gulf and the Indian Ocean through the Strait of Hormuz is presented by Johns et al. 2003[43]. Hydrographic data and moored Acoustic Doppler Current Profiler (ADCP) measurements revealed a persistent deep outflow, characterised by dense and hypersaline water with a mean speed of about $20\,\mathrm{cm\,s^{-1}}$. This outflow, occupying depths of 40 m to 200 m when entering the Gulf of Oman, has salinities between 39.3 psu and 40.8 psu, contrasting with ambient values of ≤ 37 psu. The resulting gravity current aligns along the southern wall of the channel, consistent with geostrophic adjustment.

In parallel, the Bab el-Mandeb overflow transports water from the Red Sea, characterised by higher salinity (≈ 39 psu) and temperature, which sinks to intermediate depths before entering the Arabian Sea via the Gulf of Aden (ambient salinity ≈ 36 psu). The Red Sea Outflow Experiment (REDSOX), described by Peters et al. 2005[35], showed that the Red Sea outflow splits into two distinct pathways after exiting the Strait of Bab el-Mandeb: the Northern Channel and the Southern Channel. In the Northern Channel, the current is confined within a narrow meandering channel, about 5 km wide, such that Earth's rotation does not significantly affect the flow. This current (velocity $\approx 1\,\mathrm{m\,s^{-1}}$) exhibited minimal dilution owing to weak entrainment at the bottom layer, although significant mixing occurred at the interface due to limited lateral spreading. In contrast, the Southern Channel flow was weaker ($\approx 0.5\,\mathrm{m\,s^{-1}}$) but experienced strong bottom-layer entrainment. This behaviour reflects the much wider channel geometry, which allows greater lateral spreading and enhanced rotational effects.

In this section, we have discussed several major observations of dense overflows, which are known to strongly affect the chemical composition, structure, and dynamics of the large-scale ocean system. The examples provided are indicated on the world map in fig. 3.1, although many additional cases have been studied.

One such process is cascading, described by Ivanov et al. 2004[41], whereby dense water formed on continental shelves descends under gravity into deeper ocean layers. Key parameters controlling cascading include buoyancy differences, bottom friction, ambient stratification, slope geometry, and Coriolis deflection. Ivanov et al. documented 61 cascading events worldwide, emphasising their intermittent and location-specific nature, and proposed numerical parameters to characterise their behaviour. Across this wide range of observations, the mean density contrast was found to be $0.37\,\mathrm{kg\,m^{-3}}$, but values as high as $2\,\mathrm{kg\,m^{-3}}$ have been reported in Arctic regions. The estimated downslope volumetric flux ranges from 0.05 to 0.08 Sv per 100 km of shelf edge.

To conclude, dense overflows around the world display universal features despite their diverse geographical locations. They originate from the formation of a water mass significantly denser than the surrounding ocean, which is subsequently driven across a sill where the flow typically reaches near-critical hydraulic conditions. Beyond the sill, the gravity current accelerates downslope, undergoing intense mixing and entrainment. As it descends the continental slope, the flow is deflected by the Coriolis force and by the local bathymetry. Farther from the source, entrainment weakens and the current gradually approaches geostrophic balance, spreading laterally and generating submesoscale structures that can be advected offshore. Through these interconnected processes, dense overflows provide a crucial dynamical link

between marginal-sea water-mass formation and the large-scale structure and global ocean circulation.

3.2 Physical insight of ocean Gravity Currents

3.2.1 The non-rotating lock-exchange experiment

Before introducing downslope topography and rotational effects, let us first consider two fluids of different densities separated by a vertical barrier. The resulting flow, once the barrier is removed, is known as the *lock-exchange experiment*, and has been extensively studied both experimentally (Linden and Simpson 1986[54], Shin et al. 2004[90]) and numerically (Hartel et al. 2000[40]).

The horizontal pressure difference driving the flow is $\Delta P = \Delta\rho\, gH$, where H is the total fluid depth and $\Delta\rho$ is the density difference between the two layers. When the gate is carefully lifted to minimise unwanted disturbances, the lighter fluid intrudes above the denser one, forming a turbulent gravity current. The essential dynamics can be captured through a few characteristic parameters.

Following the analysis from Linden 2012[53], the momentum balance for the denser fluid after the gate release can be expressed as:

$$\rho\, a = \frac{\Delta P}{H} \quad \text{, with} \quad a = g\frac{\Delta\rho}{\rho}, \tag{3.1}$$

where a is the acceleration, often referred to as the *reduced gravity* $g' = g\frac{\Delta\rho}{\rho}$. A characteristic velocity can be obtained by dimensional analysis. Considering a characteristic time scale $t_0 \sim H/v$, we find:

$$v \sim g' t_0 \quad \Longrightarrow \quad v \sim \sqrt{g'H}. \tag{3.2}$$

This characteristic velocity can be compared with the actual front velocity U, defining the *Froude number* $F = \frac{U}{\sqrt{g'H}}$. The Froude number is a key parameter for describing gravity current regimes, as it relates the front propagation velocity to the reduced gravity and flow depth. Several theories have been proposed to predict F in the lock-release configuration (Yih 1965[121], Von Kármán 1940[109], Benjamin 1968[3], Shin et al. 2004[90]).

Assuming total energy conservation (i.e., no dissipation), Yih 1965[121] expressed the loss of potential energy per unit width as:

$$\Delta P_E = \frac{1}{4} g\, \Delta\rho\, H^2\, U\, \Delta t, \tag{3.3}$$

where $U\Delta t$ is the distance travelled by the front during a period Δt. Under the Boussinesq approximation, the corresponding kinetic energy per unit width is:

$$K_E = \frac{1}{4}(2\rho H) U^2 U \Delta t. \tag{3.4}$$

Equating $\Delta P_E = K_E$ yields the front velocity:

$$U = \sqrt{\frac{g\, \Delta\rho\, H}{4\rho}} = \frac{\sqrt{g'H}}{2}, \tag{3.5}$$

implying $F = \frac{1}{2}$.

Linden 2012[53] also discussed the earlier approximation by Von Kármán 1940[109], who applied Bernoulli's principle to an ideal, inviscid, and irrotational flow. He considered a stagnation point at the front of the current, where the ambient fluid is at rest. Assuming pressure continuity across the interface, Von Kármán related this stagnation pressure to the hydrostatic pressure inside the current. Using Bernoulli's equation,

$$p + \frac{1}{2}\rho q^2 + g\rho z = \text{constant}, \tag{3.6}$$

and balancing pressures, he obtained $U^2 = 2g'H$, leading to $F = \sqrt{2}$.

These two classical approaches, both neglecting dissipation, highlight a significant discrepancy. Yih's theory (Yih 1965[121]) accurately predicts the front velocity for full-depth lock-release flows, whereas Von Kármán's theory performs better when the ambient is infinitely deep. An alternative formulation from Benjamin 1968[3], based on momentum conservation, gives predictions similar to Yih's, although it extends Von Kármán's framework.

A more general theory was later proposed by Shin et al. 2004[90], combining both energy and momentum conservation. This unified expression for the front velocity is:

$$U^2 = g' \frac{D(2H - D)}{4H}, \tag{3.7}$$

where D is the initial depth of the denser fluid before the barrier is removed. For $H = D$, eq. 3.7 gives $F = \frac{1}{2}$, consistent with Yih's result. Experimental data show that the thickness h of the intruding current after release is approximately $h \approx D/2$. When $D \to 0$, eq. 3.7 reduces to:

$$U^2 = g'h \quad \Longleftrightarrow \quad F = 1, \tag{3.8}$$

in excellent agreement with laboratory observations. Photographs from the experiments of Shin et al. 2004[90] are shown in fig. 3.6. Despite visible shear instabilities, the dense current occupies roughly half of the total depth, and the temporal evolution of the front position yields $F \approx 0.5$, corroborating the theoretical prediction.

Most gravity currents evolving downslope exhibit a characteristic structure, as depicted in fig. 3.7. The front head accelerates downslope, driven by momentum, and grows as it entrains ambient fluid. Behind the head, the tail region is thinner due to increased friction and elongation caused by the faster-moving head. Both the head and the tail thicken progressively due to entrainment. At low Reynolds numbers, friction dominates the flow, while at high Re, shear instabilities such as Kelvin–Helmholtz waves produce a turbulent wake behind the head. The schematic, modified from Decamp 2005[17], also indicates the typical vertical velocity profile $u(x, z)$ expected within the current.

The inclusion of rotational effects profoundly modifies the behaviour of downslope gravity currents. The study of their non-rotating analogues introduces several key physical components that remain relevant under rotation. The following subsection offers a state-of-the-art based on the evolution of our understanding of rotating downslope gravity currents.

3.2.2 A main geostrophic current

As already discussed in the introduction, a downslope gravity current is a buoyancy-driven flow in which a horizontal density gradient forces a dense fluid to descend along a sloping

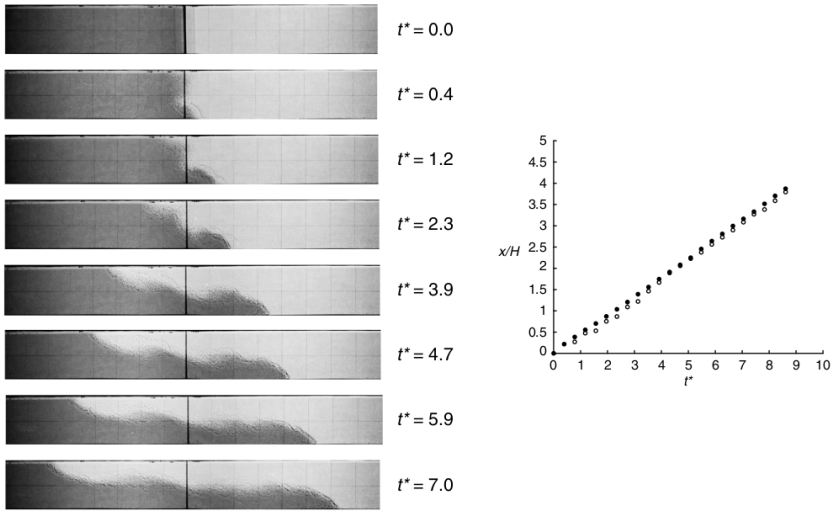

Figure 3.6: Figure 1.15 from Linden 2012[53]: *Sequences of a Boussinesq lock-release experiment. Front positions of the denser and lighter layers are plotted against time.*

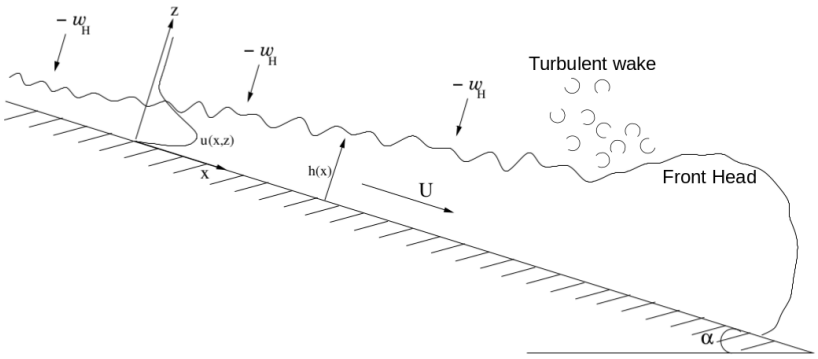

Figure 3.7: Modified schematic from Decamp 2005[17]: *Basic structure of a downslope gravity current. The front head is thicker than the tail, where shear instabilities generate a turbulent wake. The tail thins due to friction but also thickens downslope due to entrainment, characterised by the entrainment velocity* $-w_H$.

boundary. When the characteristic advection timescale of the current, L/U, becomes comparable to the Coriolis timescale f^{-1} (with f the Coriolis frequency), the Rossby number $R_o = \frac{U}{fL}$ becomes small, and the flow dynamics change fundamentally. In this rotationally dominated regime, the Coriolis force acts to deflect the current and may eventually balance the downslope buoyancy forcing. The resulting equilibrium between Coriolis and buoyancy forces is referred to as *geostrophic balance*. Once the current has adjusted geostrophically, it tends to flow along the slope rather than continuing to descend. However, bottom friction locally reduces the velocity, causing a near-slope Ekman layer to develop, which partially breaks geostrophic balance and allows a portion of the current to continue descending under gravity.

A pioneering theoretical framework for modelling downslope water flow dynamics was introduced in Bowden 1960[6]. The author examined a current flowing over a submarine

ridge and demonstrated that, under the influence of rotation, the flow tends to align parallel to the slope as it approaches geostrophic balance. Bowden derived an analytical model from the shallow-water equations, including both Coriolis and bottom friction effects. The system was represented by two layers: a thin dense lower layer, flowing over a much deeper, nearly at rest, upper layer. Within this framework, Bowden derived expressions for pressure and velocity distributions in the lower layer and showed how bottom friction modifies the flow direction, inducing a downslope deviation. Friction was represented at the seabed through a quadratic stress law, in which shear stress was related to velocity via a parameterised friction coefficient k. This parameter was constrained using oceanic observations; for example, Dietrich 1956[14] estimated $k = 3 \times 10^{-2}\,\mathrm{m^2\,s^{-1}}$ near the Iceland–Faroe Ridge. Bowden further conducted numerical simulations for various k values, demonstrating the influence of friction on flow direction. By comparing model results with observational data, he refined the parameterisation to achieve quantitative agreement.

Smith 1975[92] extended this approach by analysing deep boundary currents in a rotating and stratified ocean. Earlier works had focused primarily on water-mass budgets and transport estimates (Lee and Ellett 1965 and 1967[50, 51], Worthington 1970[118]), but Smith introduced a *streamtube model* to describe the mean dynamics of boundary currents, building on the ideas initiated by Bowden. The streamtube concept allows the representation of cross-sectionally averaged properties of the boundary current while accounting for bottom slope, frictional effects, and the Coriolis force. The concept is illustrated schematically in fig. 3.8, adapted from Girton and Sanford 2003[28]. Model parameters were calibrated using observations from the Nordic overflows through the Denmark Strait and from the Mediterranean Outflow.

The entrainment parameterisation in Smith's model was based on the laboratory experiments of Ellison and Turner 1959[20], who studied turbulent stratified flows descending inclines. The entrainment velocity was assumed proportional to the mean flow velocity, with an empirical proportionality constant E_0. Bottom friction was again represented by a quadratic drag law. Numerical integration of Smith's equations showed reasonable agreement with oceanic measurements, successfully reproducing key features of overflow structure and transport.

Killworth 1977[44] investigated the mixing mechanisms occurring along Antarctic continental slopes that lead to the formation of Antarctic Bottom Water (AABW), a key driver of the Global Thermohaline Circulation (GTHC) (Foldvik et al. 2004[24], Orsi et al. 1999[73]). The study focused on Weddell Sea Bottom Water, formed when dense shelf waters descend the continental slope and turn westward under the influence of the Coriolis force. Two and three dimensional streamtube models were developed, assuming steady-state plumes affected by bottom friction and turbulent entrainment, both essential to reproduce realistic downslope transport.

Model predictions were compared with field observations from the Weddell Sea, which had identified two major features: (i) dense water formed near the shelf break reaches the seabed at the slope base (Foster and Carmack 1976[25], Seabrooke 1971[88]), and (ii) mixing and entrainment increase the mass flux by 100–300% as the plume descends (Gill 1973[27], Foster and Carmack 1976[25]). Although these effects were included, the model could not fully reproduce the observed descent or acceleration of the plumes, suggesting the presence of an additional internal energy source. To address this, Killworth introduced a depth-dependent thermal expansion coefficient α ($^\circ\mathrm{C}^{-1}$), expressed as $\alpha_1 = \partial_z \alpha$. Accounting also for the salinity dependence via the saline contraction coefficient β (psu^{-1}), the modified linear equation of state was written as

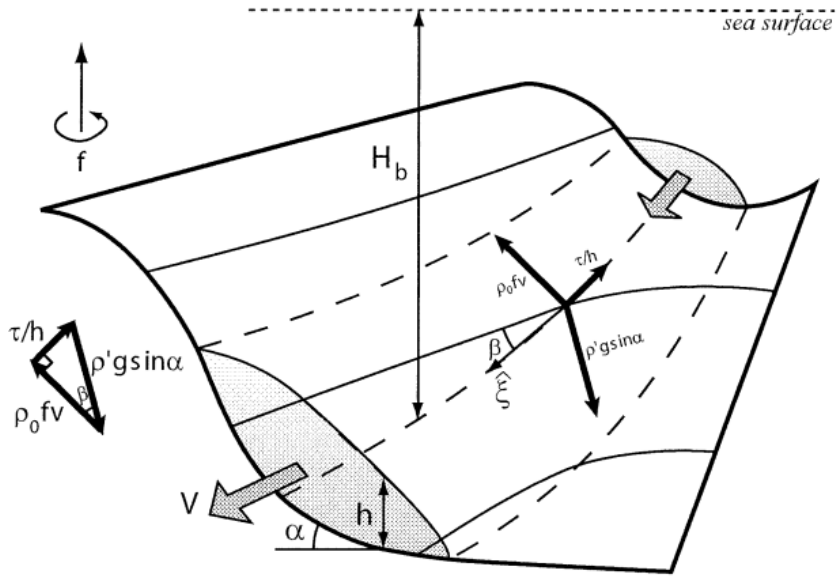

Figure 3.8: From Girton and Sanford 2003[28]: *Schematic illustration of the streamtube concept and definition of symbols. The three main forces acting on the overflow (buoyancy, drag, and Coriolis) are indicated by arrows.*

$$\frac{\rho}{\rho_0} = -\alpha(T - T_0) + \beta(S - S_0) + \alpha_1 z T, \tag{3.9}$$

where ρ_0, T_0, and S_0 are reference values of density, temperature, and salinity, respectively, and α_1 is the vertical gradient of thermal expansion with depth z. Including this nonlinearity in the equation of state allows for enhanced density increase through *cabbeling*, a process by which the mixing of two water parcels with identical densities but different temperatures and salinities produces a denser mixture. This mechanism was proposed to explain the additional densification of descending water masses observed in the Weddell Sea.

Building on these advances, Price and Baringer 1994[77] proposed a streamtube model that extended Smith's framework by introducing a Froude-number-dependent entrainment parameterisation. In their model, the entrainment coefficient E_0 varies with the Froude number, thereby linking entrainment intensity to the dynamical state of the flow and allowing it to adapt to local variations in inertial and gravitational forcing. The model also incorporated a parameterisation for lateral plume broadening based on the Ekman number, $E_k = \nu/(fh^2)$, where h is the current thickness. This broadening accounts for the lateral spreading of the plume as it flows downslope. Importantly, the numerical configuration employed realistic topographic data, significantly improving the capacity of the model to reproduce observed overflow behaviour and entrainment characteristics.

Shapiro and Hill 1997[89] presented a major study that bridged the simplicity of streamtube models, used to estimate bulk properties and trajectories of dense plumes, with the complexity of three-dimensional flow dynamics that resolve internal variations. Shapiro's model therefore not only predicts the overall plume path but also captures its interactions with both the upper layer and the seabed. For idealised cases such as uniform slopes, the model was validated against known theoretical results. For more realistic configurations, the advection–diffusion equation was solved numerically using finite differences, with applications to the Hebrides shelf edge where observational data enabled direct validation. A key finding in Shapiro and Hill 1997[89] was the identification of two downslope-driving

processes: (i) *Ekman drainage*, arising from a geostrophically adjusted along-slope current whose frictional Ekman layer leaks water downslope; and (ii) *cascading*, a gravity-driven descent of dense shelf water that is more inertial and less influenced by rotation. Cascading dominates when the dense layer is thin compared with the Ekman thickness δ_{Ek}. These two regimes, together with the theoretical structure of the gravity current, are illustrated in fig. 3.9.

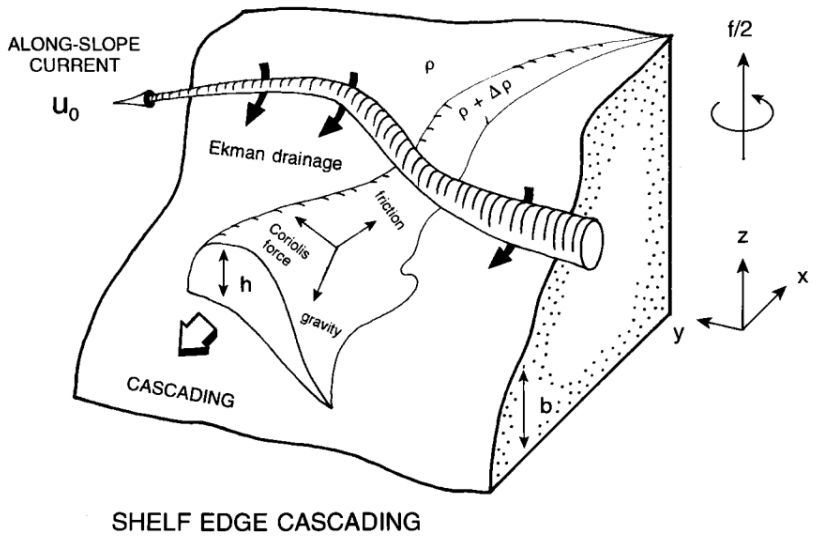

Figure 3.9: From Shapiro and Hill 1997[89]: *Schematic of cascading and current-forced Ekman drainage on a continental slope.*

Cenedese et al. 2004[12] explored density-driven downslope currents in a rotating fluid through controlled laboratory experiments. The setup consisted of a 60 cm cubic tank mounted on a 1 m diameter rotating table. The tank was filled with fresh water, while dense, dyed saline water was injected near the base of the slope. The Coriolis parameter, slope angle θ, injection rate, and reduced gravity g' were varied to investigate different regimes. Plan-view imaging captured the evolving flow, and current thickness was measured optically using a ruler normal to the slope. Over 300 experiments revealed three distinct regimes: (i) a laminar regime with nearly constant thickness; (ii) a wave regime, characterised by interfacial waves; and (iii) an eddy regime, in which cyclonic vortices periodically formed in the ambient. The transition from the wave to eddy regime is shown in fig. 3.10. A steady-state model reproduced the laminar and wave regimes, while mixing intensity increased significantly across the laminar–wave transition and with the Froude number $Fr = U_{\mathrm{exp}}/\sqrt{g' H \cos\theta}$, where U_{exp} is the measured velocity, and H a vertical length scale.

These rotationally induced waves were interpreted as analogues of oceanic mixing processes. A follow-up study by Cenedese and Adduce 2008[11] focused on mixing and entrainment, refining measurements for $0.8 < Fr < 10$ and $10 < Re < 1400$ the Reynolds number. They distinguished between non-breaking and breaking wave regimes; in the latter, direct velocity estimates from crest tracking were not feasible. The classical Ellison–Turner entrainment relation (Ellison and Turner 1959[20]) was extended to include rotational effects, leading to an empirical entrainment coefficient E that depends on the Richardson number Ri, Re, and Fr, thereby improving the description of mixing across regimes.

Lane-Serff and Baynes 1998[48] examined how downslope intrusions interact with upper layers and generate eddies. Two rotating tanks were used: a square tank (75 cm×75 cm×70 cm)

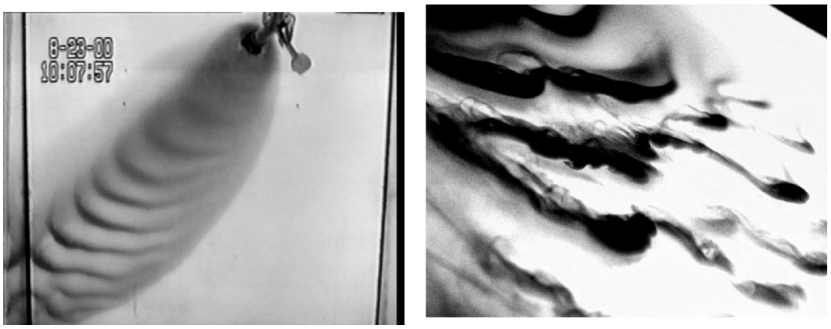

Figure 3.10: From Cenedese et al. 2004[12]: *Top view of the wave regime; right panel shows wave breaking preceding cyclonic vortex formation.*

and a circular tank (diameter 95 cm, height 50 cm) with rotation periods $3\,\mathrm{s} < T < 20\,\mathrm{s}$. The slopes tested included planes (5.7°, 15.7°) and a truncated conical topography (13.8°). Dense water entered via a near-bottom nozzle or over a weir, and dye was added to visualise the flow. Across 88 runs, the current descended before being deflected by rotation. Two components were identified: (i) an inviscid along-slope flow at the geostrophic (Nof) velocity $V_g = g's/f$, s being the topographic slope (Nof 1983[70]); and (ii) a viscous downslope transport governed by Ekman dynamics. The inviscid horizontal scale is the Rossby deformation radius $R_d = \sqrt{g'h}/f$, h being the height of the current, while the viscous drainage scale is $\mathcal{L} = Q/T_{Ek}$, with $T_{Ek} = V_g\delta_{Ek}/2$ and $\delta_{Ek} = \sqrt{2\nu/f}$ the Ekman thickness (Nagata et al. 1993[66]). Qualitatively, (i) the friction layer extends downslope; (ii) rotation suppresses vertical shear, promoting columnar flow (Taylor–Proudman effect); and (iii) slope-induced stretching of these columns amplifies vorticity, generating surface eddies. Eddy intensity increases with $\mathcal{L}/L$, i.e. with the relative dominance of viscous drainage (fig. 3.11). These surface vortices are hereafter referred to as Lane-Serff eddies.

As streamtube models have limitations in representing bottom-friction dynamics and interaction with upper layers, new approaches based on diffusion equations were developed. Wirth 2009[113] numerically modelled the dynamics of an infinitely long gravity current flowing along-slope over a constant slope s, under rotation. By considering thermal expansion, the gravity current was treated as a temperature anomaly $T°$. The three velocity components (u, v, w) were resolved, but variations in the along-slope direction were neglected, leading to a so-called 2.5-dimensional model. The initial condition was a geostrophically adjusted current with a parabolic cross-slope structure. Friction acted only near the sloping boundary. The model produced a two-part gravity current: (i) a geostrophic "vein", largely frictionless, extending cross-slope but slightly descending; and (ii) a frictional layer containing an Ekman layer, where reduced velocity weakened the Coriolis force, enabling significant downslope transport. A schematic of this structure is shown in fig3.12.

This numerical study revealed the dynamical evolution of the gravity current, including spreading and descent of the vein, and detrainment of water into the friction layer. The results demonstrated that the entire behaviour of the gravity current is strongly controlled by the thin frictional layer. This highlights a key issue for global circulation models, whose coarse vertical resolution (metres to tens of metres) cannot resolve friction-layer dynamics. Wirth 2009 further proposed a simplified analytical model for the vein thickness h, derived from numerical simulations and based on the heat equation:

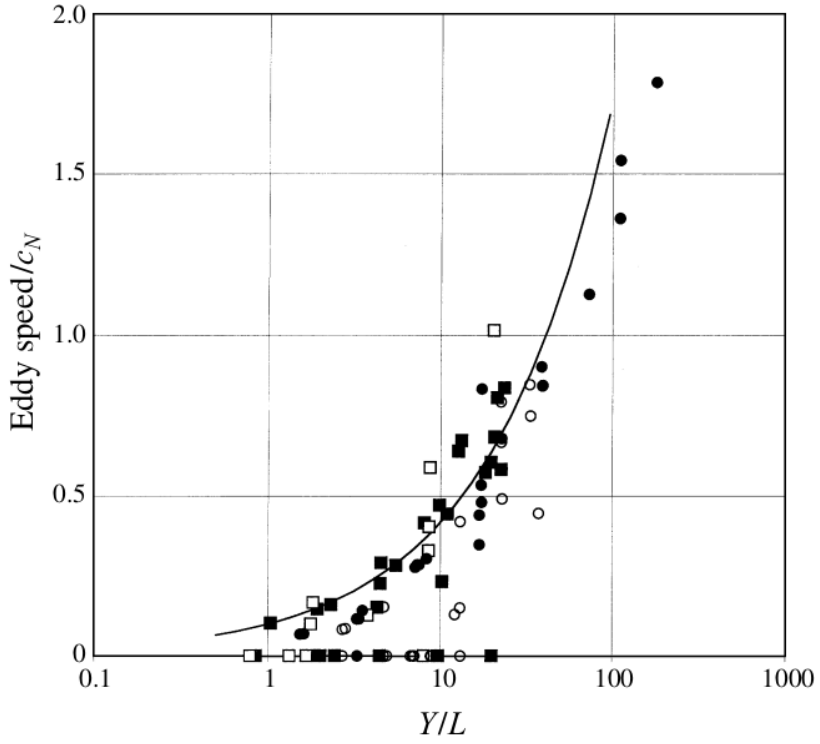

Figure 3.11: From Lane-Serff and Baynes 1998[48]: *Non-dimensional eddy speed (U/V_g) versus $\mathcal{L}/L$. Zero values indicate undetermined speeds. Stronger eddies occur when viscous drainage dominates.*

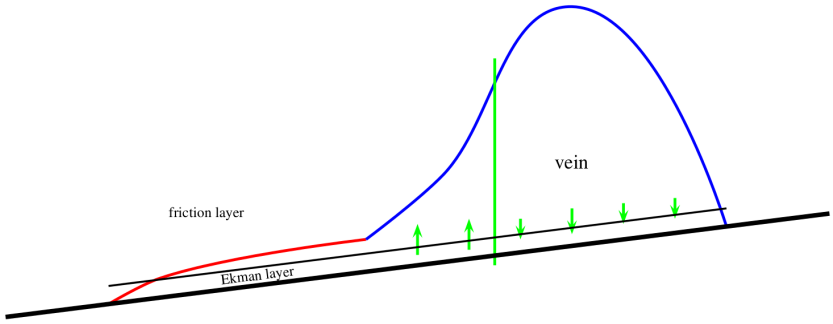

Figure 3.12: From Wirth 2009[113]: *Schematic cross-section of a gravity current on an inclined plane. The current consists of a geostrophic vein (blue), a friction layer (red), and a near-bottom Ekman layer (thin black). The green line separates concave from convex parts of the vein. Small arrows indicate vertical velocity into/out of the Ekman layer.*

$$\partial_t h = -\partial_x T_{Ek} = \frac{\delta_{Ek}}{2}\partial_x V_g = \frac{\delta_{Ek} g'}{2f}\partial_{xx} h = \partial_x (K_H \partial_x h), \tag{3.10}$$

where $T_{Ek} = V_g \frac{\delta_{Ek}}{2}$ is the Ekman transport, $V_g = g's/f$ the geostrophic velocity, δ_{Ek} the Ekman-layer thickness, and g' the reduced gravity. This model reproduced the numerical results very well, indicating that the dynamics of rotating gravity currents are primarily controlled by Ekman transport. Although large-scale instabilities were not studied due to the model geometry, eq. 3.10 provides a minimal analytical framework for stability analyses

and for parameterisation in global ocean models.

This study was preceded by Wåhlin and Walin 2001[110], who developed a similar heat-diffusion equation to describe the lateral spreading and downslope migration of dense currents driven by frictional effects, as well as the adjustment of lateral boundaries defined by the intersections between isopycnals and the bottom slope. She also compared three different approaches for bottom-friction parameterisation: one based on an Ekman boundary layer (leading to an equation similar to that of Wirth), and linear and quadratic bulk parameterisations. All three approaches produced comparable results. The model was validated by comparing its predictions with those from other analytical models (Smith 1977[93], Killworth 2001[45]) and numerical models (Baringer and Price 1997[2], Lane-Serff and Baines 1998[48]). By examining multiple parameterisations of bottom friction, Wåhlin demonstrated that her model is robust and able to represent a range of physical conditions observed in reality.

Continuing in this direction, Ungarish (2022) [106] extended Wirth's framework by including both bottom and upper-interface Ekman layers, as well as lateral momentum effects due to cross-slope velocity variations. The model considered a dense-fluid release of fixed volume over a slope, within a 2.5-dimensional lock-release scenario. The analysis began with geostrophic adjustment, producing a parabolic height profile and significant lateral velocity. The temporal evolution of the gravity current thickness $h(t)$ was solved numerically using finite differences, yielding insights into the combined effects of bottom friction, interface dynamics, and lateral momentum on gravity current evolution.

3.2.3 Intrusion

We have seen that the pathway of a rotating dense overflow on a sloping topography can be understood as the result of a balance among buoyancy, Coriolis, and frictional forces, leading to a geostrophic adjustment in the inviscid main flow and an underneath Ekman layer within the friction layer. In this subsection, we examine how dense water intrudes into a stratified ambient and the flow patterns that emerge from this intrusion.

Negretti et al. 2021[67] investigated vorticity generation during intrusion into a stratified ambient using a large rotating facility (13 m diameter, 1.2 m depth) featuring an inverted-cone topography with a central flat zone. The initial condition consisted of a two-layer stratification, while an intermediate density layer was injected at a constant rate around the rim through circumferential injectors. Particle Image Velocimetry (PIV) at multiple depths revealed submesoscale filaments and vortices originating from the slope that transported dense water toward the centre. Some injected fluid escaped the main vein through Ekman dynamics, descending the slope until reaching neutral buoyancy at the pycnocline; there, Coriolis deflection steered the flow along the topography, forming a pronounced boundary current. PIV revealed multiple mechanisms for surface vortex generation (Etling et al. 2000[21]): (i) baroclinic instability due to horizontal density gradients and rotation; (ii) geostrophic adjustment during initial descent, which thins the upper layer and enhances local vorticity via stretching; and (iii) Ekman pumping, where the coupled action of Coriolis, buoyancy, and friction induces a velocity spiral and vertical drainage, stretching vortex lines. A numerical model inspired by this work was later developed in Wirth and Negretti 2022[116].

When friction dominates within the boundary layer beneath the vein, part of the dense water continues downslope as the local buoyancy gradient no longer fully balances the Coriolis force. Boundary mixing reduces the density of the escaping water while increasing that of the ambient, progressively decreasing g' until a new equilibrium confines the flow near the slope. The resulting Deep Boundary Current (DBC) is cyclonic in the Northern Hemisphere

and anticyclonic in the Southern Hemisphere. Such intrusions generate dense eddies that detach into the interior, as shown in Spall 2010[96]. Using the MITgcm with hydrostatic primitive equations on a staggered grid (east-boundary resolution 1 km), Spall simulated uniform surface cooling and convection represented by enhanced vertical diffusion under unstable conditions, reproducing a neutrally buoyant cyclonic DBC in a stratified basin.

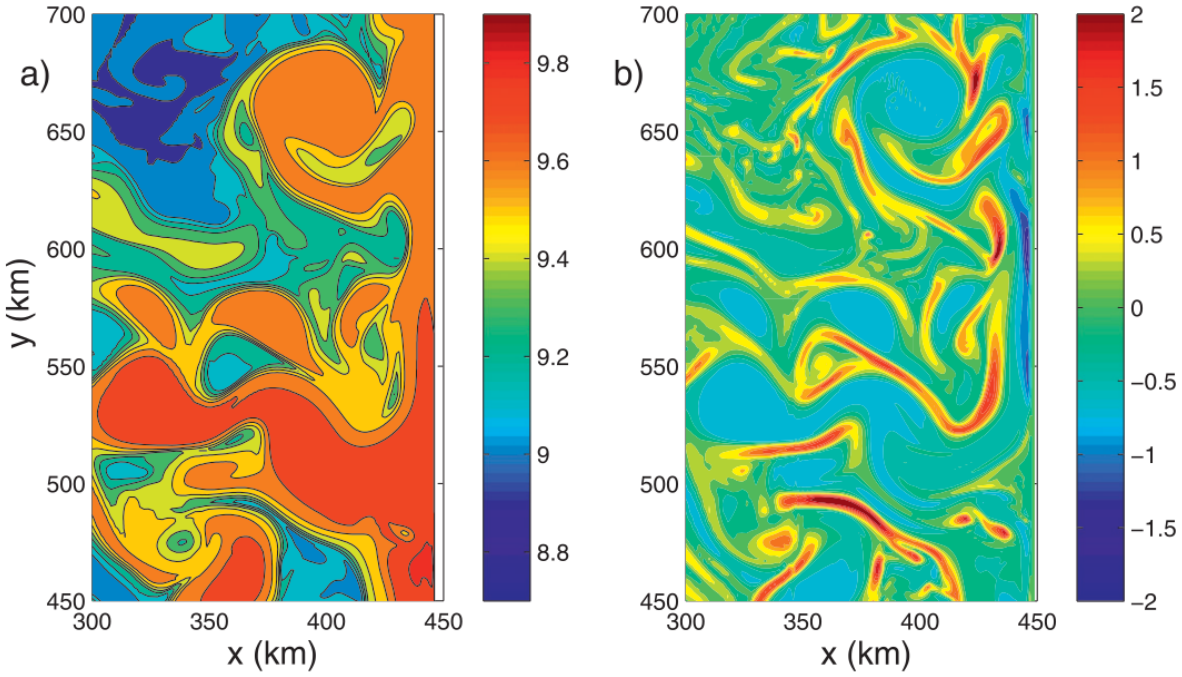

Figure 3.13: From Spall 2010[96]: *Snapshot at* 50 m *depth near the eastern boundary: (a) temperature (contours* 0.1 °C*); (b) relative vorticity normalised by f (contours 0.25). Large, warm, anticyclonic eddies are surrounded by narrow filaments of intense cyclonic vorticity.*

The contour plots presented fig. 3.13 highlights the complex dynamics near the eastern boundary resulting from the interaction between the warm, cyclonic boundary current and the ocean interior. Panel (a) shows vigorous lateral heat transfer, while panel (b) reveals alternating cyclonic and anticyclonic filaments that entrain ambient water, producing prominent submesoscale eddies.

Griffiths and Hopfinger 1983[32] conducted rotating-channel experiments in which a buoyant gravity current propagated along a lateral boundary above denser ambient water. The current formed a turbulent *nose* with strong three-dimensional mixing at the front, whereas the upstream region became quasi-two-dimensional under rotational constraint. Both velocity and layer thickness decayed exponentially with time, with a decay scale set by the Rossby deformation radius $R_d = c/f$, where $c = \sqrt{gH}$ is the non-dispersive shallow-water wave speed. Kelvin waves, resulting from the balance between Coriolis and pressure-gradient forces, transported momentum parallel to the boundary, while cross-boundary momentum exchange relied on dissipation via friction or wave breaking.

Unlike the stratified-intrusion simulations of Spall, Griffiths' experiments did not involve a stratified ambient; the current remained neutrally buoyant yet subject to both Coriolis and frictional effects. Together, these studies emphasise the fundamental role of boundary currents in transferring dense water into the ocean interior. The next subsection addresses mixing and turbulent energy generation associated with gravity-current intrusions.

3.2.4 Mixing

Mixing plays a major role in shaping the deep-ocean structure. Munk 1966[64] proposed a seminal theoretical framework for the vertical structure of the ocean. As dense, cold water sinks at high latitudes, a compensating mechanism must return deep water to the surface through upwelling. Munk argued that the energy required for abyssal upwelling is supplied by vertical mixing. While upwelling balances downwelling in mass, vertical mixing provides the energy that maintains stratification and enables the gradual rise of deep water. Munk summarised the steady-state balance between vertical mixing and upward velocity with an advection–diffusion equation,

$$\kappa\,\partial_{zz}T - w\,\partial_z T = 0, \tag{3.11}$$

where κ is the vertical diffusivity ($\mathrm{m^2\,s^{-1}}$), w the upward velocity ($\mathrm{m\,s^{-1}}$), z the vertical coordinate, and T a tracer (here, temperature). The solution of eq. 5.4 with constant coefficients yields an exponential dependence of T with depth, consistent with observed large-scale oceanic profiles.

A reassessment in Munk and Wunsch 1998[65] retained the conceptual simplicity of Munk's model, treating w and κ as vertically uniform for analytical tractability, but placed greater emphasis on the energy sources sustaining mixing, particularly winds and tides. Incorporating advances from microstructure observations, tracer-release experiments, and numerical modelling, they argued that the mixing required to maintain the global overturning circulation is far from uniform: it is intensified near boundaries, over rough topography, seamounts, and continental slopes. While Munk 1966[64] implied a canonical large-scale diffusivity of order $1 \times 10^{-4}\,\mathrm{m^2\,s^{-1}}$, tracer-release experiments in Ledwell et al. 1993[49], performed 1200 km west of the Canary Islands at 310 m depth using sulphur hexafluoride, indicated a much lower interior value $\kappa \approx 1 \times 10^{-5}\,\mathrm{m^2\,s^{-1}}$, an order of magnitude smaller than typical diapycnal values inferred near boundaries.

Kunze and Llewellyn Smith 2004[47] further challenged the notion of uniform mixing, drawing on Ledwell's tracer results. Applying Munk's balance eq. 5.4 with an upwelling speed $w \approx 1\,\mathrm{cm/day}$ and an observed stratification scale of about 1300 m gives $\kappa \sim 1 \times 10^{-4}\,\mathrm{m^2\,s^{-1}}$. However, observations from the Brazil Basin (Mauritzen et al. 2002[59]) revealed weak mixing in the interior and above smooth topography, contrasted by much larger diffusivities ($\kappa > 1 \times 10^{-4}\,\mathrm{m^2\,s^{-1}}$) over rough slopes. Together with dye experiments, microstructure profilers provide direct estimates of turbulent kinetic energy dissipation ϵ and buoyancy frequency N, related to diapycnal diffusivity via the Osborn relation (Osborn 1980[74]),

$$\kappa = \Gamma\,\frac{\epsilon}{N^2}, \tag{3.12}$$

where Γ is the mixing efficiency (typically $\Gamma \approx 0.2$) and N the Brunt–Väisälä frequency. As emphasised by Munk and Wunsch 1998[65], Kunze highlighted the significance of boundary-layer processes and tidal/internal-wave interactions, especially enhanced mixing where internal-wave beams reflect from slopes whose inclination matches the wave ray angle ($s \approx \alpha_{\mathrm{wave}}$).

Despite their simplicity, the one-dimensional models of Munk 1966[64] and Munk and Wunsch 1998[65] remain valuable descriptors of large-scale vertical structure. Their exponential profiles are widely observed and provide a first-order framework for interpreting turbulent mixing. Wunsch 2023[119] reaffirmed the utility of such reduced models for illuminating coarse-scale dynamics, even if spatial and temporal variability limits their universality. The definition of a scale height $\tilde{h} = \kappa/w$ encapsulates this structure and will be used later in this manuscript to compare vertical organisation in marge scale rotating downslope gravity-current experiments.

Localised, rotating downslope mixing was studied experimentally by Decamp during her PhD thesis in Decamp 2005[17] under the supervision of J.Sommeria. The setup consisted of a long rectangular channel mounted on the Coriolis rotating platform. A sloping bottom and initial salinity stratification established a stable background density gradient. Dense inflow at one end defined a controlled discharge Q_0 and velocity U_0, prescribing the input energy. Rotation imposed a Coriolis parameter f. Velocity and density fields were measured using conductivity probes and optical diagnostics (laser imaging and cameras). The time-dependent evolution of these fields enabled detailed estimates of energy dissipation and mixing efficiency.

Qualitatively, the experiments revealed progressive erosion of stratified layers as energy entered the system. Initially sharp interfaces degraded under turbulent mixing, while large coherent vortices, such as Lane–Serff eddies (Lane-Serff and Baines 1998[48]), redistributed energy and enhanced interfacial mixing. Rotation favoured predominantly horizontal motions, promoting anisotropic mixing. Mixing was strongest where velocity gradients were largest, progressively homogenising the density field. In a representative run lasting 1 h and 45 min, the inflow was halted and the system left to evolve under rotation alone. Vertical density profiles were recorded throughout the active and rest phases. Profiles converged after about 18 h, as depicted in fig. 3.14a, and the time-mean over the final 6 h yielded a global density probability distribution, displayed in fig. 3.14b.

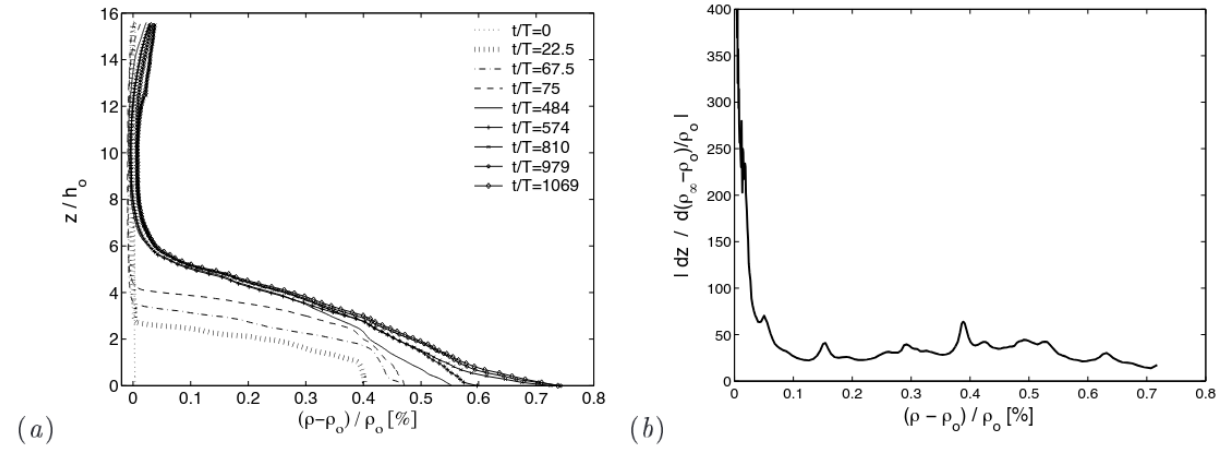

Figure 3.14: a) From Decamp 2005[17]: *Evolution of vertical density profiles from* $t/T = 0$ *to* $t/T = 78.7$ *(end of the experiment) and then until* $t/T = 1080$*. The fluid reaches a rest state for* $t/T > 810$. b) From Decampe 2005[17]: *Global density distribution from mixing of a current with initial excess* $\Delta\rho/\rho_0 = 1.5\%$.

Decamp and Sommeria concluded from fig. 3.14b that the current mixed vigorously with the ambient. From an initial density excess $\Delta\rho/\rho_0 = 1.5\%$, the post-mixing distribution is nearly homogeneous, with a dominant peak at $\Delta\rho/\rho_0 \approx 0.4\%$, representing the highest density in the current.

A contrasting oceanic analogue is provided by the Great Meteor Seamount in the Canary Basin, named after the German R/V *Meteor* expeditions (1925–1927). It offers a natural laboratory for turbulent mixing over steep slopes forced by semidiurnal tides. van Haren et al. 2012[107] deployed 101 temperature sensors at 0.5 m vertical spacing on a lander at the sloping flank, complemented by an acoustic current meter, CTD, and LADCP data. Using Thorpe-scale analysis (Thorpe and Deacon 1977[101]), they estimated mean vertical diffusivity $k_z \approx 3 \times 10^{-3}\,\mathrm{m^2\,s^{-1}}$ and energy dissipation $\epsilon \approx 1.5 \times 10^{-7}\,\mathrm{W\,kg^{-1}}$. Mixing was highly

intermittent and intensified during upslope-propagating internal bores that generated strong turbulence both near the bottom and throughout the water column, with large overturns amplifying mixing in thin stratified layers.

As discussed in Subsection 3.1.2, dense overflows in the Faroese Channels also produce intense mixing that shapes the deep North Atlantic thermohaline structure. To estimate frictional stress within the channel system, Mauritzen et al. 2005[60] applied two complementary methods: (i) a log-layer approach, assuming a near-bed logarithmic velocity profile measured by XCPs; and (ii) Thorpe-scale estimates, in which CTD-derived overturns were inverted to infer turbulent stress. Despite discrepancies (maximum stresses of order 1 Pa from the log-layer method versus 2 Pa from Thorpe scales), both approaches indicated elevated frictional stress throughout the channels, particularly at the Faroe Bank sill and downstream sections (E–G), where the plume accelerates and descends. These results confirm the major role of friction and turbulence in driving mixing within the Faroese Channels.

Chapter 4

Experimental method and data processing

4.1 The role of experimental studies

Natural processes such as gravity currents can be explored through observational surveys, laboratory experiments, or mathematical models based on first principles. The latter can sometimes be solved analytically, but in most cases numerical methods must be employed to resolve nonlinear behaviour.

Observational studies are scarce, especially for processes in the deep ocean (Wåhlin and Walin 2001[110]). Costs are high, measurements are sparse in space and/or time, parametric dependence cannot be explored systematically, and natural phenomena cannot be reproduced in controlled settings, so results are not easily generalised.

Observational surveys inspire laboratory experiments, which are less expensive, and modern methods (as in the TUBE campaign described in Negretti et al. 2021[67]) enable extended observation in space and time. Experiments are reproducible, and parametric studies can be performed in a controlled environment. Laboratory work is essential not only for validating mathematical models but also for identifying improved models that better capture observations and parameter dependences; I consider my work an example of this approach.

A mathematical model can also be used to explore phenomena that have not yet been observed. Such predictions may then motivate new observations to test the model and, in some cases, lead to the discovery of previously unobserved processes. Both laboratory experiments and mathematical models therefore guide further *in situ* observations. In this way, models, experiments, and observations influence each other synergistically. Observations, experiments, and models can thus be viewed as three communicating entities, as discussed in Greenwald 2004[31]. The diagram in fig. 4.1 summarises the interactions among them.

From observational measurements, key physical properties of the phenomenon can be identified, and an experimental setup can be designed to isolate and study the relevant processes. Using both experimental and observational results, a theoretical model, analytical or numerical, can be formulated to predict the behaviour with a given accuracy. Model validation then consists in comparing these predictions with experimental or observational data. A well-defined and extensively tested model yields physical insight that substantially improves our understanding of the phenomenon.

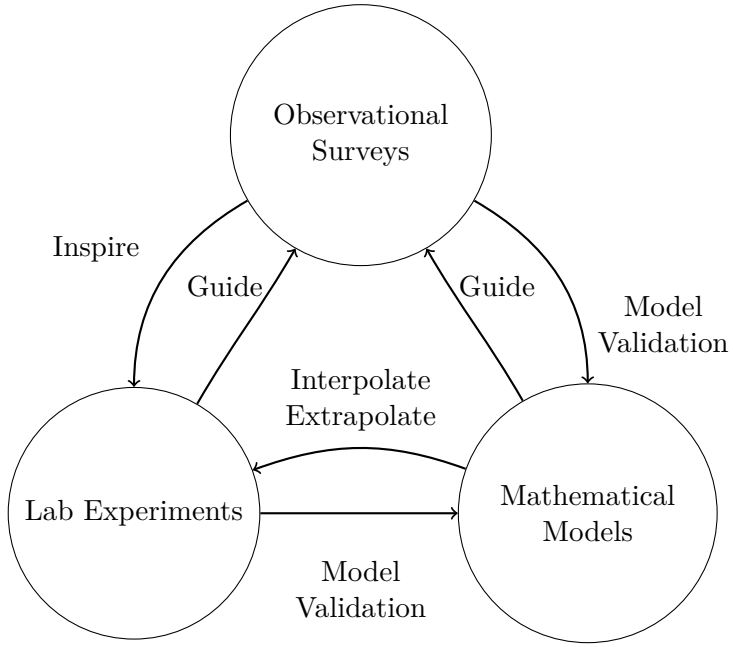

Figure 4.1: Diagram of interactions between Observational Surveys, Lab Experiments, and Mathematical Models. Observations inspire experimental design. Experimental results guide further *in situ* observations or motivate the derivation of first-principles models that provide physical insight. Models interpolate or extrapolate between measurement points and can be validated by comparison with experiments or observations.

4.2 The TUBE Experiment

4.2.1 The Coriolis Platform

Geophysical flows are characterised by the combined effects of topography, stratification, Earth's rotation, and vigorous turbulent motions that interact nonlinearly across a wide range of spatial and temporal scales. Studying such mechanisms experimentally therefore requires very large facilities, such as the 13 m-diameter rotating Coriolis Platform at the LEGI laboratory (Laboratoire des Écoulements Géophysiques et Industriels) in Grenoble.

Originally designed in the 1960s to study tidal dynamics in the English Channel, strongly influenced by the Coriolis force, the first version of the rotating tank was used by the French electrical company EDF to investigate the projected installation of a tidal power plant in the Chausey Islands. Even at that time, it was the world's largest rotating platform and established the Grenoble basin, and particularly the LEGI laboratory, as an international reference centre for experimental research on geophysical flows.

A modernised version was built in 1985, enabling more fundamental studies of rotating and stratified fluid dynamics. Major upgrades were implemented in 2002, including the integration of electronic control systems, onboard computing, and data-acquisition equipment embedded directly in the rotating frame. In parallel, significant advances were achieved in optical measurement techniques such as laser-induced velocimetry and Particle Image Velocimetry (PIV), greatly enhancing spatial and temporal resolution.

In 2011, the Coriolis platform, originally located on the Grenoble peninsula, was dismantled and reconstructed on the Saint-Martin-d'Hères campus, where it continues to operate as

one of the world's leading experimental facilities for rotating and stratified flow studies. The platform plays a key role in operational oceanography and climate modelling and has contributed to numerous major international collaborations, including the EUHIT (European High-Performance Infrastructures in Turbulence) and Hydralab projects.

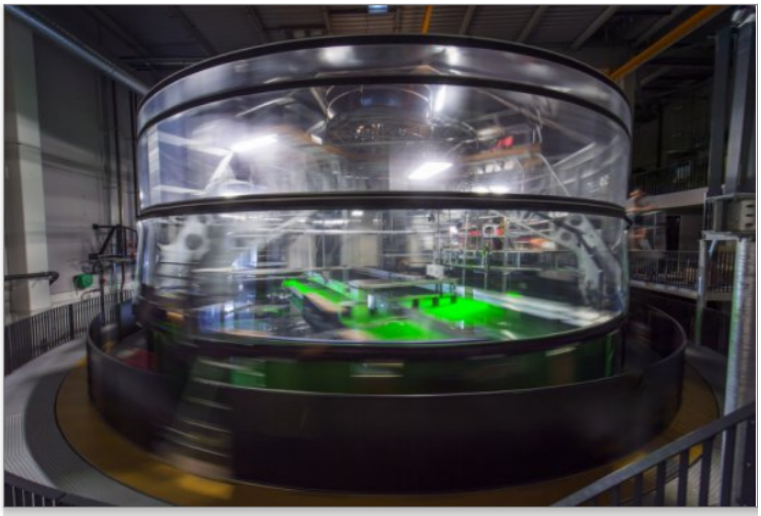

Figure 4.2: The Coriolis Platform at the LEGI lab: https://www.legi.grenoble-inp.fr/web/spip.php?article757

4.2.2 Experimental set up

The experimental campaign *Turbulent Life of Downslope Intruding Gravity Currents* (TUBE), conducted on the Coriolis Platform at LEGI (Grenoble, France), aims to elucidate the dynamics of rotating downslope dense currents and their interactions with the surrounding ambient water. These experiments provide insight into the generation of submesoscale turbulent structures formed within the boundary layers of rotating downslope gravity currents, and into the mixing induced by their intrusion from coastal environment into the deep ocean. This research is crucial for understanding the thermohaline structure and vertical water-mass exchange, as well as the transfer of energy across scales in the ocean. Such processes are fundamental for improving ocean circulation and climate models, particularly in validating non-hydrostatic numerical codes used in oceanographic simulations.

Key members involved in the TUBE project include Eletta Negretti and Achim Wirth, all affiliated with LEGI in Grenoble. The TUBE experiments reproduce rotating downslope gravity currents in an idealised, axisymmetric environment (fig. 4.3). The topography consists of a constant-slope, axisymmetric configuration forming an inverted cone that rises from a height of 40 cm at the tank edge ($R = 6.5\,\mathrm{m}$) to a central flat zone of radius $R_0 = 2.5\,\mathrm{m}$. The resulting slope is $s = 0.1$ (10% of 6°).

For most TUBE experiments, the tank is initially filled with two layers of different densities: a lower saline layer of density ρ_b and thickness $h_b \approx 15\,\mathrm{cm}$, and an upper layer of fresh water of density $\rho_t \approx 1000\,\mathrm{kg\,m^{-3}}$ and thickness $h_t \approx 35\,\mathrm{cm}$. The filling process, lasting approximately 12 hours, is performed while the tank is in rotation to ensure solid-body motion and the formation of a sharp density interface with minimal residual flow.

At the start of an experiment, saline water of density ρ_j is injected through 32 evenly spaced nozzles along the tank circumference at a radius of 6 m. Each injector is inclined at 45° in the direction of rotation to promote geostrophic adjustment of the flow. In the following sections, the density anomaly is defined as $\Delta\rho = \rho_j - \rho_t$. Two density configurations are investigated:

1. intrusive: $\rho_t < \rho_j < \rho_b$,
2. bottom: $\rho_t < \rho_j = \rho_b$.

The large scale of the Coriolis Platform provides several advantages for experimental geophysical fluid dynamics. The 13 m diameter and 1.2 m depth minimise viscous effects that would otherwise dominate in smaller tanks, enabling the study of mesoscale and submesoscale processes. The axisymmetric configuration eliminates topographic irregularities such as edges and corners, producing quasi-periodic boundary conditions. This symmetry facilitates azimuthal averaging of flow quantities to obtain the mean circulation, while deviations from this mean yield turbulent fluctuations. Such decomposition allows a clear separation between mean and fluctuating components in non-stationary flows.

The distributed injection system of 32 inlets ensures an almost perfectly circular symmetry in the generation of the gravity current. The large scale of the facility also allows long-duration experiments, up to 220 rotational periods, providing access to the full temporal evolution of the current, although the duration is ultimately limited by the absence of any sink flow.

Measurements combine several complementary techniques: Particle Image Velocimetry (PIV) for high-resolution velocity fields, an Acoustic Doppler Velocimetry Profiler (ADVP) for velocity monitoring close to the slope, and conductivity-temperature probes for detailed density measurements. The experimental setup illustrated in fig. 4.3a and described in Section 4.3 is detailed in Negretti et al. 2021[67].

4.3 Experimental measurement techniques

4.3.1 Conductivity probe for density measurements

Water density ρ increases with salinity S and decreases with temperature T. Because electrical conductivity also rises with salinity, while the influence of temperature is comparatively weak, density variations can be inferred from conductivity measurements. Although the $\rho(S,T)$ dependence is nonlinear, it can be locally approximated by a linear relation. In our experiments, temperature variations were small ($\Delta T < 1°\mathrm{C}$), so density changes were attributed solely to salinity.

The conductivity probe consists of two electrodes supplied by an AC voltage V_0 and a sensor that measures the resulting voltage V_c. As salinity increases, the measured voltage V_c varies proportionally. After calibration with a gain factor G, the output voltage fluctuates around V_0, typically between $-5\,\mathrm{V}$ and $4\,\mathrm{V}$. The MicroScale Conductivity–Temperature Instrument (MSCI) Model 125 used in these experiments measures conductivities from $0.5\,\mathrm{mS\,cm^{-1}}$ to $800\,\mathrm{mS\,cm^{-1}}$, with a frequency response of about 800 Hz.

During the TUBE experiments, the probe was positioned at a radial distance of 1.08 m from the tank centre, within the central deep area ($R < 2.5\,\mathrm{m}$; see fig. 4.3b). It moved vertically between $z_b = 1\,\mathrm{cm}$ and $z_t = 51\,\mathrm{cm}$ at a constant velocity of $1\,\mathrm{cm\,s^{-1}}$, completing

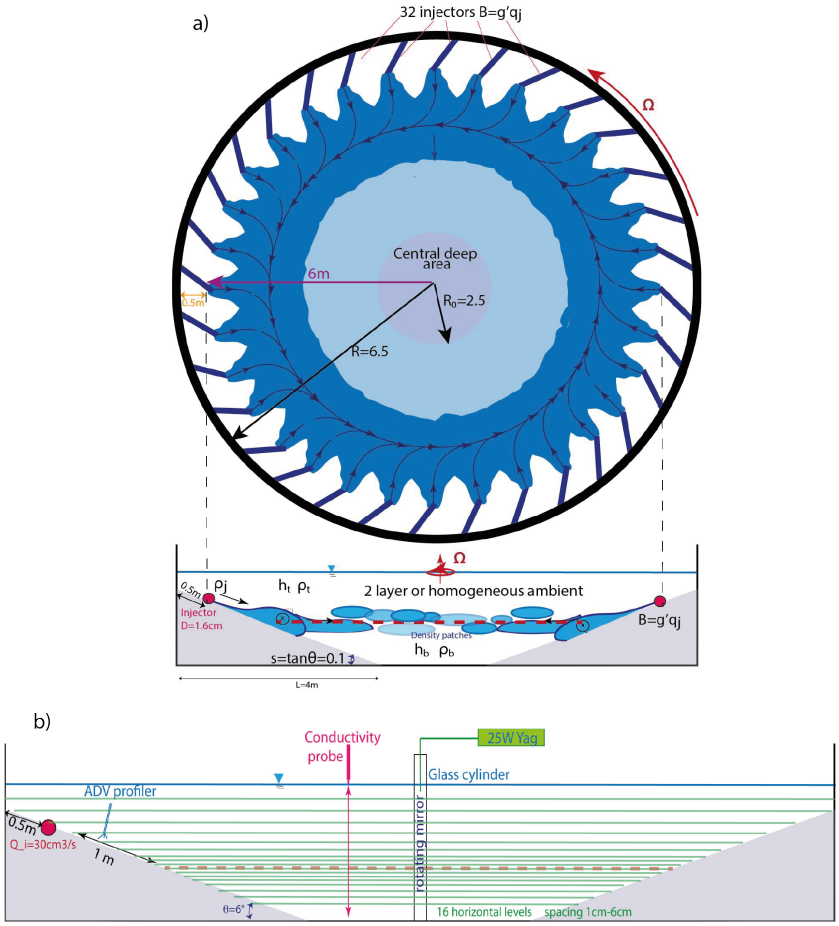

Figure 4.3: Sketch of the experimental setup from Negretti 2021[67]. (a) Schematic top and side views of the experimental configuration. Thirty-two pipes, positioned 0.5 m from the tank edge and inclined at 45°, inject saline water of density ρ_j at a constant flow rate $q_j = 32$–$43\,\mathrm{cm^3\,s^{-1}}$ into a homogeneous or stably stratified ambient. The axisymmetric conical slope has an inclination $\theta = 6°$ ($s = \tan\theta = 0.1$) and a total radial extent of 4 m. The central deep area has a diameter of 5 m. (b) Enlarged side-view sketch showing the 16 horizontal PIV measurement layers, along with the ADV position and the conductivity probe mounted on a 1 m vertical scanning axis.

each scan in about 60 s with an acquisition rate of 220 Hz. The raw data include the measured voltage V_c, the probe position, and time.

For each experiment, conductivity values were converted to density through a specific calibration procedure, as the empirical $\rho(C)$ relation varies slightly between runs. Several reference samples (typically 2–6) of known density were prepared by dissolving precise salt quantities, and their conductivities were measured with the probe. The resulting calibration points (C_i, ρ_i) were fitted with a linear regression, as shown in fig. 4.4. Although the slopes vary slightly between experiments (fig. 4.4a), calibration—performed before and after each run—ensures consistent and accurate density estimates across all datasets (fig. 4.4b). Density was then recorded continuously as the probe scanned vertically. Figure 4.5a shows the temporal evolution of probe height, while figure 4.5b presents the corresponding density measurements. Because the probe's upward motion induces small fluid disturbances, only the downward profiles (highlighted in red in fig. 4.5b) were retained for analysis. Hovmöller diagrams in fig. 4.6 confirm that upward motion perturbs the local density field, which

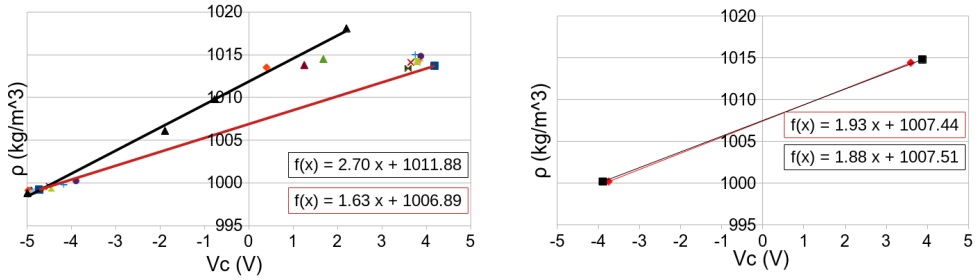

Figure 4.4: (a) Calibration points (C, ρ) obtained in 14 experiments. Red and black lines correspond to linear fits for experiments "Case 1" and "Case 9", respectively, showing that neglecting calibration would result in density-anomaly errors up to 35%. (b) Calibration before and after one experiment, showing that the linear relation remains stable over time.

rapidly relaxes to equilibrium once the probe descends.

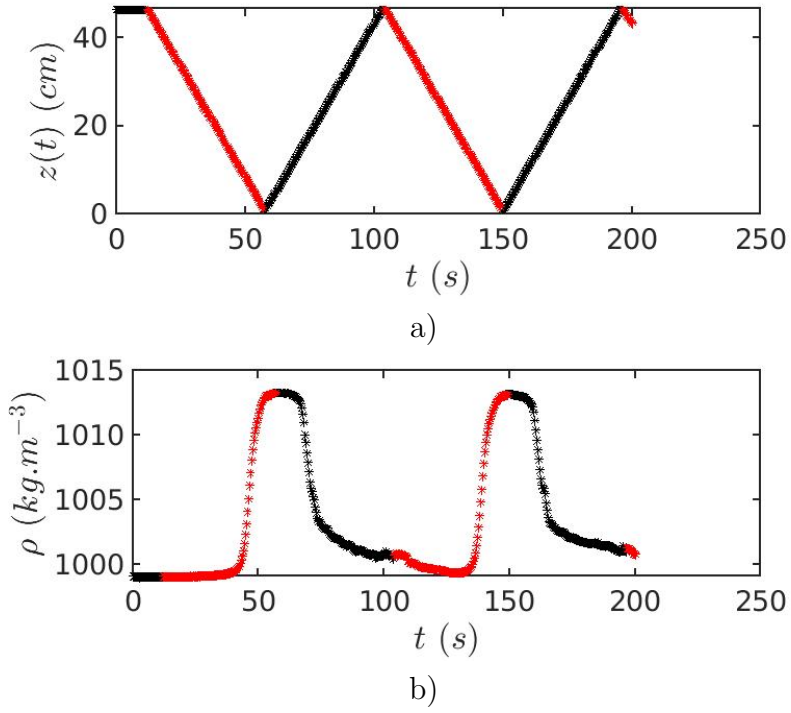

Figure 4.5: (a) Temporal evolution of the conductivity probe position z (in cm). (b) Temporal evolution of the measured density ρ (in $\mathrm{kg\,m^{-3}}$); red lines indicate downward motions used for analysis.

4.3.2 The Acoustic Doppler Velocimetry profiler (ADVP)

Velocity measurements near the topography were performed using an Acoustic Doppler Velocimetry Profiler (ADVP). The ADVP operates on the principle of the Doppler effect, whereby the frequency of a sound wave changes when the source or the observer is in motion. In this instrument, acoustic pulses are emitted into the flow, which contains particles acting as sound scatterers. As the acoustic waves encounter these particles, they are reflected

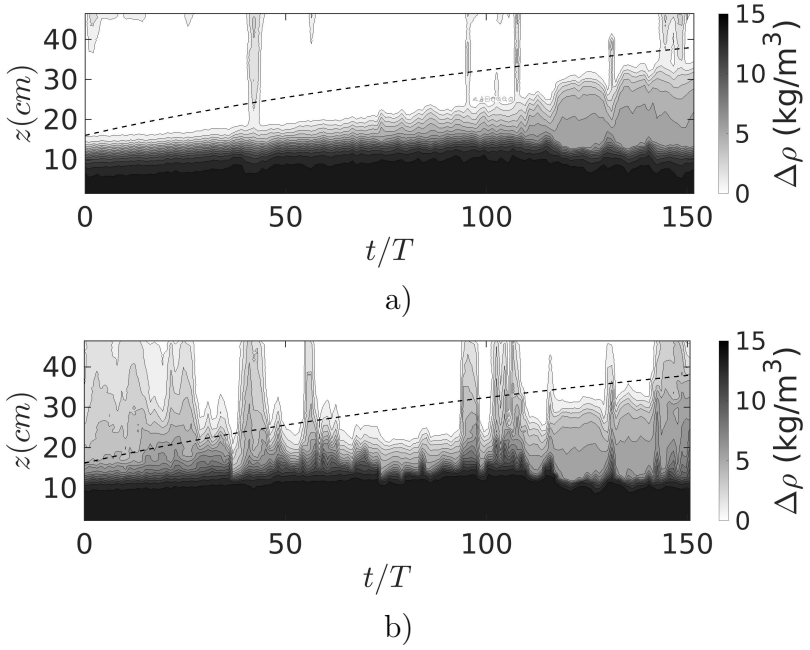

Figure 4.6: Hovmöller diagrams showing the temporal evolution of the vertical density-anomaly profile ($\Delta\rho$ in $\mathrm{kg\,m^{-3}}$). Horizontal axis: non-dimensional time t/T; vertical axis: height z (in cm). (a) Downward recordings; (b) Upward recordings, showing that the probe motion disturbs the local density structure, which rapidly returns to equilibrium.

back toward the sensor. The relative velocity between the particles and the transducers induces a frequency shift in the reflected waves, directly proportional to the particle velocity along the acoustic beam.

As depicted in fig. 4.7, the ADVP uses three acoustic transducers emitting beams in different directions that converge to a common sampling volume of vertical extent H_V. Each beam measures only the component of the particle velocity along its direction (the radial velocity). Since the distance between the particle and the transducer does not vary in any orthoradial direction, three independent beams are required to reconstruct the three velocity components. The time delay between emission and reception of the reflected signal provides the range (distance from the probe), thereby allowing a vertical profile of velocity within the sampling volume H_V to be obtained almost instantaneously.

In the TUBE experiments, the ADVP probe followed a trajectory parallel to the slope, moving from $R = 4.435\,\mathrm{m}$ to $R = 5.435\,\mathrm{m}$. The three measured velocity components (u', v', w') are defined in the local coordinate system $(\boldsymbol{x'}, \boldsymbol{y'}, \boldsymbol{z'})$, where $\boldsymbol{x'}$ and $\boldsymbol{y'}$ lie in the slope plane and $\boldsymbol{z'}$ is normal to it. The component u' is radial and directed upslope, v' is azimuthal and directed cyclonically, and z' points away from the sloping topography. The probe moves downslope along $\boldsymbol{x'}$ in discrete steps of 10 cm. At each position, the probe remains stationary for 60 s, during which continuous velocity measurements are recorded at a sampling frequency of 200 Hz. The vertical profiling range extends over $z' \in [0.2, 3.2]$ cm, resolved by 16 equally spaced points.

Because the probe continuously records data even while in motion, only the measurements acquired while it is stationary are relevant for analysis. During post-processing, the time intervals corresponding to probe motion are identified and excluded. Figure 4.8 shows the full temporal evolution of the radial velocity component u'.

The periodic sequence of local minima in $u'(t)$ corresponds to negative velocity peaks

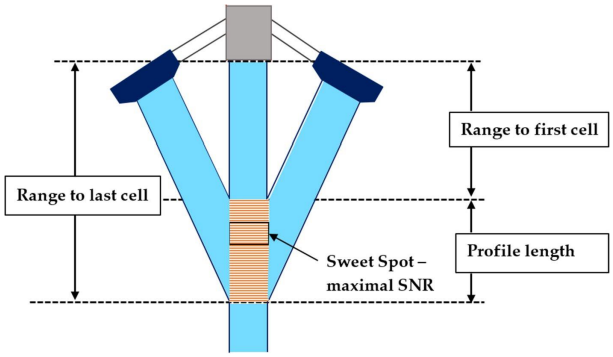

Figure 4.7: Principle of the Acoustic Doppler Velocimetry Profiler (ADVP), adapted from Liu et al. 2022[55]. Three transducers emit acoustic waves that converge to a sampling volume with a defined vertical range. The time interval between emission and reception determines the range (from the "Range to first cell" to the "Range to last cell"). The region of maximal signal-to-noise ratio ("Sweet Spot") provides the most reliable measurements.

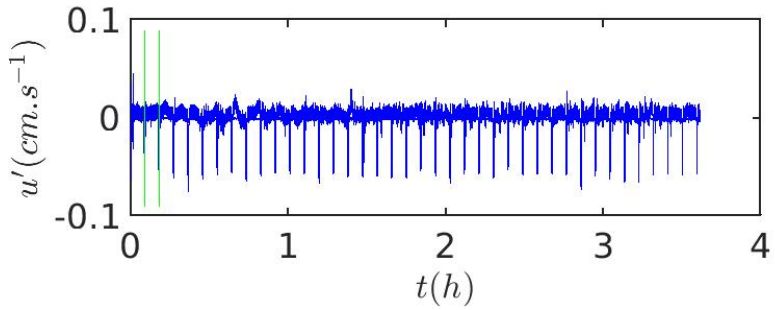

Figure 4.8: Temporal evolution (t in hours) of the downslope velocity u' (in cm s^{-1}) measured 1 cm above the slope. The blue line shows the full recording, while vertical green lines indicate the detection of scanning intervals bounded by negative velocity peaks associated with probe displacement.

generated when the probe returns to its initial position after completing each scan. These features allow segmentation of the signal into successive scanning periods. An automatic algorithm detects these peaks, enforcing a minimum time separation between consecutive detections. The vertical green lines in fig. 4.8 mark the identified scanning intervals. The velocity signal within one such interval is shown in fig. 4.9.

The acquisition window, delimited by the two vertical blue lines in fig. 4.9, contains both stationary and transition phases. The transitions between these two phases are detected as peaks in the moving standard deviation of $u'(t)$, plotted in red. This method enables automatic identification of the time periods when the ADVP is stationary, ensuring that only valid velocity data are retained for analysis.

4.3.3 Particle Image Velocimetry (PIV)

To measure the fluid velocity field across the tank domain, Particle Image Velocimetry (PIV) was employed. PIV is an optical, non-intrusive measurement technique used to capture instantaneous velocity fields in fluid flows. The fluid domain is seeded with tracer particles that are assumed to faithfully follow the fluid motion. These particles are typically small,

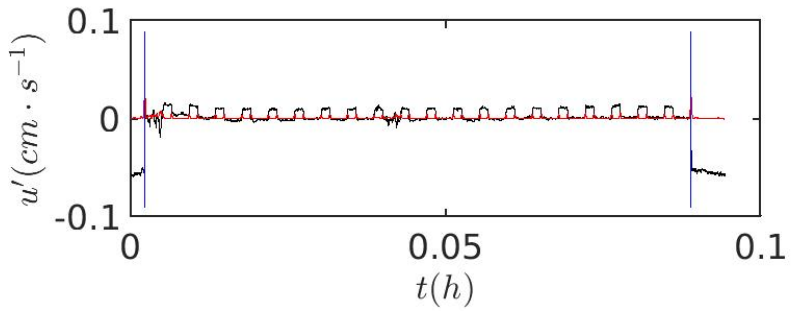

Figure 4.9: Temporal evolution (t in hours) of the downslope velocity u' (in $\mathrm{cm\,s^{-1}}$) during one scanning period. The black curve represents the recorded signal, while vertical blue lines mark the scan boundaries (corresponding to the green lines in fig. 4.8). The red curve shows the moving standard deviation (computed over 100 samples), used to detect transitions between stationary and moving phases of the probe.

neutrally buoyant, and reflective to the laser light used in illumination.

The flow field is illuminated by a thin laser sheet, created by expanding a laser beam into a plane using a fast rotating mirror that moves vertically along an axis positioned at the centre of the rotating tank. A high-resolution camera captures two successive images of the illuminated particles, separated by a short time interval Δt, typically 1 s. Each image is divided into smaller interrogation windows, and a cross-correlation analysis between corresponding windows determines the displacement of particle patterns. Dividing these displacements by Δt yields the velocity vectors in each interrogation window, resulting in a two-dimensional velocity field representing the flow dynamics within the illuminated plane.

During this campaign, both the ambient water and the injected saline solution were seeded with polyamide particles of mean diameter 60 µm and specific density $1.016\,\mathrm{kg\,m^{-3}}$. A 25 W YAG laser operating at a wavelength of 532 nm provided continuous illumination, while a high-speed rotating mirror system distributed the laser sheet over the entire tank. Images of the flow field (13 m in diameter and 9 m in height) were captured by a high-resolution Nikon D850 SLR camera (45 Mpx), mounted above the tank and synchronised with the laser system. Optical deformations and distortions were neglected. Because of the large distance between the camera and the measurement plane, just a rescaling was realised.

The laser sheet performed a vertical scan between heights of 7 cm and 51 cm above the bottom, encompassing 16 horizontal planes. A full vertical scan cycle lasted $T_V = 86.5$ s. The camera acquired one image per second, while the laser sheet shifted to the next vertical level every 5 s. The resulting dataset therefore provided quasi-simultaneous velocity measurements across multiple depths. Velocity fields were computed using cross-correlation PIV algorithms implemented in the UVMAT software. Interrogation windows were initially 35×35 pixels, reduced in subsequent passes to 20×20 pixels with a 70% overlap, optimising spatial resolution and correlation accuracy.

The picture in fig. 4.10 shows an example of a raw image captured by the Nikon camera. The illuminated laser sheet appears as a green horizontal layer at a vertical position of approximately 15 cm, close to the pycnocline. The corresponding slope intersection occurs at $R_{\mathrm{laser}} = R_0 + \frac{h_{\mathrm{laser}}}{s} \approx 4$ m. The injected saline water appears brighter due to the Rhodamine dye, and the PIV is performed by tracking the displacement of small seeding particles' as depicted in fig. 4.11.

fig. 4.12 shows an example of the velocity field computed from Correlation Image Ve-



Figure 4.10: Raw image captured by the Nikon camera showing the illuminated laser sheet (green light) at a vertical height of 15 cm, close to the pycnocline level.

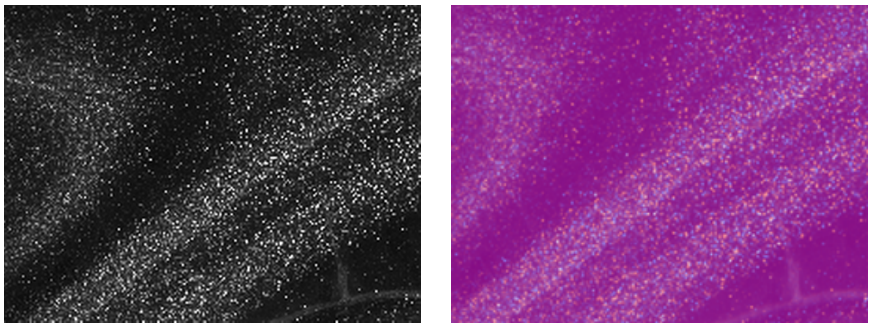

a) b)

Figure 4.11: Example of the seeded flow field. (a) Uneven distribution of tracer particles. (b) Particle displacement between two snapshots taken at a 1 s interval: red particles correspond to the first image, and blue particles to the second.

locimetry (CIV). The vectors indicate local flow direction, and their magnitude corresponds to the local velocity (in pixel $\cdot$ s^{-1}). The color of each vector represents the correlation coefficient S. The correlation may be reduced near boundaries, in regions masked by the experimental structure (white areas), or in areas with low particle density.

After rescaling, the velocity fields are converted from pixel $\cdot$ s^{-1} to cm s^{-1}. A representative result is shown in fig. 4.13, where the colour map indicates the magnitude of the velocity field computed.

4.4 Experiments and their characteristics

4.4.1 Experimental parameters

In each experiment of the TUBE campaign, a rotating gravity current is generated and evolves in an idealised environment. However, similarities can be established between ex-

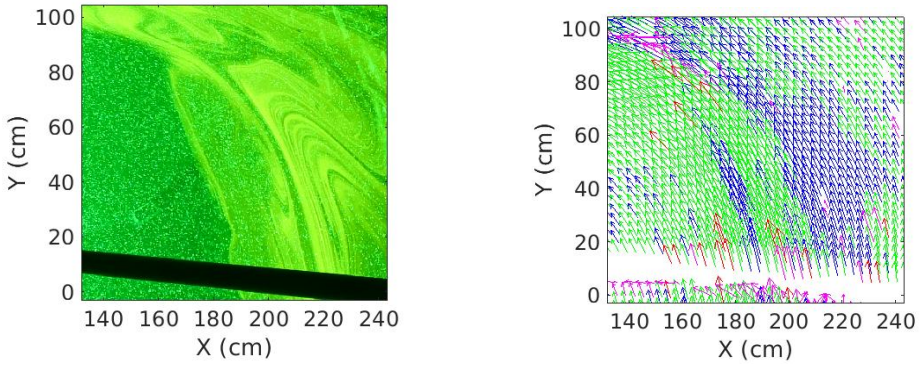

Figure 4.12: (a) Raw PIV image of the flow field. (b) Velocity field obtained from Correlation Image Velocimetry (CIV), with vectors coloured according to the correlation coefficient S. Vector length is proportional to local flow speed (in pixel $\cdot$ s^{-1}).

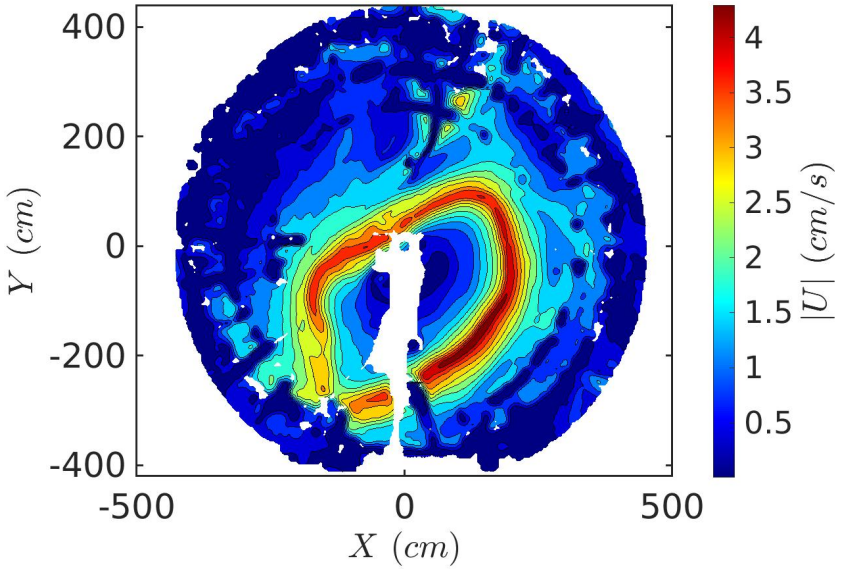

Figure 4.13: Velocity field obtained from PIV measurements. The colour map indicates flow speed.

perimental and oceanic cases, which can be summarised by the following control parameters:

- The Coriolis parameter $f = 2\Omega \sin(\Theta)$ arises from Earth's rotation Ω (rad s^{-1}) and varies with latitude Θ. In the TUBE experimental setup, f is uniform over the full domain contained within the platform, as its rotation rate cannot vary spatially. The assumption of a constant f is acceptable for the study of gravity currents, given their submesoscale extent (< 1000 km).

- When a gravity current evolves over a downslope topography, its buoyancy is strongly influenced by the density of the surrounding fluid. Therefore, a reduced gravity term $g' = g\,\frac{\rho_j - \rho_t}{\rho_t}$ is defined from the gravitational acceleration $g \approx 9.81$ m s^{-2}.

- In the ocean, dense water formed in marginal seas, basins, or continental shelves can intrude into the deep ocean by overflowing along sloping topography. Such overflowing water masses are mostly generated by surface salinity increases due to evaporation in subtropical regions, or by cooling and sea-ice formation in polar regions. The associated flow rates are typically of order 1–10 Sverdrups (1 Sv = $1 \times 10^6\,\mathrm{m^3\,s^{-1}}$). In the TUBE experiments, the rotating downslope gravity current is supplied by a constant flow rate $Q = 32\,q_j$, where q_j ($\mathrm{m^3\,s^{-1}}$) is the discharge from each of the 32 injectors.

4.4.2 Derived parameters

- When geostrophic adjustment is achieved, i.e. when the Coriolis force balances the buoyancy force ($fV_c = g's$), the current flows at the geostrophic velocity $V_g = g's/f$, also known as the Nof speed (Nof 1983[70]).

- The Ekman transport $T_{Ek} = \frac{g's}{2f}\delta_{Ek}$ represents the mass transport within the bottom boundary layer resulting from the balance between buoyancy (g'), Coriolis effects (f), and friction, characterised by the kinematic viscosity ν. The Ekman layer thickness from laminar theory is $\delta_{Ek} = \sqrt{2\nu/f}$. This transport is crucial for understanding how dense water masses formed in marginal seas or continental shelves intrude into the deep ocean.

- A characteristic horizontal length scale $\mathcal{L} = \frac{Q}{T_{Ek}}$, already defined in [48], represents the horizontal distance required for the Ekman transport to convey the total injected flux Q downslope.

- The vertical scale H denotes a theoretical overall intrusion thickness, determined from hydrostatic balance. Considering a water volume intruding into a two-layer stratified environment at the pycnocline (interface between the bottom and top layers), the thickness of injected water that penetrates into the bottom layer is derived from the following balance between the weight of the injected volume and the buoyancy forces acting upward on the portions submerged in each layer:

$$gH\rho_j = gh\rho_b + g(H-h)\rho_t. \tag{4.1}$$

From eq. 4.1, the coefficient $\gamma = \frac{\rho_j - \rho_t}{\rho_b - \rho_t}$ is obtained, and the corresponding intrusion thickness is $H = \gamma\, h_b$, which quantifies the fraction of injected water penetrating the bottom layer.

4.4.3 Dimensionless parameters

Non dimensionalisation

The momentum equation for an incompressible fluid in a rotating reference frame is given by:

$$\partial_t \boldsymbol{u} + (\boldsymbol{u}\cdot\nabla)\boldsymbol{u} = -\frac{1}{\rho}\nabla p + \nu\nabla^2\boldsymbol{u} - f\boldsymbol{e_z}\times\boldsymbol{u} + g', \tag{4.2}$$

where $\boldsymbol{e_z}$ is the vertical unit vector. Equation eq. 4.2 can be non-dimensionalised using the characteristic scales $\boldsymbol{u^*} = \boldsymbol{u}/V_g$, $\boldsymbol{x^*} = \boldsymbol{x}/\mathcal{L}$, $t^* = V_g t/\mathcal{L}$, and $p^* = -p/(\rho g' H)$, corresponding to the dimensionless velocity, length, time, and pressure fields. Substituting these dimensionless variables into eq. 4.2 yields

$$\frac{V_g^2}{\mathcal{L}}\frac{D\boldsymbol{u^*}}{Dt} = \frac{g'H}{\mathcal{L}}\nabla^* p^* + \nu\frac{V_g}{\mathcal{L}^2}\nabla^{*2}\boldsymbol{u^*} - V_g f\boldsymbol{e_z}\times\boldsymbol{u^*} + g', \tag{4.3}$$

where the dimensionless Lagrangian derivative $\frac{D\boldsymbol{u}^*}{Dt^*} = \partial_t^* \boldsymbol{u}^* + (\boldsymbol{u}^* \cdot \nabla^*)\boldsymbol{u}^*$ has been introduced for convenience. Dividing eq. 4.3 by $\frac{V_g^2}{\mathcal{L}}$ gives the final dimensionless form:

$$\frac{D\boldsymbol{u}^*}{Dt^*} = \frac{1}{F_v^2}\nabla^* p^* + \frac{1}{Re}\nabla^{*2}\boldsymbol{u}^* - \frac{1}{Ro}\boldsymbol{e_z} \times \boldsymbol{u}^* + \frac{1}{F_h^2}, \tag{4.4}$$

from which several dimensionless numbers are identified: the Reynolds number $Re = \frac{V_g \mathcal{L}}{\nu}$ from the viscous term, the Rossby number $Ro = \frac{V_g}{f\mathcal{L}}$ from the Coriolis term, the horizontal Froude number $F_h = \frac{V_g}{\sqrt{g'\mathcal{L}}}$ from the buoyancy term, and the vertical Froude number $F_v = \frac{V_g}{\sqrt{g'H}}$ from the pressure term.

Relevant numbers

The Reynolds number Re characterises the relative importance of inertial to viscous forces within a flow of characteristic length $\mathcal{L}$. For sufficiently high Re, turbulence develops, while viscosity tends to stabilise laminar motion. In the TUBE experiments, the order of magnitude $Re = V_g\mathcal{L}/\nu = \mathcal{O}(10^5)$ ensures a globally turbulent flow. The Rossby number $Ro = V_g/(f\mathcal{L})$ measures the influence of rotation on the flow dynamics. For $Ro \gg 1$, Coriolis effects become negligible and the flow is weakly affected by rotation. The vertical Froude number $F_v = V_g/\sqrt{g'H}$ compares the flow velocity to the propagation speed $\sqrt{g'H}$ of non-dispersive internal waves, analogous to the Mach number for compressible flows. When $F_v > 1$, inertial forces dominate buoyancy forces in the vertical direction, enhancing instability and mixing. The horizontal Froude number $F_h = V_g/\sqrt{g'\mathcal{L}}$ provides similar insight into horizontal flow instabilities.

Parameters discussed here are summarised in table 4.1.

Parameter/Number	**Symbol**	**Definition**
Coriolis Parameter	f	$4\pi/T$
Buoyant Acceleration	g'	$g\,(\rho_j - \rho_t)/\rho_t$
Injection Rate	Q	$32\,q_j$
Ekman Transport	T_{Ek}	$(g's/f)\,\delta_{Ek}/2$
Reference Length Scale	$\mathcal{L}$	Q/T_{Ek}
Reference Intrusion Thickness	H	γh_b, with $\gamma = (\rho_j - \rho_t)/(\rho_b - \rho_t)$
Rossby Number	Ro	$V_g/(f\mathcal{L})$
Richardson Number	Ri	$-g/\rho_t\,(\partial_z\rho)/(\partial_z U_h)^2$
Vertical Froude Number	F_v	$V_g/\sqrt{g'H}$
Horizontal Froude Number	F_h	$V_g/\sqrt{g'\mathcal{L}}$
Reynolds Number	Re	$V_g\mathcal{L}/\nu$
Buoyancy Reynolds Number	Re_b	$Re\,F_h^2$

Table 4.1: Summary of experimental parameters and relevant non-dimensional numbers.

The following table 4.2 presents the values corresponding to 15 intrusive TUBE experiments (Cases 1–15), together with representative oceanic conditions for comparison.

Experiment	g' ($\mathrm{cm\,s^{-2}}$)	f ($\mathrm{s^{-1}}$)	Q ($\mathrm{L\,s^{-1}}$)	T_{Ek} ($\mathrm{m^2\,s^{-1}}$)	H (cm)	Ro –	F_v –	F_h –
Case 1	5.79	0.21	0.69	4.29×10^{-5}	0.063	8.2×10^{-3}	0.46	0.028
Case 2	6.09	0.21	1.19	4.51×10^{-5}	0.042	5.2×10^{-3}	0.57	0.023
Case 3	5.5	0.21	1.15	4.07×10^{-5}	0.063	4.4×10^{-3}	0.45	0.021
Case 4	5.1	0.10	1.35	1.07×10^{-4}	0.056	3.7×10^{-2}	0.92	0.061
Case 5	5.1	0.14	1.39	6.95×10^{-5}	0.058	1.3×10^{-2}	0.67	0.036
Case 6	4.81	0.14	1.37	6.54×10^{-5}	0.073	1.2×10^{-2}	0.58	0.034
Case 7	12.75	0.14	1.37	1.73×10^{-4}	0.14	8.2×10^{-2}	0.68	0.091
Case 8	5.5	0.21	1.36	4.07×10^{-5}	0.052	3.7×10^{-3}	0.49	0.019
Case 9	13.05	0.21	1.33	9.63×10^{-5}	0.10	2.2×10^{-2}	0.54	0.046
Case 10	13.84	0.10	1.33	2.89×10^{-4}	0.14	2.7×10^{-1}	0.94	0.166
Case 11	9.63	0.21	0.60	7.13×10^{-5}	0.11	2.6×10^{-2}	0.45	0.051
Case 12	7.17	0.42	0.60	1.83×10^{-5}	0.10	1.3×10^{-3}	0.20	0.011
Case 13	5.5	0.21	0.60	4.07×10^{-5}	0.082	8.5×10^{-3}	0.39	0.029
Case 14	4.51	0.21	1.60	3.34×10^{-5}	0.073	2.1×10^{-3}	0.37	0.015
Case 15	5.51	0.14	2.52	7.47×10^{-5}	0.079	8.4×10^{-3}	0.60	0.029
Case 16	6.00	0.14	2.52	8.17×10^{-5}	0.083	9.9×10^{-3}	0.61	0.032
Case 17	9.16	0.21	2.54	6.78×10^{-5}	0.106	5.6×10^{-3}	0.44	0.024
Case 18	9.34	0.14	1.20	1.27×10^{-4}	0.160	5.1×10^{-2}	0.55	0.071
Case 19	5.3	0.05	1.20	3.14×10^{-4}	0.076	5.1×10^{-1}	1.60	0.224
Case 20	6.97	0.42	1.00	1.88×10^{-5}	0.100	7.2×10^{-4}	0.20	0.008
Case 21	9.04	0.21	0.55	6.69×10^{-5}	0.110	2.5×10^{-2}	0.43	0.050
Case 22	8.84	0.21	1.20	6.52×10^{-5}	0.155	1.1×10^{-2}	0.36	0.033
Case 23	9.14	0.21	1.20	6.74×10^{-5}	–	1.2×10^{-2}	–	0.034
Case 24	7.07	0.21	1.60	5.22×10^{-5}	–	5.3×10^{-3}	–	0.023

Table 4.2: Experimental parameters and non-dimensional numbers. The buoyant acceleration is defined as $g' = g(\rho_j - \rho_t)/\rho_t$, with g the gravitational acceleration; the Coriolis parameter is $f = 4\pi/T$, where T is the tank rotation period; Q is the total injection rate; the Ekman transport is $T_{Ek} = (g's/f)\,\delta_{Ek}/2$, where $\delta_{Ek} = \sqrt{2\nu/f}$ is the Ekman-layer thickness; the theoretical intrusion thickness is $H = \gamma h_b$, with $\gamma = (\rho_j - \rho_t)/(\rho_b - \rho_t)$; and the main non-dimensional numbers are $Ro = V_g/(f\mathcal{L})$, $F_v = V_g/\sqrt{g'H}$, and $F_h = V_g/\sqrt{g'\mathcal{L}}$.

Chapter 5

Density Structure of Gravity Currents Intrusions

This chapter is an extended version of the paper "Predicting the vertical density structure of oceanic gravity current intrusions", published in Scientific Reports in 2024 (Rétif et al. 2024[84], also visible in the appendix 8.2).

5.1 Two regimes of intrusion

5.1.1 First observation

In the case of an intrusive gravity current, i.e. when $\rho_t < \rho_j < \rho_b$ (see Subsection 4.2.2), the injected dense water detaches from the slope and intrudes along the pycnocline once it reaches the central deep area, where the vertical density profile is measured using the conductivity probe.

Within this chapter, two intrusion regimes are distinguished. Intrusions of gravity currents appear in the vertical density profiles recorded in the central deep area as a third layer located between the two initially homogeneous layers. However, both the size and the shape of these intrusions vary during an experiment, as shown in fig. 5.1.

It displays three vertical density profiles recorded at the central deep area for different non-dimensional times (t/T). The initial configuration at $t/T = 1$ (solid line) corresponds to the pre-injection state, while the profiles at $t/T = 117$ (dash-dotted line) and $t/T = 152$ (dashed line) show two distinct intrusion structures. At $t/T = 152$, the profile exhibits a curved intrusion with a homogeneous layer between $z = 15\,\mathrm{cm}$ and $z = 25\,\mathrm{cm}$ where $\rho \approx \rho_j$. In contrast, at $t/T = 117$, the intrusion displays an almost linear variation of $\Delta\rho$ with depth over approximately 10 cm.

This linear behaviour produces a plateau in fig. 5.2 (red circles), which shows the distribution of the vertical density gradient as a function of the density anomaly. Each point corresponds to one measurement position of the conductivity probe, equally spaced by $\delta z = 5 \times 10^{-3}\,\mathrm{m}$. The accumulation of values at the edges of each graph indicates vertically homogeneous segments corresponding to the top and bottom layers.

In the initial configuration (black dots in fig. 5.2), the vertical density gradient exhibits a single minimum ($\partial_z \rho \approx -270\,\mathrm{kg\,m^{-4}}$) associated with the pycnocline. During the linear intrusion phase ($t/T = 117$, red circles), the plateau is visible for $1 \leq \Delta \leq 5$. Later, at $t/T = 152$ (blue triangles), the intrusion produces an accumulation of values near ρ_j,

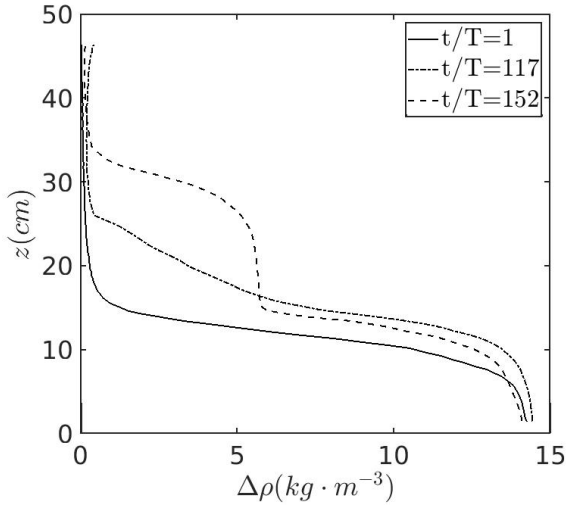

Figure 5.1: Vertical density profiles recorded at $t/T = 1$ (solid line), $t/T = 117$ (dash-dotted line), and $t/T = 152$ (dashed line).

corresponding to a homogeneous intruding layer at the injected density. The transition between the upper layer and this injected layer has a linear slope in fig. 5.2 (the tooth-saw shape of blue triangles), which implies an exponential vertical density profile, consistent with the curvature observed at $t/T = 152$ in fig. 5.1.

Developing an analytical model capable of fitting these observed vertical profiles provides insight into the physical mechanisms shaping the intrusion structure.

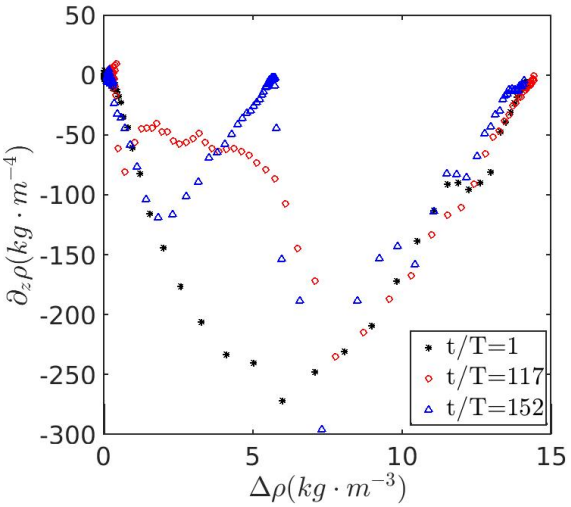

Figure 5.2: Distribution of vertical density gradients as a function of the density anomaly $\Delta\rho$ at three different times: $t/T = 1$ (black dots), $t/T = 117$ (red circles), and $t/T = 152$ (blue triangles).

5.1.2 Model for the vertical density profile

As observed in fig. 5.2, the distribution of $\partial_z\rho$ as a function of $\Delta\rho$ can be accurately fitted using straight-line segments. A piecewise linear fit is obtained by applying linear regressions

over four distinct $\Delta\rho$ domains, bounded by local extrema of $\partial_z\rho$. The resulting fits are shown in fig. 5.3.

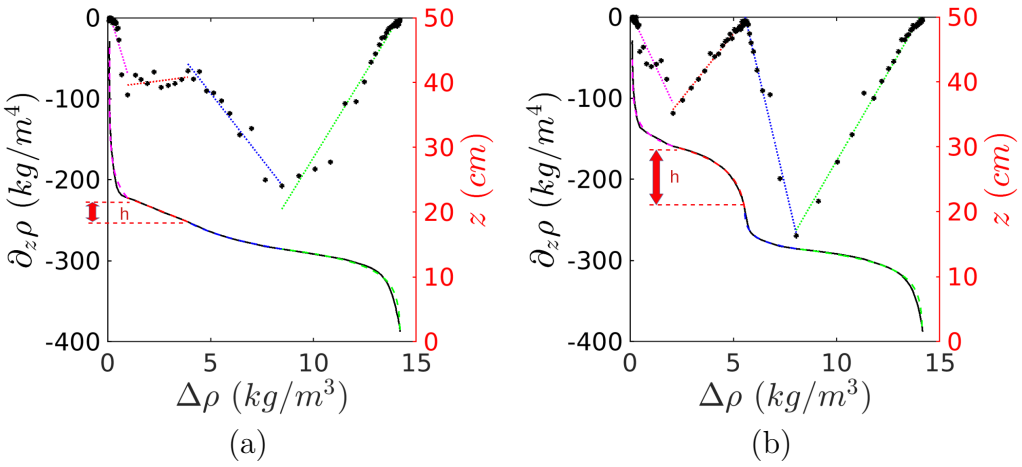

Figure 5.3: Vertical density profiles (red lines) and corresponding vertical density gradients (black stars) for $t/T = 84$ (a) and $t/T = 140$ (b), Case 5. Dashed lines show piecewise exponential fits derived from piecewise linear regressions (dotted lines).

In fig. 5.3, the range of density anomalies $\Delta\rho$ is divided into four domains: (i) the upper layer–intrusion interface (magenta), (ii) the intrusion layer (red), (iii) the transition to the bottom layer (blue), and (iv) the bottom layer (green). Each linear regression takes the general form

$$\partial_z\rho = \alpha\Delta\rho + \beta, \tag{5.1}$$

where α and β are the slope and intercept of the fitted line, respectively. Equation eq. 5.1 is a first-order ordinary differential equation (ODE), whose solution are exponential. To determine $\Delta\rho(z)$, boundary conditions are required. Continuity between adjacent domains is ensured by imposing two boundary conditions for each: $\Delta\rho(z_1) = \Delta\rho_1$ and $\Delta\rho(z_2) = \Delta\rho_2$.

To avoid over-constraining the solution, a two-step approach is used. First, a solution satisfying the lower boundary condition is obtained:

$$\Delta\rho(z) = \frac{\beta}{\alpha} + \left(\Delta\rho_1 - \frac{\beta}{\alpha}\right) e^{\alpha(z_1 - z)}. \tag{5.2}$$

Since $e^{\alpha(z_1-z_1)} = 1$, this solution satisfies $\Delta\rho(z_1) = \Delta\rho_1$. The coefficient β is then adjusted to satisfy the second boundary condition, yielding the general solution:

$$\Delta\rho(z) = \frac{\Delta\rho_2 - \Delta\rho_1 e^{\alpha(z_1-z_2)}}{1 - e^{\alpha(z_1-z_2)}} + \left(\Delta\rho_1 - \frac{\Delta\rho_2 - \Delta\rho_1 e^{\alpha(z_1-z_2)}}{1 - e^{\alpha(z_1-z_2)}}\right) e^{\alpha(z_1-z)}. \tag{5.3}$$

This solution depends on the density values $\Delta\rho_1$, $\Delta\rho_2$ and their corresponding vertical positions z_1, z_2. Applying eq. 5.3 with the appropriate boundary conditions for each of the four domains provides an excellent fit to the measured vertical profiles, as shown in fig. 5.3, where the data almost perfectly overlap the model curves.

A steady one-dimensional description of vertical density structure in the ocean was first proposed by Munk (1966)[64] and later refined by Munk and Wunsch (1998)[65]. The exponential behaviour observed here suggests that a similar balance governs the intrusion

structure in rotating downslope gravity currents. Munk's model assumes a steady-state balance between upward advection (w) and downward diffusion (κ):

$$\partial_z(w\rho) - \partial_z(\kappa\,\partial_z\rho) = 0. \tag{5.4}$$

Integrating eq. 5.4 over z shows that eq. 5.1 can be identified with Munk's formulation, leading to $\alpha = w/\kappa$. Following Wunsch (2023)[119], we define a vertical scale height

$$\tilde{h} = \frac{1}{\alpha} = \frac{\kappa}{w}. \tag{5.5}$$

As seen in fig. 5.3, the intrusion fitted by the red dashed line exhibits a nearly linear rather than exponential structure. In such cases, $\alpha = 1/\tilde{h}$ becomes very small, yielding unrealistically large $\tilde{h}$ values that cannot represent a meaningful thickness. A more robust measure of intrusion thickness, applicable to both linear and exponential profiles, is the vertical extent h of the fitted intrusion layer (red dashed segment).

5.1.3 Detection of Laminar and Turbulent intrusions

In the previous subsection, the scale height $\tilde{h} = \kappa/w$ revealed a link between the observed shape of the intrusion and the balance between diffusivity κ and upward advection w. When the vertical density profile exhibits a nearly linear shape, the fit can be interpreted as an exponential with a very small curvature (large $\tilde{h}$), suggesting dominant diffusion ($\kappa \gg w$). Conversely, for exponential profiles, $\tilde{h}$ remains finite, indicating a significant contribution from both κ and w.

The first type corresponds to a *laminar intrusion*, in which molecular or viscous diffusion dominates and the flow is primarily driven by Ekman dynamics. The second type corresponds to a *turbulent intrusion*, where strong mixing between injected and ambient waters occurs as the dense current cascades downslope before detaching at the pycnocline. For laminar intrusions, the exponential fit theoretically diverges, leading to $h \gg \tilde{h}$.

To distinguish between these two regimes, we introduce the ratio

$$Pe = \frac{h}{\tilde{h}} = \frac{hw}{\kappa} = Re_w \cdot Sc, \tag{5.6}$$

where $Re_w = \frac{hw}{\nu}$ is the Reynolds number based on the vertical advection velocity, and $Sc = \frac{\nu}{\kappa}$ is the Schmidt number comparing momentum and scalar diffusion. This *Péclet number* Pe serves as a criterion to discriminate between laminar ($Pe < 1$) and turbulent ($Pe > 1$) intrusions.

This diagnostic was tested alongside two additional criteria: one based on the distribution of $\partial_z\rho$ versus $\Delta\rho$, and another on the local relative vorticity ζ, as illustrated in fig. 5.4.

Figures 5.4a and 5.4c display the vertical density gradients (black stars) and profiles (red lines) for laminar and turbulent intrusions, respectively. The corresponding vorticity fields are shown in fig. 5.4b and fig. 5.4d.

For turbulent intrusions, dense water cascading downslope induces strong mixing. After detachment at the pycnocline, a well-mixed homogeneous layer forms, producing an accumulation of low-magnitude $\partial_z\rho$ values. A *local-maxima criterion* is thus defined: the number of measurements N_v satisfying $-30 \leq \partial_z\rho \leq 0$ at $\rho = \rho_i \pm 1$ (red box in fig. 5.4c) is counted. If the corresponding vertical extent $h_v = N_v \times 5 \times 10^{-3}$ m exceeds the Ekman layer thickness $\delta_{Ek} = \sqrt{2\nu/f}$, the intrusion is classified as turbulent; otherwise, it is laminar.

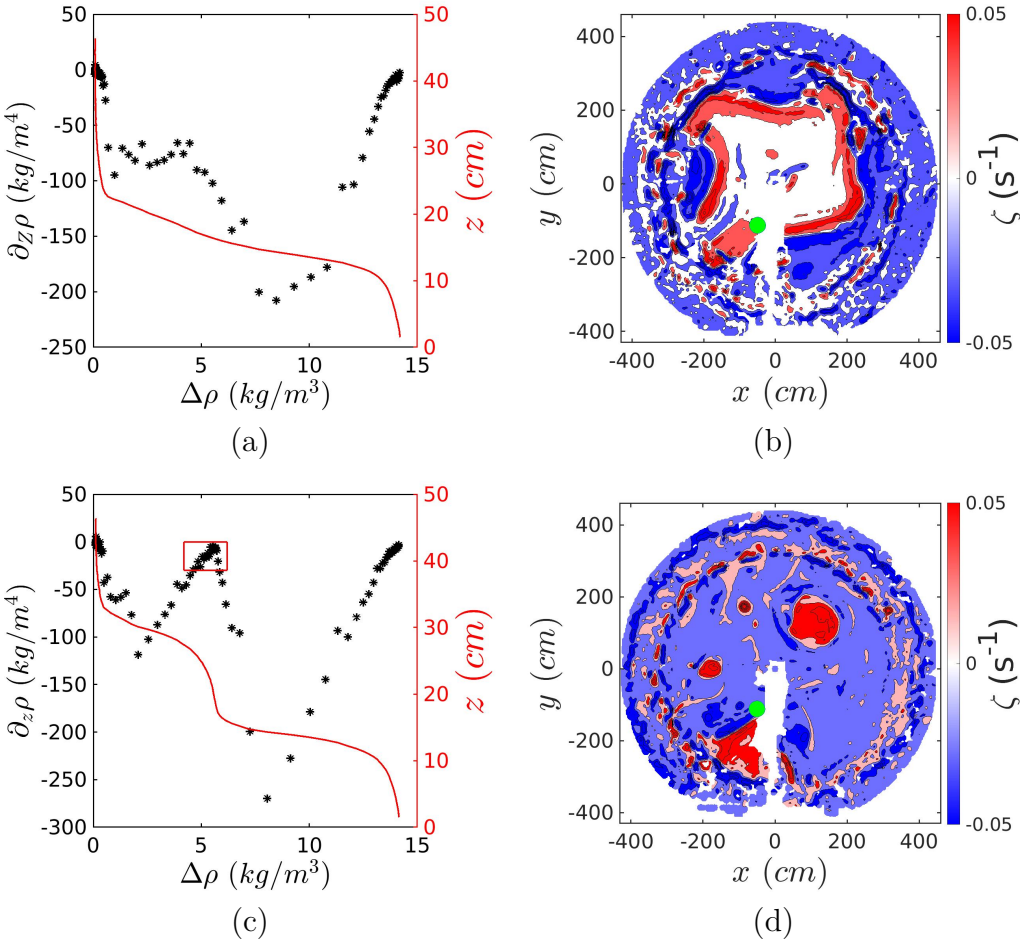

Figure 5.4: (a,c) Same as fig. 5.3 but without fits. The red box in (c) highlights the accumulation of low $\partial_z \rho$ values for the local-maxima criterion, bounded by $\rho = \rho_i \pm 1$ and $-30 \leq \partial_z \rho \leq 0$. (b,d) Horizontal vorticity fields computed from PIV at $z = 15\,\mathrm{cm}$, corresponding to the intrusion level, for Case 5. The green dot indicates the conductivity-probe location.

A second diagnostic is based on the vorticity ζ. In laminar intrusions, dense water escapes the geostrophic flow via Ekman dynamics, detaches at the pycnocline, and feeds a deep boundary current (DBC). This DBC is organised cyclostrophically, as shown in fig. 5.4b, with zones of strong negative vorticity (dark blue) steering the current and inducing meandering. For turbulent intrusions (fig. 5.4d), cascading dense water performs anticyclonic inertial oscillations, disrupting the DBC and confining it within isolated cyclones (red zones). As discussed in A. Tassigny [98], strong negative ζ values are characteristic of turbulent intrusions. Hence, the vorticity-based criterion is summarised as follows: if $\zeta < 0$, the intrusion is turbulent; if $\zeta > 0$, it is laminar.

Using the Pe criterion, intrusion regimes were identified across the 15 experiments. Figure 5.5 presents Hovmöller diagrams of the vertical density profile, where vertical green and red lines mark laminar and turbulent intrusions, respectively.

Turbulent intrusions are visually associated with sudden vertical expansions of the pycnocline. In Case 5, a sequence of laminar intrusions is followed by a period of turbulent ones, due to strong cascading motions that disrupt the DBC (as already visible in fig. 5.4b). In Case 2, laminar and turbulent intrusions occur intermittently, reflecting the meandering behaviour of the DBC.

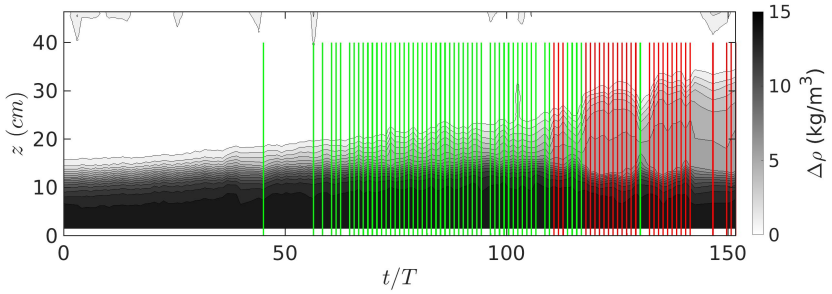

(a)

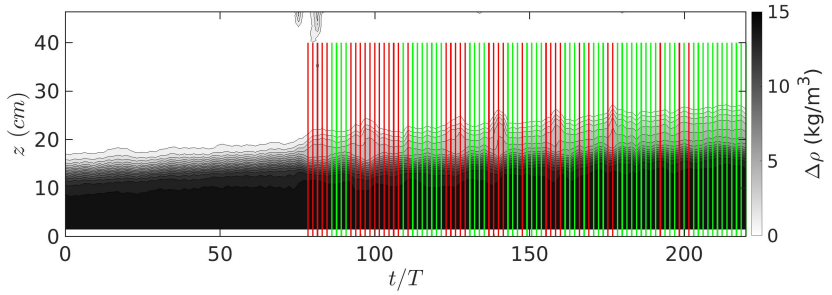

(b)

Figure 5.5: Hovmöller diagrams of vertical density profiles for Case 5 (a) and Case 2 (b). Vertical lines indicate detected intrusion regimes: green for laminar, red for turbulent. In Case 5, a full period of laminar intrusions is followed by a full period of turbulent ones; in Case 2, both regimes alternate intermittently.

5.2 Predicting the thickness of turbulent intrusions

For the 15 experiments considered (see Table 1 in the methodology), each scanning period of the conductivity probe was analysed to detect intrusions on the vertical density profiles. For each detected intrusion, the density structure was fitted, the scale height $\tilde{h}$ and the intrusion thickness h were derived, and the regime (laminar or turbulent) was determined using the three criteria previously defined. The histogram in fig. 5.6 summarises the results obtained with the main criterion based on the Péclet number Pe, compared to the classification made using the local maxima criterion. The mean value obtained for turbulent intrusions is $\langle Pe \rangle = 2.5$.

In this section, we seek a model capable of predicting the average turbulent intrusion thickness over an experiment, using the experimental control parameters. Neither h nor $\tilde{h}$ represent the true physical thickness of the intrusion: h depends on the chosen density interval defining the vertical extension, while $\tilde{h}$ reflects only the curvature of the fitted intrusion layer. Therefore, the mean value $\langle \tilde{h} \rangle$ over each experiment is used as a representative scale to investigate its dependence on the governing parameters.

The graph in fig. 5.7a show $\langle \tilde{h} \rangle$ for 14 experiments with Rossby numbers ranging from $Ro = 10^{-3}$ to $Ro = 4 \times 10^{-2}$. A clear correlation emerges between $\langle \tilde{h} \rangle$ and the rotation rate (through Ro), while the injection flow rate Q and Ekman transport T_{Ek} also contribute. From a linear regression, the following empirical relation is obtained:

$$\tilde{h} \frac{T_{Ek}}{Q_j} = Ro\,\mathcal{C}, \tag{5.7}$$

where $\mathcal{C}$ is a constant coefficient.

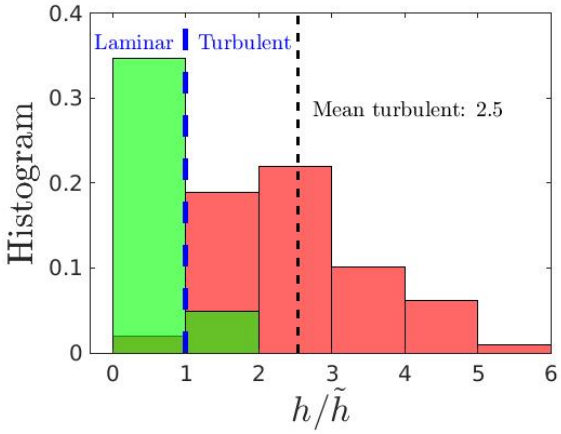

Figure 5.6: Histogram showing laminar intrusions ($h/\tilde{h} < 1$) and turbulent intrusions ($h/\tilde{h} > 1$). The mean value for turbulent intrusions is $\langle Pe \rangle = 2.5$. The green and red shaded regions indicate events classified as laminar and turbulent, respectively, according to the local maxima criterion (see text).

From Wirth (2012)[114], the intrusion thickness can be analytically expressed from the definition of the Froude number:

$$F = \frac{V_g}{\sqrt{g'\tilde{h}}} \quad \Longleftrightarrow \quad \tilde{h} = \frac{V_g^2}{g'F^2} = \frac{g's^2}{F^2 f^2}, \tag{5.8}$$

where the geostrophic velocity $V_g = \frac{g's}{f}$. From the right-hand side of eq. 5.8, the Rossby number $Ro = \frac{V_g}{f\mathcal{L}}$ can be extracted to recover eq. 5.7, with $\mathcal{L} = \frac{Q}{T_{Ek}}$ being the length scale defined by Lane-Serff and Baines (1998)[48], corresponding to the distance required for the Ekman transport to drain the injected flux Q.

The Ekman transport is defined as $T_{Ek} = V_g \delta_{Ek}$. From eq. 5.7 and eq. 5.8, the coefficient $\mathcal{C}$ can be identified as $\mathcal{C} = \frac{s}{F^2}$. The slope of the linear regression in fig. 5.7a gives $F \approx 0.8$, which corresponds to the critical Froude number for flows influenced by both friction and rotation (Wirth 2012[114]; Killworth 2001[45]).

Figure 5.7b reproduces the same distribution as fig. 5.7a but includes the low-rotation experiment (Case 55, $Ro = 0.5$). The geostrophic model (blue triangles) underestimates $\tilde{h}$ in this low-rotation regime. To correct this, the flow velocity is redefined using the gradient balance that includes both geostrophic and cyclostrophic contributions:

$$fV_c + \frac{2V_c^2}{R} = g's, \tag{5.9}$$

where R is the curvature radius of the flow path. Using V_c instead of V_g in the right-hand side of eq. 5.8 improves model predictions, as shown by the red triangles in fig. 5.7b, particularly for low-rotation cases.

To further improve the model, the rotational effect is incorporated into the wave propagation speed that enters the Froude number on the left-hand side of eq. 5.8. The shallow-water wave speed $\sqrt{g'H}$ is replaced by the Poincaré-wave group velocity

$$C_{PC} = \frac{g'\tilde{h}k}{\sqrt{f^2 + g'\tilde{h}k^2}}, \tag{5.10}$$

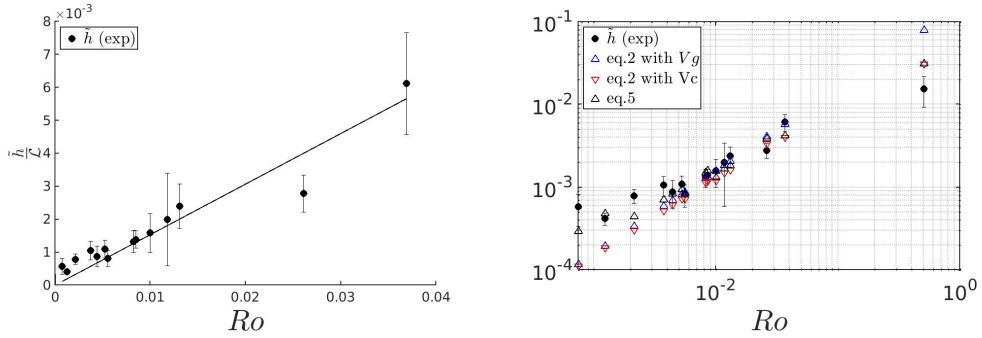

(a) (b)

Figure 5.7: (a) Measured mean scale height $\langle\tilde{h}\rangle$ (black dots) from turbulent intrusions for 14 experiments, excluding the low-rotation case (Case 19, $Ro = 0.51$). The solid line shows a linear regression with slope s/F^2, where $F \approx 0.8$. (b) Same data including Case 55 (black dots), compared with the geostrophic model (blue triangles), the geostrophic–cyclostrophic model ($R = 4\,\mathrm{m}$, red triangles), and the geostrophic–cyclostrophic–Poincaré model ($k = 10\,\mathrm{m}^{-1}$, black triangles).

where k is the wave number. Injecting C_{PC} into eq. 5.8 yields the enhanced model:

$$\tilde{h} = \frac{V_c^2}{2F^2 g'} + \sqrt{\frac{V_c^4}{4g'^2F^4} + \frac{V_c^2 f^2}{g'^2 k^2 F^2}}, \tag{5.11}$$

where $k = 10\,\mathrm{m}^{-1}$ is used as a representative wavelength.

The predictions of this final model (black triangles in fig. 5.7b show good agreement with the experimental data over nearly three decades of Rossby numbers, validating the inclusion of both cyclostrophic balance and Poincaré-wave effects in the description of turbulent intrusion thickness.

5.3 Richardson number analysis in the central area

As presented in the methodology, horizontal velocity is measured on 16 horizontal laser sheets spanning the full domain, so the velocity at the conductivity–probe location can be retrieved. Figure 5.8(a–c) shows vertical profiles of the horizontal speed $|\boldsymbol{U_h}|$ (blue symbols/lines) together with the density–anomaly profile $\Delta\rho$ (black). Figure 5.8(d–f) shows the corresponding velocity direction $\phi = \arctan(v/u)$ (red symbols/lines) alongside $\Delta\rho$ (black). For noise reduction, both velocity and density are averaged over five scanning periods: $t/T \in [\![1, 10]\!]$ in panels (a,d), $t/T \in [\![80, 85]\!]$ in (b,e), and $t/T \in [\![130, 135]\!]$ in (c,f). At the beginning of the experiment (Case 5), fig. 5.8a shows a two–layer stratification without detectable injected water at the probe, but a slight increase of $|\boldsymbol{U_h}| \approx 0.25\,\mathrm{cm\,s}^{-1}$ near the upper layer suggests remote influence of the forming intrusion. When injected water reaches the probe (fig. 5.8b), a clear velocity peak appears, $|\boldsymbol{U_h}| \approx 2\,\mathrm{cm\,s}^{-1}$. Later, a well–mixed third (intrusive) layer forms (fig. 5.8c), with nearly uniform $|\boldsymbol{U_h}| > 1\,\mathrm{cm\,s}^{-1}$ for $z \in [10, 25]\,\mathrm{cm}$; above it, $|\boldsymbol{U_h}|$ decreases but remains significant, indicating that the intrusion drives the overlying fluid. Regarding direction, early–time angles are noisy (small speeds), but $\phi < 0$ generally indicates an inward radial component ($u > 0$) with a geostrophic along–isobath component ($v < 0$). In laminar–intrusion periods (fig. 5.8e), the along–slope/geostrophic component is more pronounced, whereas turbulent intrusions (fig. 5.8f) show a direction more aligned toward the tank centre, consistent with inertia from cascading downslope.

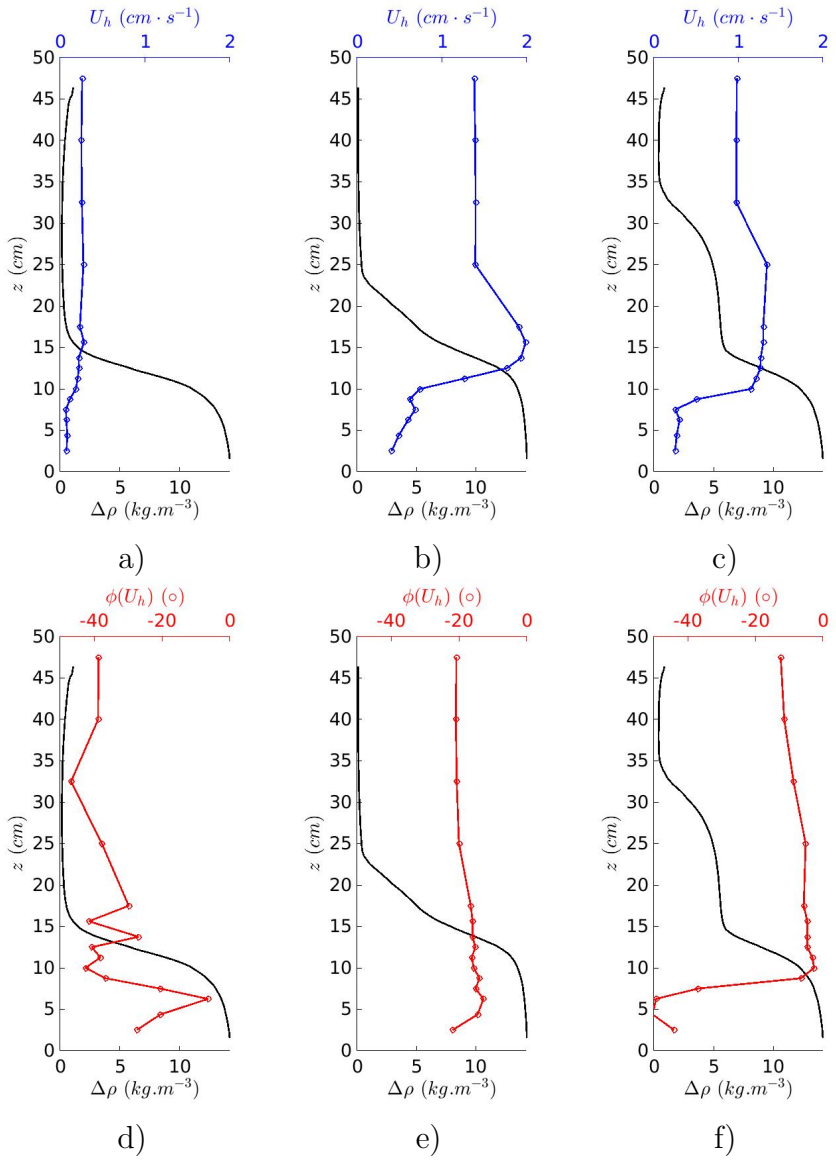

Figure 5.8: Vertical density profiles (black). (a–c) with horizontal speed $|\boldsymbol{U_h}|$; (d–f) with direction $\phi = \arctan(v/u)$.

For stratified flows, the onset of shear instabilities between layers can be assessed using the Richardson number Ri, defined as

$$Ri = -\frac{g}{\rho_t}\frac{\partial_z \rho}{(\partial_z U_h)^2} = \frac{N^2}{(\partial_z U_h)^2}, \tag{5.12}$$

where N is the Brunt–Väisälä frequency. Shear instability, such as Kelvin–Helmholtz waves, typically occurs when $Ri < \frac{1}{4}$. Definition eq. 5.12 requires matching density and velocity data from the conductivity probe and the PIV system. The graphs in fig. 5.9a show the temporal evolution of the vertical positions of the PIV laser sheets (orange rectangles) and the conductivity probe (black points). The two instruments have different vertical resolutions and their scanning periods are not synchronised. To co-locate density and velocity, linear interpolations are performed. As illustrated in fig. 5.9b, a first interpolation is carried out between two density measurements ρ_i^j and ρ_{i+1}^j within scanning period j; the same is done for period j+1. A second interpolation between the two periods then provides an approximate density value at the PIV measurement point (red rectangle in fig. 5.9b). Combining

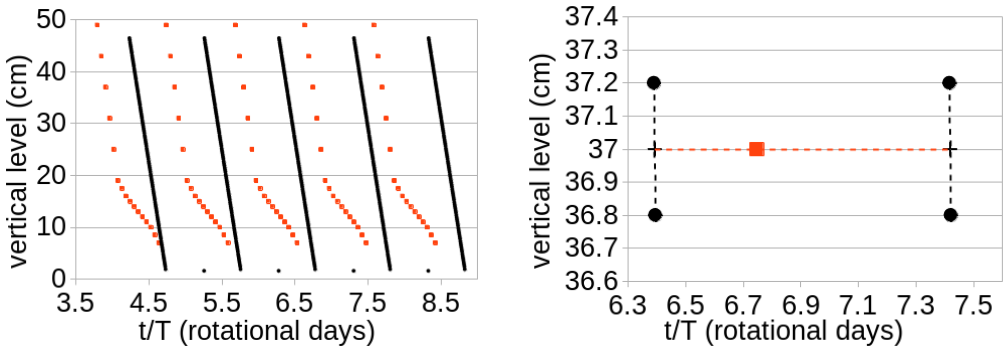

a) b)

Figure 5.9: Temporal evolution of measurement heights. Time is expressed in rotational days t/T, with T the rotation period; the vertical coordinate is in cm. Laser-sheet positions for PIV are plotted in red; conductivity-probe positions in black. (a) Five scanning periods. (b) Example of co-location at one velocity point: density at the same position and time is obtained by two successive linear interpolations—first between two vertical levels within one period, then between two consecutive periods using the first-step results.

co–located velocity (PIV) and density (CTD) data, we compute a discretised bulk Richardson number at the probe location and at the PIV vertical resolution, using the following discretisation. The shear $\partial_z U_h$ is discretised using a first-order forward difference:

$$\partial_z U_h \approx \frac{\sqrt{(u_{j+1}-u_j)^2+(v_{j+1}-v_j)^2}}{\delta z_j}, \tag{5.13}$$

where the spatial resolution δz_j is limited by the spacing between the horizontal laser sheets used for PIV. Similarly, vertical density profiles yield a discrete form of N^2:

$$N_i^2 = -\frac{g}{\rho_t}\frac{(\rho_{i+1}-\rho_i)}{\delta z_i}, \tag{5.14}$$

where δz_i is finer than δz_j. As described above, interpolated values of ρ_i are used to obtain ρ_j at PIV levels, which leads to the discretised (bulk) Richardson number

$$Ri_j = \frac{N_j^2 \cdot (\delta z_j)^2}{U_{h_j}^2} = -\frac{g}{\rho_t}\frac{(\rho_{j+1}-\rho_j)\cdot \delta z_j}{U_{h_j}^2}. \tag{5.15}$$

Hence Ri_j represents a bulk estimate over the layer thickness δz_j.

For Case 5, fig. 5.10a shows the shear $\partial_z U_h$ versus Ri (log–log), with the envelope closely following $\partial_z U_h = 10^{-2}\sqrt{Ri}$ (red line); the stability threshold $Ri = 1/4$ is shown in blue. Figure 5.10b shows weak correlation between Ri and the density gradient alone, indicating that, at the probe, Ri variability is dominated by vertical shear rather than by local changes of $\partial_z \rho$. Importantly, nearly all values satisfy $Ri > 1/4$, implying that shear–instability–driven mixing is inhibited in the central deep area; thus, layer–to–layer exchanges are expected to occur primarily near the slope. To localise potentially vulnerable zones, fig. **??** overlays $Ri < 10$ (green) and $Ri < 1$ (red) on the Hovmöller diagram of density at the probe. Values within nominally homogeneous layers (where $\partial_z \rho < 1\,\mathrm{kg\,m^{-4}}$) are excluded. The smallest Ri are predominantly concentrated at the lower boundary of the intrusion, co–located with enhanced shear. To test whether intrusion–phase mixing occurs mainly on the slope,

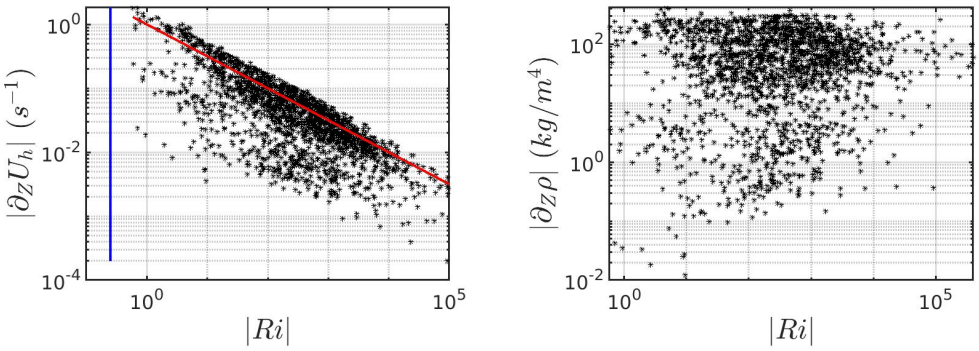

Figure 5.10: Case 5. (a) Shear $\partial_z U_h$ versus Ri (log–log); model line $\partial_z U_h = 10^{-2}\sqrt{Ri}$ (red); stability threshold $Ri = 1/4$ (blue). (b) $\partial_z \rho$ versus Ri shows weak correlation.

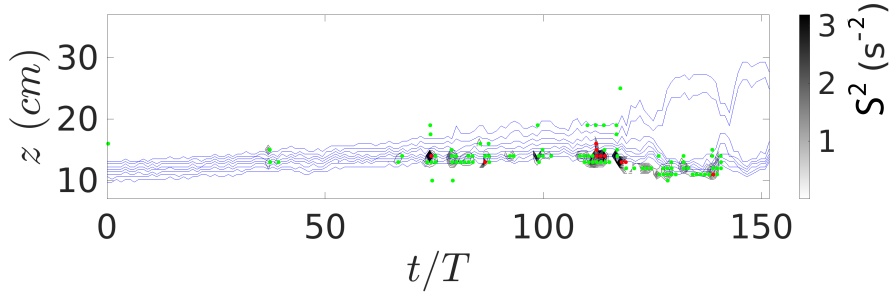

Figure 5.11: Hovmöller diagram of density (Case 5) with $Ri < 10$ (green) and $Ri < 1$ (red). Low Ri cluster along the lower intrusion interface.

fig. 5.12 compares laminar (black) and turbulent (red) intrusion profiles for Case 50, corrected by the pycnocline elevation and with the initial profile removed. Here the injected density is centred between the top and bottom layers ($\rho_b = 1009\,\mathrm{kg\,m^{-3}}$, $\rho_j = 1004.2\,\mathrm{kg\,m^{-3}}$, $\rho_t = 999.6\,\mathrm{kg\,m^{-3}}$), eliminating background asymmetry. Laminar intrusions are symmetric, consistent with weak pre–detachment mixing. Turbulent intrusions are markedly asymmetric: a sharp lower interface (previously leaning on the slope) and a smoother upper interface, consistent with significant near-slope mixing during cascading, followed by advection into the interior characterised by the conservation of the intrusion's density structure.

5.4 Conclusions

By analysing experimental data from vertical density profiles recorded by a conductivity probe in the central deep area, together with horizontal velocity fields measured by PIV at the pycnocline level, two distinct regimes of intrusion of rotating gravity currents into a stratified ambient were identified: (i) *laminar intrusions*, governed by Ekman dynamics, and (ii) *turbulent intrusions*, resulting from enhanced mixing along the slope. Laminar intrusions exhibit a close-to linear vertical density variation, whereas turbulent intrusions display an exponential density profile. Measured Richardson numbers in the central area remain well above the critical threshold of $Ri = 0.25$, confirming that turbulent mixing develops primarily along the slope, while the intrusion within the deep interior remains stably stratified.

Applying the advection–diffusion framework proposed by Munk (1966)[64], we derived the exponential e-folding scale $\tilde{h}$ (the "scale height" of Wunsch 2023[119]) characterising the

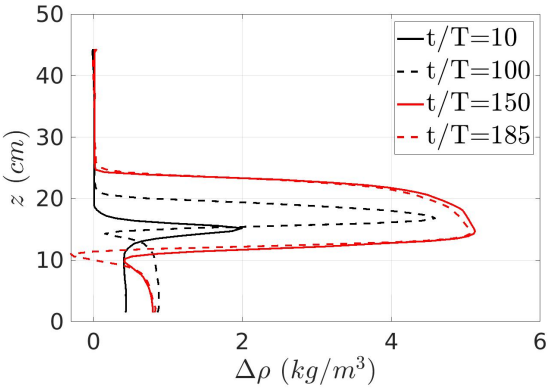

Figure 5.12: Case 50: vertical intrusion profiles at different times for laminar (black) and turbulent (red) events, corrected by the pycnocline elevation. Laminar intrusions are symmetric; turbulent intrusions are asymmetric with a sharper lower interface.

vertical density structure of turbulent intrusions. This balance between upward advection and downward diffusion provides a clear physical distinction between regimes: laminar intrusions correspond to weak vertical motion and diffusion-dominated transport, while turbulent intrusions involve stronger upward advection and enhanced mixing, yielding a pronounced exponential structure. The ratio between the total intrusion thickness and the scale height, expressed as a Péclet number $Pe = h/\tilde{h}$, offers a reliable diagnostic criterion: $Pe < 1$ for laminar intrusions and $Pe > 1$ for turbulent ones. On average, the turbulent intrusion thickness is found to be approximately 2.5 times the scale height, allowing for a clear determination of $\tilde{h}$.

An analytical model based on the critical Froude number accurately predicts the observed scale height across three orders of magnitude in Rossby number, incorporating the effects of slope, rotation, injected flux, and Ekman transport.

Chapter 6

Determining the Ekman-layer thickness in large-scale experiments of downslope rotating gravity currents

This chapter presents an ongoing work in preparation for publication.

6.1 Introduction

The dynamics of the bottom Ekman boundary layer (BBL) governs the exchange of momentum, mass, and tracers between the ocean interior and the seabed. Within this thin near-bottom region, frictional stresses, Coriolis acceleration, pressure gradients and time variability achieve a balance that produces the characteristic veering of currents with depth and cross-isobath transports (Weatherly and Martin 1978[112]; Garrett et al. 1993[26]). This process is central to large-scale circulation, sediment resuspension, and benthic–pelagic coupling across a wide range of oceanic environments (Gross and Nowell 1983[33]; McCave 2008[61]). Despite its apparent conceptual simplicity, the BBL exhibits remarkable complexity, as stratification, turbulence, topography, and wave motions all interact to shape its structure and variability (Trowbridge and Lentz 1991[102]; Brink and Lentz 2010[9]; Umlauf et al. 2015[105]).

The classical Ekman model, first formulated for the ocean surface, has long served as the foundation for understanding boundary-layer flows in a rotating frame (Ekman 1905[19]). Early theoretical extensions to the bottom boundary layer, such as those of Caldwell, Atta, and Helland (1972[10]) and Howroyd and Slawson (1975[39]), focused on turbulent closures and the representation of eddy viscosity, providing some of the first systematic attempts to move beyond constant-viscosity formulations. These studies, together with Lilly (1976), highlighted the role of turbulence parameterisations in capturing vertical momentum transport within rotating boundary layers, a theme that remains central to contemporary modelling efforts (Taylor and Sarkar 2008[100]; Umlauf and Arneborg 2009[103][104]; Zulberti et al. 2023).

Laboratory studies have also been crucial in elucidating the dynamics and structure of the BBL. Classical experiments in homogeneous fluids (Greenspan and Howard 1963[30]; Greenspan 1968) showed that a fluid in a cylindrical container spins up to rigid-body rotation over a timescale $T_s \sim (H^2/(\nu\Omega))^{1/2}$, where H is the fluid depth and Ω the rotation rate. In stratified fluids, spin-up is slower because buoyancy confines secondary circulation near the bottom, restricting the vertical reach of friction (Holton 1965[38][38]; Pedlosky

1967[75]; Walin 1969[111]). Moreover, stratification strongly modifies the BBL structure: theoretical and numerical analyses show that density gradients can thin the boundary layer, alter current veering, and even suppress cross-isobath Ekman transport through "buoyancy arrest" (Price and Sundermeyer 1999[80]; Brink and Lentz 2010[9]). Boyer et al. 2009[8] conducted laboratory experiments to investigate near-bottom flows over a shelf–slope geometry for both homogeneous and linearly stratified fluids, covering regimes from transitional to fully turbulent. In the case of stratified flows, they observed large-scale instabilities that generated slope- and basin-scale eddies, exhibiting a slower decay than in the homogeneous cases. Sous et al. 2013[95] used spin-up/spin-down experiments to examine the neutrally stratified Ekman boundary layer across regimes ranging from turbulent to laminar. PIV measurements showed agreement with classical Ekman theory in the laminar case and with the atmospheric logarithmic law in the turbulent regime.

Parallel advances have come from numerical and observational approaches. Large-eddy simulations (e.g. Taylor and Sarkar 2008[100]; Grooms et al. 2015; Jagannathan et al. 2023[42]) have clarified the role of time dependence, stratification, and topographic interactions in controlling BBL thickness and transport properties. Observational campaigns using moorings, acoustic Doppler current profilers, and microstructure profilers have revealed how near-inertial motions, internal tides, and storm-driven events interact with the BBL to enhance mixing and modify sediment transport (Trowbridge and Lentz 1991[102]; Xie et al. 2023[120]). Maggi et al. 2025[57] extended this line of experimental work by investigating the structure and instabilities of the BBL over a mobile sediment bed, confirming the validity of laminar Ekman theory even in turbulent regimes when molecular viscosity is replaced by a turbulent viscosity, consistent with the results of Sous et al. 2013[95] regarding the dependence of the friction velocity u_* on the Reynolds number based on the BBL thickness. They also elucidated mechanisms of secondary circulation and the role of the BBL in sediment transport and bedform development. Such studies demonstrate the importance of the BBL for sediment dynamics, including the formation of contourite drifts and the resuspension of particles across continental slopes (Rebesco et al. 2014[82]; Sánchez et al. 2023).

Using the experimental dataset of Negretti et al. 2021[67] on downslope intruding gravity currents in the Coriolis rotating platform at high buoyancy Reynolds numbers, Tassigny et al. 2024[99] showed that intrusions into a two-layer stratified ambient exhibit an intrinsic, intermittent turbulent cascading process with no characteristic length scale, suggesting self-organised criticality that dominates vorticity and turbulence in the ambient interior. Using data from the same experimental campaign, Rétif et al. 2024[84] demonstrated that laminar and turbulent intrusions produce different vertical density profiles and scale heights (Wunsch 2023[119]) in the receiving ambient, with turbulent events following an advection–diffusion process. They also developed an analytical model linking these laboratory findings to real-ocean phenomena.

This paper focuses on the structure of the bottom Ekman boundary layer (BBL) over the slope area, characterised by both laminar and intermittent turbulent cascading events identified in Tassigny et al. 2024[99] and Rétif et al. 2024[84], to assess whether these processes can modify the thickness and behaviour of the BBL within the gravity current. For this purpose, we use ADVP velocity data to characterise the BBL across a range of experiments conducted at different rotation rates. We show that, on average, the classical (laminar) Ekman theory accurately predicts the experimentally derived BBL thickness when applying three independent estimation methods. From the turbulent BBL thickness, we extrapolate a turbulent viscosity and find it to remain approximately constant with respect to the Rossby number $Ro = \frac{V_g}{f\mathcal{L}}$. This dimensionless number compares the geostrophic speed V_g with the Coriolis frequency f and the characteristic length scale $\mathcal{L}$, which are further

defined in the methodology section below. Finally, the friction velocity is estimated and shown to scale with Re_δ, consistent with the relationships proposed by Sous et al. 2013[95] and confirmed by Maggi et al. 2025[57].

6.2 Experiments

The detailed experimental setup and measurement techniques are described in Negretti et al. 2021[67]. The essential details relevant to the data analysed in this paper are summarised below.

The Coriolis rotating tank initially contained two discrete water layers of different densities, stably stratified, and is in anticlockwise rotation with a constant period T, corresponding to a Coriolis parameter $f = 2\Omega = 4\pi/T$. Dense water of density ρ_j was injected at a constant flow rate Q through 32 pipes equally spaced around the tank's circumference, positioned 0.5 m from the edge, on an inverted cone of constant slope $s = 0.1$ (see fig. 6.1). We consider here 23 experimental cases with varying Coriolis parameters f and injection flow rates Q (see table 6.1).

The velocity field in the injection region was measured using an Acoustic Doppler Velocimetry Profiler (ADVP, Vectrino) to characterise the gravity current along the slope and the associated Ekman boundary layer. The ADVP is better suited than PIV for resolving near-bottom flows, and the PIV seeding particles simultaneously served as tracers for the ADV measurements. The instrument was mounted 1.1 m from the tank edge on a traversing system operating along a 1 m radial path between two adjacent injectors (see fig. 6.1). Measurements were taken continuously at 200 Hz, at 10 cm intervals, over a total acquisition time of 65 s per scanning period T_{scan}. All three velocity components (u, v, w) were recorded in a local coordinate system (x, y, z) aligned with the slope, within a vertical section extending up to $z = 3.2$ cm above the bottom, with a vertical resolution of 0.2 cm.

We consider an Ekman layer developing beneath the main geostrophic flow (also called the "vein", following Wirth 2009[113]), which transports water downslope. This Ekman transport is defined as $T_{Ek} = V_g \delta_{Ek}^{lam}/2$, where $V_g = g's/f$ is the geostrophic speed, fully defined by the reduced gravity $g' = g\frac{\rho_j - \rho_t}{\rho_t}$, the slope $s = 0.1$ and f (Nof 1983[70]). The vertical length $\delta_{Ek}^{lam} = \sqrt{2\nu/f}$ is the theoretical laminar Ekman layer thickness where $\nu = 10^{-6}\,\mathrm{m^2\,s^{-1}}$ is the laminar molecular viscosity. From the transport T_{Ek}, we define a horizontal length scale $\mathcal{L} = Q/T_{Ek}$, representing the characteristic distance over which the flow is entirely drained from the veine through the Ekman layer. A Rossby number $Ro = V_g/(f\mathcal{L})$ based on the drainage scale $\mathcal{L}$ is then derived, along with a Reynolds number $Re_\delta = V_g \delta_{Ek}^{lam}/\nu$ based on the vertical scale δ_{Ek}^{lam}.

6.3 Results

6.3.1 Near-slope vertical velocity profiles

Vertical profiles of the radial and azimuthal velocity components (u, v) (red and blue circles, respectively) for experimental Case 6 at $t/T \approx 33$ are shown in fig. 6.2a. The maximum velocity occurs at $z \approx 5 \times 10^{-3}$ m, and for larger z, it approaches the asymptotic values U_∞ and V_∞. These velocity profiles can be fitted using the classical laminar Ekman theory (see

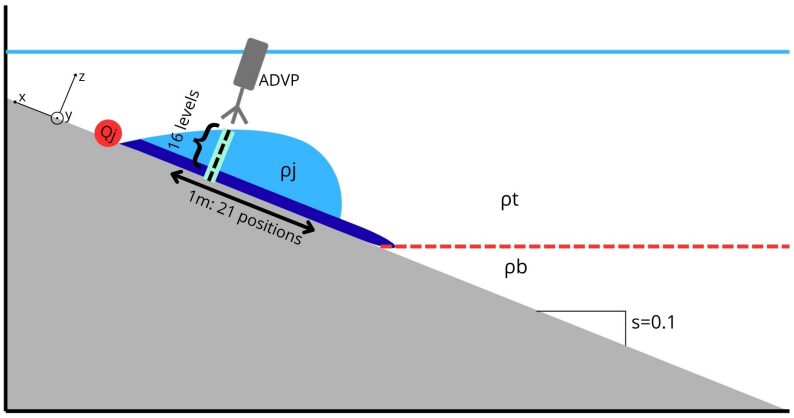

Figure 6.1: Schematic of the experimental setup. In a stably stratified two-layer ambient ($\rho_b > \rho_t$), a salt solution with density ρ_j is injected at the sources (in red) with a flow rate Q. A geostrophic vein (in blue) develops along the downslope ($s = 0.1$), and a frictional layer, the Ekman layer (in dark blue), transports water downslope toward the pycnocline. Using an Acoustic Doppler Velocimetry Profiler (ADVP), vertical velocity profiles are measured near the slope over 16 levels (green zone) and across 21 positions along a 1 m radial path.

Ekman 1905[19]):

$$u_{Ek} = U_\infty(1 - e^{-z/\delta_{Ek}}\cos(z/\delta_{Ek})) - V_\infty e^{-z/\delta_{Ek}}\sin(z/\delta_{Ek}) \tag{6.1}$$

$$v_{Ek} = V_\infty(1 - e^{-z/\delta_{Ek}}\cos(z/\delta_{Ek})) + U_\infty e^{-z/\delta_{Ek}}\sin(z/\delta_{Ek}), \tag{6.2}$$

shown as solid lines in fig. 6.2a. The geostrophic velocity component v predominates over the downslope radial component u, indicating that the flow near the topography is driven by an upper geostrophic gravity current. The hodograph in fig. 6.2b displays a spiral pattern that is well predicted by Ekman theory (solid line). Not all velocity profiles exhibit such spirals, as the velocity above the slope, outside the Ekman layer, cannot always be clearly identified owing to the stratified upper layer, which prevents the development of a Taylor–Proudman column. Nevertheless, a spiral structure is still observed in most profiles, and we define $V_{max} = \max(\sqrt{v^2 + u^2})$ as the maximum velocity magnitude, indicated by the red arrow in fig. 6.2b.

The influence of the Rossby number Ro on the maximum velocity magnitude, measured from the velocity profiles and averaged over the full duration of each experiment, is shown in fig. 6.3. The figure presents V_{max}, normalised by V_g, as a function of the rotational period t/T for six experimental cases: Case 12 ($Ro = 0.0013$, cyan), Case 17 ($Ro = 0.0056$, blue), Case 16 ($Ro = 0.0099$, green), Case 10 ($Ro = 0.2740$, purple), and the weakly rotating experiment Case 19 ($Ro = 0.5048$, red). In fig. 6.3, the magnitude V_{max} in the most rapidly rotating case, Case 12 ($Ro = 0.0013$), exceeds the geostrophic velocity V_g, due to inertial oscillations that locally produce exceeding values.

The ratio is generally lower than 1, with $V_{max}/V_g \approx 0.8$ for Case 16 and Case 17, which is consistent with expectations for rotating gravity currents (see Rétif et al. 2024[84], Wirth 2012[114], Killworth 2001[45]. However, for Case 10 and Case 19, this ratio decreases significantly to values below 0.25, indicating that these weakly rotating experiments do not lead to rotating gravity currents. Specifically, Case 10 corresponds to a bottom-intrusive

Experiment	T (s)	g' (cm/s^2)	Q $(liter/s)$	f (s^{-1})	U_{inj} cms^{-1}	V_g cms^{-1}	Ro $(-)$	Re_δ $(-)$
Case 2	60	6.09	1.19	0.209	14.6	2.9	0.0052	38
Case 3	60	5.50	1.15	0.209	14.1	2.6	0.0044	36
Case 5	90	5.10	1.39	0.140	17.1	3.7	0.0130	12
Case 6	90	4.81	1.37	0.140	16.8	3.4	0.0117	56
Case 7	90	12.75	1.37	0.140	16.8	9.1	0.0824	62
Case 8	60	5.50	1.36	0.209	16.7	2.6	0.0037	32
Case 9	60	13.05	1.33	0.209	16.3	6.2	0.0215	44
Case 10	120	13.84	1.33	0.105	16.3	13.2	0.2740	58
Case 11	60	9.63	0.60	0.209	7.4	4.6	0.0260	14
Case 12	30	7.17	0.60	0.419	7.4	1.7	0.0013	7
Case 13	60	5.50	0.60	0.209	7.4	2.6	0.0085	19
Case 14	60	4.51	1.60	0.209	19.6	2.2	0.0021	40
Case 15	90	5.51	2.52	0.140	30.9	3.9	0.0084	109
Case 16	90	6.00	2.52	0.140	30.9	4.3	0.0099	110
Case 17	60	9.16	2.54	0.209	31.2	4.4	0.0056	88
Case 18	90	9.34	1.20	0.140	14.7	6.7	0.0505	62
Case 19	240	5.30	1.20	0.052	14.7	10.1	0.5048	70
Case 20	30	6.97	1.00	0.419	12.3	1.7	0.0007	16
Case 21	60	9.04	0.55	0.209	6.8	4.3	0.0250	12
Case 22	60	8.84	1.20	0.209	14.7	4.2	0.0110	44
Case 23	60	9.14	1.20	0.209	14.7	4.4	0.0117	43
Case 24	60	7.07	1.60	0.209	19.6	3.4	0.0053	66

Table 6.1: Experimental parameters are rotation period T, reduced gravity g', and injection rate Q. Derived parameters are the Coriolis parameter $f = 4\pi/T$, and injection velocity $U_{inj} = \frac{Q}{32\pi\left(\frac{D}{2}\right)^2}$, where $D = 1.6\,\text{cm}$ is the diameter of the 32 injection tubes. The geostrophic speed $V_g = g's/f$ with the slope $s = 0.1$, the Rossby number $Ro = V_g/f\mathcal{L}$ based on the horizontal length scale $\mathcal{L}$, and the Reynolds number $Re_\delta = V_g\delta_{Ek}^{lam}/\nu$ based on the laminar Ekman layer thickness δ_{Ek}^{lam} are also reported.

configuration with a higher reduced gravity g', while Case 19 rotates too slowly for the resulting currents to be regarded as rotating gravity currents. Negative radial velocities u were observed in most cases, highlighting that gravity drives the current downslope. In contrast, rapidly rotating experiments exhibited upslope velocities associated with local recirculation.

6.3.2 Estimation of the Ekman layer thickness

To determine the Ekman layer thickness δ_{Ek} from vertical velocity profiles measured near the slope, 3 independent methods are used.

Method 1

While the previous method focused on the local maxima of the azimuthal velocity profile $v(z)$, this second method considers both $u(z)$ and $v(z)$, and in particular the corresponding velocity fluctuations $u' = u - U_\infty$ and $v' = v - V_\infty$ from their asymptotic values U_∞ and V_∞. In the theoretical expressions eq. 6.1 and eq. 6.2, δ_{Ek} appears in both the exponential and

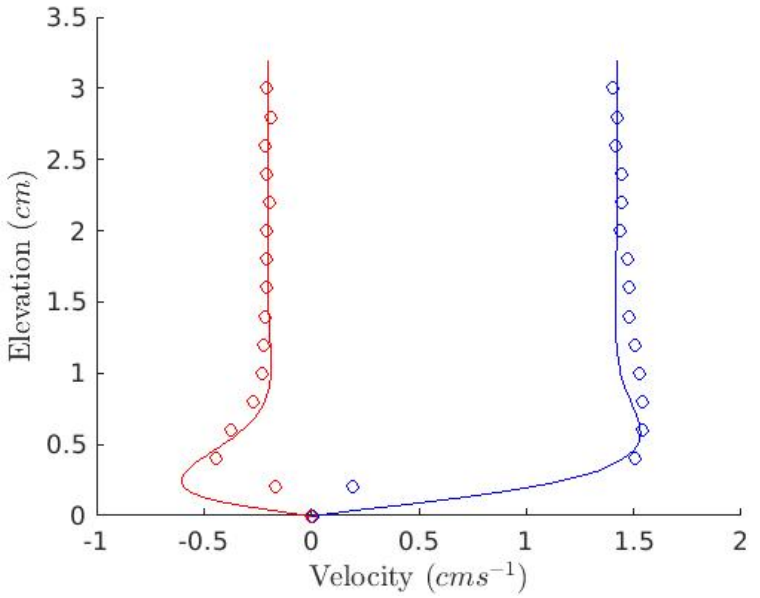

(a)

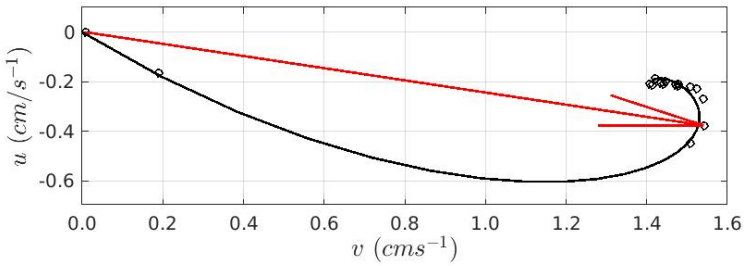

(b)

Figure 6.2: For experimental Case 6, $t/T \approx 33$: (a) Radial and azimuthal velocity components, $u(z)$ (red circles) and $v(z)$ (blue circles). Solid lines represent the corresponding theoretical Ekman velocity profiles, u_{Ek} and v_{Ek}, based on eq. 6.1 (red line) and eq. 6.2 (blue line). (b) Hodograph showing the velocity vectors composed of u (radial) and v (azimuthal) components across all measured vertical levels. The radial velocity is nearly an order of magnitude smaller than the azimuthal component. The solid black line represents the theoretical model from eq. 6.1 and eq. 6.2. The red arrow indicates the maximum velocity magnitude $V_{max} = \max(\sqrt{v^2 + u^2})$.

trigonometric terms. To eliminate the sine and cosine dependencies, the square sum of the fluctuations is considered:

$$(u')^2 + (v')^2 = e^{-2z/\delta_{Ek}}(U_\infty^2 + V_\infty^2). \tag{6.3}$$

Thus, we obtain the thickness

$$\delta_{Ek} = -2z \frac{1}{\ln \frac{(u')^2+(v')^2}{U_\infty^2+V_\infty^2}}. \tag{6.4}$$

A distribution of $\ln \frac{(u')^2+(v')^2}{U_\infty^2+V_\infty^2}$ against the vertical coordinate z, as shown in fig. 6.4, provides a slope $\mathcal{K} = -2/\delta_{Ek}$ after performing a linear regression. The plot in fig. 6.4a shows a perfectly linear behaviour (black stars), when the velocity profile is generated from the

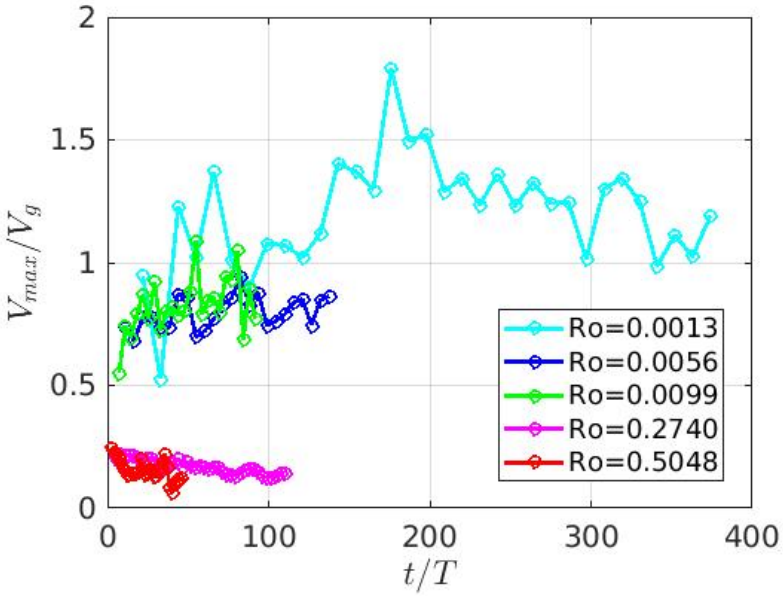

Figure 6.3: Time evolution (in rotational days, t/T) of the maximum flow magnitude $V_{max} = \max(\sqrt{v^2 + u^2})$, normalised by the geostrophic speed V_g, for five experimental cases corresponding to five different Rossby numbers $Ro = V_g/f\mathcal{L}$.

theoretical Ekman model eq. 6.1 and eq. 6.2 where U_∞, V_∞, and δ_{Ek} are known, and confirms that $\delta_{Ek} = -2/\mathcal{K}$. From an observed velocity profile, averaged over the full experiment Case 7, a similar graph is presented in fig. 6.4b. When $U_\infty = \langle u \rangle_z$) and $V_\infty = \langle v \rangle_z$ (red stars), the linear fit is not consistent over all vertical levels z. To obtain a linear relationship (black stars), a *brute-force* algorithm was used to identify the pair (U_∞, V_∞) that maximises the coefficient of determination R^2 of the linear regression across the full z-range. The resulting values of U_∞ and V_∞ are then retained for use in the other methods. Error bars are determined from the dispersion around the linear regression performed on the aligned distribution (black stars on fig. 6.4b).

Method 2

The analytical expressions eq. 6.1 and eq. 6.2 for the radial $u_{Ek}(z)$ and azimuthal $v_{Ek}(z)$ velocity components involve the Ekman layer thickness δ_{Ek}. To estimate δ_{Ek} from the observed velocity profiles $u(z)$ and $v(z)$, we identify the vertical position of the maximum of $v(z)$, z_{max}. Using eq. 6.2, the Ekman thickness is then expressed as:

$$\delta_{Ek} = \frac{z_{max}}{\pi + \tan^{-1}\left(\frac{V_\infty - U_\infty}{V_\infty + U_\infty}\right)}, \tag{6.5}$$

where U_∞ and V_∞ represent the asymptotic (i.e. above the Ekman layer) values of the radial and azimuthal velocity components, respectively. Determining these coefficients is challenging, as the observed profiles do not always converge towards asymptotic values. In practice, while the gravity current interacts with the slope to form a bottom friction layer, it simultaneously interacts with the overlying fluid, likely producing an interfacial velocity structure. The asymptotic velocity components U_∞ and V_∞ are determined as in Method 1. For each experiment, error bars are bounded by the thickness estimates from eq. 6.5, com-

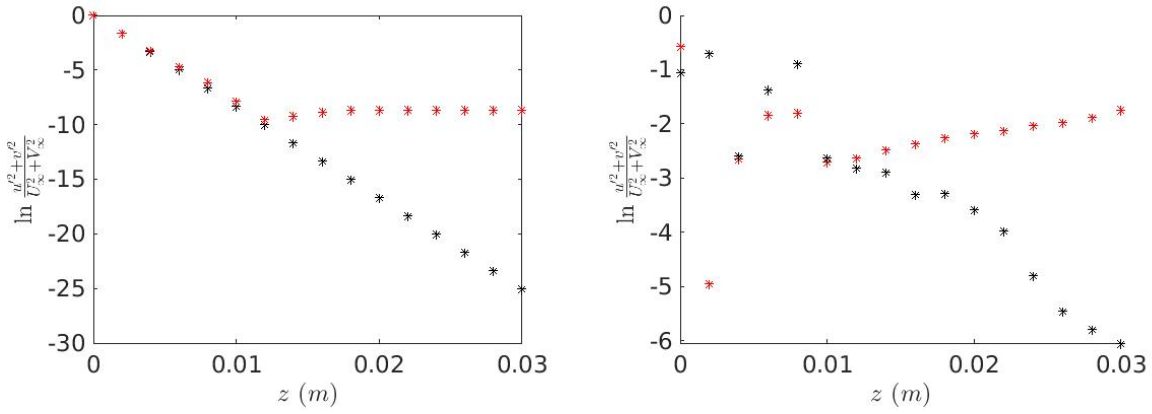

(a) (b)

Figure 6.4: $\ln \frac{(u'_{Ek})^2+(v'_{Ek})^2}{U_\infty^2+V_\infty^2}$, plotted as a function of the vertical position z. (a) Theoretical velocity profiles u_{Ek} and v_{Ek} (eq. 6.1 and eq. 6.2) for two configurations: $U_\infty = \langle u \rangle_z$ and $V_\infty = \langle v \rangle_z$ (red stars), and the exact values used in u_{Ek} and v_{Ek} (black stars). (b) Same as (a), but using observed velocity profiles u and v; the optimal configuration for U_∞ and V_∞ is determined by aligning the data points (black stars) using a *brute-force* algorithm which maximises the coefficient of determination R^2 gotten from the linear regression.

puted using $(U_\infty, V_\infty) = (\min(u(z), \max(v(z))$ and $(U_\infty, V_\infty) = (\max(u(z), \min(v(z))$, as the main uncertainty remains in the estimation of U_∞ and V_∞.

Method 3

This method aims to compute δ_{Ek} without using the assymptotic velocity U_∞ and V_∞, starting from eq. 6.1 and eq. 6.2:

$$\begin{aligned} -f(u - U_\infty) &= \nu \partial_{zz} v, \\ f(v - V_\infty) &= \nu \partial_{zz} u, \end{aligned} \tag{6.6}$$

To remove U_∞ and V_∞, the system in eq. 6.6 is differentiated with respect to z, which involves third z derivatives. After adding the square of the two components, an expression for δ_{Ek} is obtained:

$$\widehat{\delta_{Ek}}^4 = 4 \frac{(\partial_z u)^2 + (\partial_z v)^2}{(\partial_{zzz} u)^2 + (\partial_{zzz} v)^2}. \tag{6.7}$$

The third derivatives with respect to z are discretised using a non-centred finite-difference approximation:

$$\partial_{zzz} u(z) \approx \widehat{u_{zzz}} = \frac{-u(z) + 3u(z + \Delta z) - 3u(z + 2\Delta z) + u(z + 3\Delta z)}{z + \Delta z^3}, \tag{6.8}$$

while the first derivative ∂_z is discretised using a forward finite-difference:

$$\partial_z u(z) \approx \widehat{u_z} = \frac{u(z + \Delta z) - u(z)}{\Delta z}. \tag{6.9}$$

The Ekman layer thickness δ_{Ek} is obtained as the mean value over the $\widehat{\delta_{Ek}}$ values computed at the first 2 vertical levels. Error bars are bounded by their two corresponding thickness values $\widehat{\delta_{Ek}}$. Second order numerical error has been quantified, calculations are further detailed in the section 8.1 of the appendix, leading to the relative error

$$\frac{\widehat{\delta_{Ek}} - \delta_{Ek}}{\delta_{Ek}} = \frac{\Delta_z}{2\delta_{Ek}} + O(\Delta z^2), \tag{6.10}$$

where δ_{Ek} is the theoretical Ekman thickness we want to estimate. This bias is always positive, meaning that the Method 3 overestimates the real thickness of about $\Delta z/2$, and results obtained with Method 3 are therefore corrected.

6.3.3 A measure of the Ekman layer thickness

Theory suggests that the Ekman-layer thickness is only a few millimetres and thus at the limit of what is measurable with the vertical resolution of 2 millimetres. We therefore compared the three independent methods to determine the Ekman layer thickness δ_{Ek}. In fig. 6.5a, δ_{Ek} estimated from the three methods is shown as a function of f. Error bars represent the uncertainties associated with each method, as further detailed in subsection 6.3.2. The three methods have been applied to the velocity profiles $\langle\overline{u}\rangle$ and $\langle\overline{v}\rangle$, averaged over all horizontal positions R_{scan} ($\langle\rangle$) and time steps T_{scan}($^-$). Method 2 yields values that lie mostly below the theoretical relation δ_{Ek}^{lam} (solid line). Method 1, based on velocity fluctuations u'_{Ek} and v'_{Ek} (see sub-section6.3.2), gives values above the theoretical prediction, while Method 3 produces values distributed around the theoretical laminar model. The three methods provide consistent results in terms of order of magnitude and overall trend, indicating that the Ekman layer thickness can be reliably estimated from Ekman spiral modelling. Error bars, determined for each experiment depending on the method used (see sub-section 6.3.2), result in uncertainties that are relatively small compared to the vertical resolution $\Delta z = 2 \times 10^{-3}$ m. For Method 2, the average thickness of the error bar spans 9×10^{-4} m, with a maximum value of 14×10^{-4} m; for Method 1, the average thickness is 16×10^{-4} m, with a maximum of 48×10^{-4} m; and for Method 3, the average thickness is 17×10^{-4} m, with a maximum of 32×10^{-4} m. To better visualise and compare the trends obtained from these methods, fig. 6.5b presents results averaged over experiments conducted at the same rotation rate. Error bars correspond to the mean uncertainties across all experiments. A similar trend is observed between Method 2 and Method 3. We notice that the correction applied in Method 3, which compensates for part of the numerical error, significantly alters the values. Indeed, for most experiments, the uncorrected values fall outside the error bars determined from the uncertainties in the velocity profiles. It is also observed that Method 1 systematically overestimates δ_{Ek} compared with Method 2 and Method 3.

From δ_{Ek} values presented in fig. 6.5a, the viscosity $\nu_t = f\langle\overline{\delta_{Ek}}\rangle^2/2$ is extracted, giving $\nu_t/\nu \approx 1$ for Method 3, 0.5 for Method 2, and 5 for Method 1. As already mentioned, the three methods have been applied to velocity profiles averaged over the entire experiment, as such profiles are smoother and less noisy than individual profiles. However, computing δ_{Ek} at each radial position R_{scan} and scanning period $T_{scan} \approx 5.5$ min recorded by the ADVP in both space and time allows the variations of this thickness to be investigated throughout an experiment. The resulting thickness values can then be averaged in time and space, leading to a single representative value $\langle\overline{\delta_{Ek}}\rangle$ that characterises the experiment. This methodology has been applied but produced results that were too scattered when

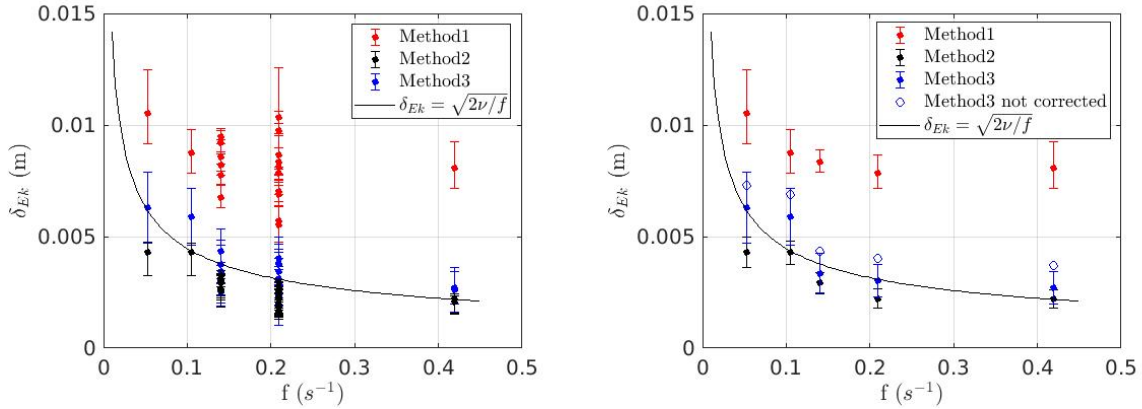

Figure 6.5: Ekman layer thickness δ_{Ek} computed from the velocity components $\langle\overline{u(z)}\rangle$ and $\langle\overline{v(z)}\rangle$, averaged over scanning periods and horizontal positions, plotted as a function of f, for the three methods detailed in sub-section 6.3.2: Method 1 (red), Method 2 (black), and Method 3 (blue). The solid line represents the laminar prediction δ_{Ek}^{lam}. (a) Results are shown for all experiments; error bars are computed from the uncertainties detailed in sub-section 6.3.2. (b) Results are averaged over each f value, and error bars are averaged accordingly; blue circles are averaged results from Method 3 before correction (see 6.3.2).

using Method 1. Comparisons between values, each obtained from profiles $\langle u(z)\rangle$ and $\langle v(z)\rangle$ averaged over scanning periods and horizontal positions, and those based on $\langle\overline{\delta_{Ek}}\rangle$ where the thickness values are obtained from every single profiles before being averaged over scanning periods and horizontal positions, led to similar results for Method 2, whereas for Method 3, $\langle\overline{\delta_{Ek}}\rangle$ was clearly smaller, lying below the theoretical laminar value δ_{Ek}^{lam}. Using estimates of U_∞ and V_∞ (see subsection 6.3.2), δ_{Ek} is computed for all single velocity profiles using Method 2. To investigate possible patterns between δ_{Ek} and R_{scan} or T_{scan}, Hovmöller diagrams are presented in fig. 6.6 for five rotation rates: $f = 0.419\,\mathrm{s}^{-1}$ (Case 20), $f = 0.209\,\mathrm{s}^{-1}$ (Case 17), $f = 0.140\,\mathrm{s}^{-1}$ (Case 16), $f = 0.105\,\mathrm{s}^{-1}$ (Case 10), and $f = 0.052\,\mathrm{s}^{-1}$ (Case 19).

No clear dependence of δ_{Ek} on either R_{scan} or T_{scan} is observed.

We also identified events where $\delta_{Ek} > \delta_{Ek}^{lam}$, i.e. cases where the derived viscosity ν_t exceeds the molecular value ν, which are outlined in fig. 6.6 with black contours. It is observed that within regions where $\delta_{Ek} > \delta_{Ek}^{lam}$, the thickness δ_{Ek} intensifies as f decreases. However, the number of occurrences of such events, N_{turb}, does not appear to be correlated with f.

However, linear correlations between $\langle\overline{\delta_{Ek}}\rangle$ and the rate N_{turb}/N_{Ek} are observed in fig. 6.7a for two clusters corresponding to $f = 0.209\,\mathrm{s}^{-1}$ (12 experimental cases) and $f = 0.140\,\mathrm{s}^{-1}$ (6 experimental cases), where N_{turb} is normalised by the total number of measurements N_{Ek}. The two linear regressions yield similar slopes, α, suggesting that the correlation between $\langle\overline{\delta_{Ek}}\rangle$ and N_{turb}/N_{Ek} does not vary significantly with the rotation rate f. The slope α is then used to extrapolate $\langle\overline{\delta_{Ek}}\rangle$ values for the other rotation rates f (dashed lines coloured by f).

The right panel, fig. 6.7b, shows the corrected mean Ekman layer thickness, computed as $\alpha \cdot \left(\frac{N_{turb}^{target}}{N_{Ek}} - \frac{N_{turb}}{N_{Ek}}\right) + \langle\overline{\delta_{Ek}}\rangle$, for target values of $\frac{N_{turb}^{target}}{N_{Ek}} = 0\%$ (black stars); 40% (black stars), for which the values approach the theoretical δ_{Ek}^{lam} (black line); and 100%, corresponding to an extrapolation where all recorded profiles satisfy $\delta_{Ek} > \delta_{Ek}^{lam}$.

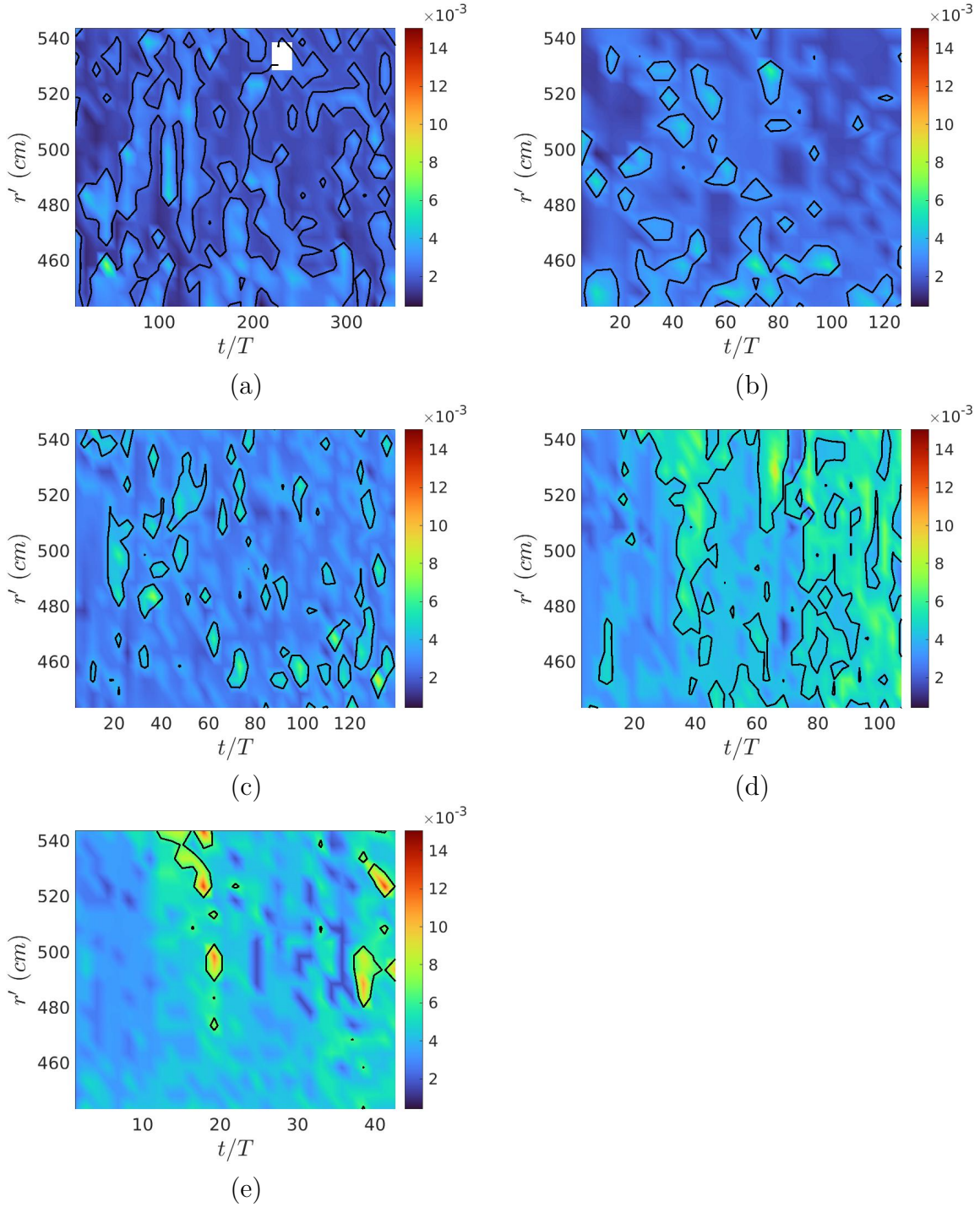

Figure 6.6: Hovmöller diagrams for five experimental cases: Case 20 (a: $f = 0.419\,\mathrm{s}^{-1}$), Case 17 (b: $f = 0.209\,\mathrm{s}^{-1}$), Case 6 (c: $f = 0.140\,\mathrm{s}^{-1}$), Case 10 (d: $f = 0.105\,\mathrm{s}^{-1}$), and Case 19 (e: $f = 0.052\,\mathrm{s}^{-1}$). The horizontal axis corresponds to the scanning period T_{scan}, while R_{scan} denotes the radial positions. The colour map shows the Ekman layer thickness δ_{Ek} (in metres), estimated using Method 2 based on the local extrema of the azimuthal velocity v and the asymptotic velocity components U_∞ and V_∞.

A possible interpretation is that the spread observed in $\langle\overline{\delta_{Ek}}\rangle$ for constant f can be explained as follows: the rotational effect influences the characteristic Ekman layer thickness but does not significantly affect the occurrence of turbulent events. This behaviour was also

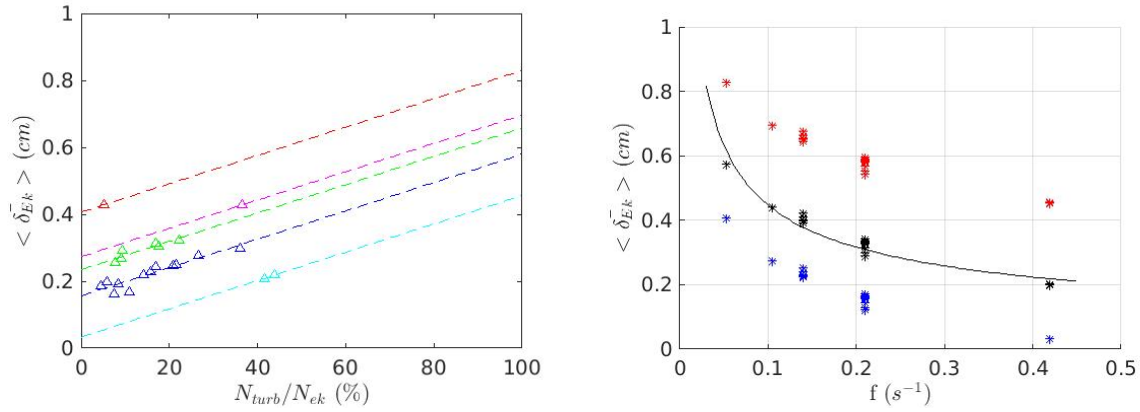

Figure 6.7: (a) Mean Ekman layer thickness $\langle\overline{\delta_{Ek}}\rangle$ plotted against the proportion of turbulent events, expressed as the ratio N_{turb}/N_{Ek}, where N_{turb} is the number of instances where $\delta_{Ek}^{turb} > \delta_{Ek}^{lam}$, and N_{Ek} is the total number of estimated values. Each triangle represents an experimental case, coloured according to the rotation rate f, forming identifiable clusters. The dashed blue and green lines show linear regressions of the form $\alpha\frac{N_{turb}}{N_{Ek}} + b$. The slopes obtained from these fits are similar, and their mean value α is used to extrapolate linear trends for other rotation rates. (b) Corrected mean Ekman layer thickness, computed as $\alpha \cdot \left(\frac{N_{turb}}{N_{Ek}}^{target} - \frac{N_{turb}}{N_{Ek}}\right) + \langle\overline{\delta_{Ek}}\rangle$, for target rates of $\frac{N_{turb}}{N_{Ek}}^{target} = 0\%$ (blue stars); 40% (black stars), which matches the laminar theoretical prediction δ_{Ek}^{lam} (black solid line); and 100% (red stars), which allows determination of the turbulent viscosity ν_t by extrapolation.

reported by Rétif et al. (2024)[84], where no dependence of the proportion of turbulent versus laminar intrusions was not well predicted from experimental parameters was found, although the characteristic thickness of turbulent intrusions does depend on the parameters.

Values extrapolated for $\frac{N_{turb}^{target}}{N_{Ek}} = 100\%$, shown with red stars in fig. 6.7b, are used to estimate the turbulent viscosity ν_t. In fig. 6.8, the ratio ν_t/ν is presented as a function of the Rossby number $Ro = V_g/f\mathcal{L}$ (black stars, logarithmic scale). A linear regression (solid line) gives a slope of -0.6 in $\log_{10}(Ro)$. The plot fig. 6.8 indicates an apparent increase of the turbulent viscosity ν_t with rotation. This trend, however, contradicts theoretical expectations and previous studies, which show that rotation tends to suppress turbulence and thus reduce the effective viscosity (see Caldwell et al. 1972[10]; Taylor and Sarkar 2008[100]). However, if we account for an additional thin turbulent roughness sub-layer independent of f, then the thickening of the Ekman layer with increasing Ro reduces the relative impact of rugosity, producing the behaviour observed.

From the recorded velocity profiles, it is also possible to quantify how the rotating gravity current dynamically interacts with the bottom slope by estimating the friction velocity u_*. In Maggi et al. 2025[57], three definitions are proposed for evaluating u_*. Due to the limited vertical resolution of the ADVP, the vertical velocity gradient very close to the slope ($z \leq 1 \times 10^{-3}$ m) cannot be accurately resolved; consequently, the classical definition

$$u_*^2 = \nu\sqrt{(\partial_z u)^2|_{z=0} + (\partial_z v)^2|_{z=0}} \tag{6.11}$$

cannot be applied. Facing the same limitation, the definition

$$u_*^2 = \sqrt{\overline{\tilde{u}\tilde{w}}^2 + \overline{\tilde{v}\tilde{w}}^2}, \tag{6.12}$$

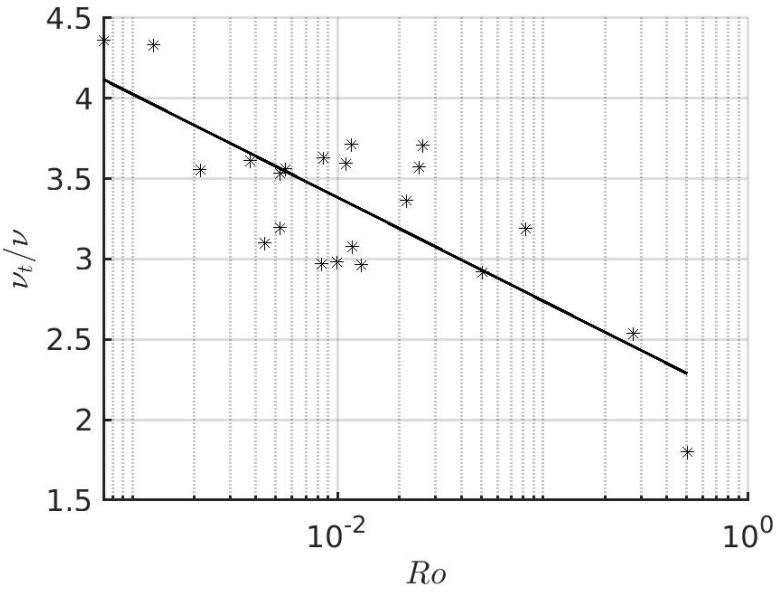

Figure 6.8: Turbulent viscosity computed for $\frac{N_{turb}}{N_{Ek}} = 100\%$ (see fig. 6.8), normalised by $\nu = 10^{-6}\,\mathrm{m^2\,s^{-1}}$, plotted against $\log_{10}(Ro)$. The linear regression is shown by the solid line.

based on the velocity fluctuations $\tilde{u} = u(z) - \langle\overline{u(z)}\rangle$, $\tilde{v} = v(z) - \langle\overline{v(z)}\rangle$, and $\tilde{w} = w(z) - \langle\overline{w(z)}\rangle$ (see Maggi et al. 2025[57] and Davarpanah et al. 2020[13]); and

$$u_*^2 = \frac{\langle\overline{\delta_{Ek}}\rangle f \langle\overline{v}\rangle}{\sqrt{2}}, \tag{6.13}$$

which relies on mean quantities and experimental parameters, where the azimuthal velocity $\langle\overline{v}\rangle$ is averaged over time and horizontal position, also following Maggi et al. 2025[57]. In Maggi et al. 2025[57] and Sous et al. 2013[95], the non-dimensional ratio $\langle\overline{v}\rangle/u_*$ is investigated. In Sous et al. 2013[95], experimental results led to the relation $\langle\overline{v}\rangle/u_* = \sqrt{2Ro_f}$, where the friction Rossby number is defined as

$$Ro_f = \frac{u_*^2}{f\nu}, \tag{6.14}$$

and the Reynolds number within the Ekman layer is expressed as

$$Re_\delta = \frac{\langle\overline{v}\rangle \delta_{Ek}^{lam}}{\nu} = \frac{\langle\overline{v}\rangle}{\sqrt{\nu f/2}}. \tag{6.15}$$

From expressions eq. 6.14 and eq. 6.15, we obtain

$$u_* = \sqrt{Ro_f f \nu}, \tag{6.16}$$

and

$$\langle\overline{v}\rangle = Re_\delta \sqrt{\nu f/2}. \tag{6.17}$$

Finally, dividing eq. 6.17 by eq. 6.16 yields

$$\frac{\langle \overline{v} \rangle}{u_*} = \frac{Re_\delta}{\sqrt{2Ro_f}}. \tag{6.18}$$

In fig. 6.9, $\frac{\langle \overline{V} \rangle}{u_*}$ is plotted against $\sqrt{Re_\delta}$ for all experimental cases and the three considered methods. For each distributions, black stars for Method 2, red stars for Method 1 and blue stars for Method 3, u^* has been obtained from eq. 6.13, where $\langle \overline{\delta_{Ek}} \rangle$ is estimated using the three methods presented in sub-section 6.3.2. For Method 2, the linear regression (solid black line) leads to the relation $\frac{\langle \overline{v} \rangle}{u_*} \approx \sqrt{Re_\delta}$. Consequently, eq. 6.18 gives $\frac{\langle \overline{v} \rangle}{u_*} = \sqrt{Re_\delta} = \sqrt{2Ro_f}$, which agrees with the laminar theory presented in Sous et al. 2013[95]. For Method 3, the linear regression yields a slope closer to the results of Maggi et al. 2025[57], where $\frac{\langle \overline{v} \rangle}{u_*} = 0.7\sqrt{Re_\delta}$. However, all methods produce approximately linear relationships, in good agreement with the laminar Ekman theory of Sous et al. 2013[95].

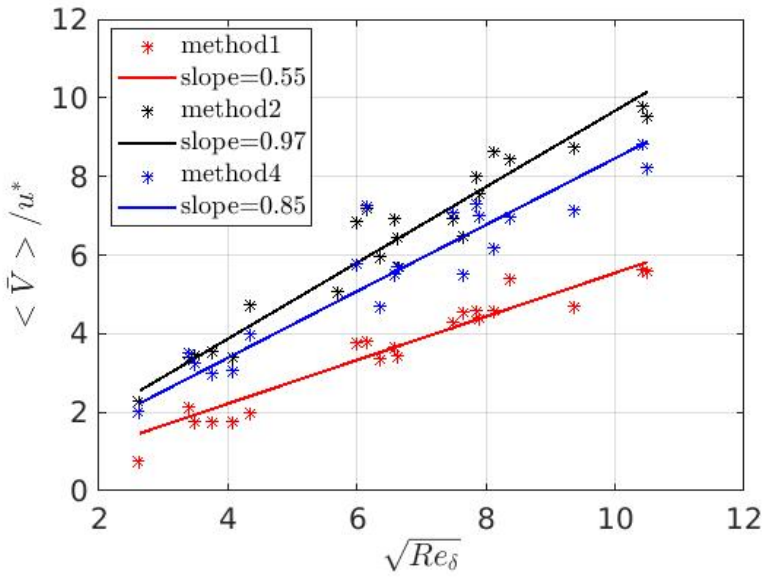

Figure 6.9: Scatter plot of the averaged maximum flow magnitude $\langle \overline{V_{max}} \rangle$ over the friction velocity u^*, compared with the square root of the Reynolds number based on the laminar Ekman layer, $\sqrt{Re_\delta}$. Method 1 (red stars); Method 2 (black stars); Method 3 (blue stars) (see sub-section 6.3.2). Linear regressions are shown by solid lines.

Results for all experiments are summarised in table 6.2. It is noted that u^*_{fluct}, computed from definition eq. 6.12, is of the same order of magnitude as u^* computed from definition eq. 6.13. However, u^*_{fluct} does not exhibit any clear trend, indicating that the Vectrino ADVP has limitations in accurately resolving velocity fluctuations.

6.4 Discussion and Conclusions

The study of the present chapter provides clear experimental evidence of Ekman dynamics in rotating downslope gravity currents, as the geostrophically adjusted main flow interacts with the underlying inclined topography. From a wide variety of experimental cases, summarised in table6.1, with Rossby numbers ranging from $Ro = 0.0013$ to $Ro = 0.5048$, we analysed the velocity structure near the slope (from $z' = 0\,\text{cm}$ to $z' = 3.2\,\text{cm}$). Ekman spiral shapes

Experiment	$\langle\overline{V_{max}}\rangle$ (cm/s)	u^* (cm/s)	u^*_{fluct} (cm/s)	Ro_f (−)
Case 2	1.23	0.171	0.213	14
Case 3	1.16	0.169	0.228	14
Case 5	0.30	0.090	0.111	6
Case 6	1.48	0.214	0.075	33
Case 7	1.65	0.218	0.071	34
Case 8	1.05	0.207	0.051	21
Case 9	1.43	0.251	0.050	30
Case 10	1.33	0.206	0.086	40
Case 11	0.46	0.128	0.118	8
Case 12	0.32	0.139	0.131	5
Case 13	0.61	0.130	0.148	8
Case 14	1.31	0.219	0.083	23
Case 15	2.88	0.294	0.134	62
Case 16	2.91	0.305	0.125	67
Case 17	2.84	0.325	0.131	50
Case 18	1.63	0.203	0.089	29
Case 19	1.14	0.134	0.088	34
Case 20	0.75	0.221	0.079	12
Case 21	0.39	0.113	0.129	6
Case 22	1.42	0.220	0.081	23
Case 23	1.40	0.202	0.087	20
Case 24	2.14	0.247	0.093	29

Table 6.2: Experimental results: averaged maximum flow magnitude $\langle\overline{V_{max}}\rangle$, friction velocity based on experimental parameters u^* (see eq. 6.13) and on velocity fluctuations u^*_{fluct} (see eq. 6.12), and the friction Rossby number Ro_f (see eq. 6.14).

were observed, but only a few snapshots of the velocity profiles could be fitted using Ekman theory, i.e. with eq. 6.1 and eq. 6.2, owing to strong upper stratification. For a Rossby number Ro ranging from 0.0056 to 0.0100, the maximum velocity magnitude determined from the spiral shapes gives $V_{max} \approx 0.8V_g$, which is consistent with expectations for rotating downslope gravity currents (see Rétif et al. 2024[84], Wirth 2012[114], Killworth 2001[45]). When rotation is very fast ($Ro = 0.0013$), the downslope current exhibits inertial oscillations and V_{max} exceeds V_g. However, when rotation is weak, the flow speed drops to $V_{max} \approx 0.25V_g$, as the dynamics are no longer associated with rotating gravity currents.

Three independent methods were developed to estimate the Ekman layer thickness δ_{Ek}. These methods respectively rely on: (i) the position of the local extrema of the azimuthal velocity profile $v(z)$; (ii) the decay of the velocity fluctuations (u', v') from their asymptotic values; and (iii) the differential system derived from the governing Ekman balance, which eliminates the need to estimate U_∞ and V_∞ explicitly. Despite their different formulations, all three methods provide thickness estimates of the same order of magnitude and reproduce consistent global trends with the rotation rate f. While Method 1 tends to overestimate δ_{Ek}, Method 2 yields sub-laminar values that are not consistent with theory. The third method yields values close to the laminar prediction $\delta^{lam}_{Ek} = \sqrt{2\nu/f}$. From the three methods, a turbulent viscosity ν_t was determined for each experiment and showed no significant variation with the associated Rossby number $Ro = V_g/f\mathcal{L}$. For Method 2, $\nu_t \approx 0.5\nu$; for Method 1, $\nu_t \approx 5\nu$; and for Method 3, $\nu_t \approx \nu$. Two different methodologies were used for applying

Method 2 and Method 1: the first determines δ_{Ek} from velocity profiles $\langle\overline{u(z)}\rangle$ and $\langle\overline{v(z)}\rangle$ averaged over all positions R_{scan} and time steps T_{scan} for all experimental cases, while the second computes δ_{Ek} from each individual velocity profile obtained in every experiment before calculating the mean thickness $\langle\overline{\delta_{Ek}}\rangle$. For Method 2, the thickness obtained from $\langle\overline{u(z)}\rangle$ and $\langle\overline{v(z)}\rangle$ is similar to $\langle\overline{\delta_{Ek}}\rangle$, whereas for Method 3 $\langle\overline{\delta_{Ek}}\rangle$ becomes lower and most values fall below the laminar prediction. Method 1 yields more scattered results when considering $\langle\overline{\delta_{Ek}}\rangle$. Method 3 applied to all profiles leads to values consistently below the laminar prediction, making it unsuitable for counting occurrences where $\delta_{Ek} > \delta_{Ek}^{lam}$. Thus, Method 2 was used to study the temporal evolution of the thickness throughout the experimental cases.

Applying Method 2 to all profiles, significant data dispersion was observed across experiments, likely due to variability in the rate of turbulent events N_{turb}/N_{ek}, which is not captured by theories based solely on f. However, when a constant turbulent rate N_{turb}/N_{ek} is assumed across all experiments, the data collapse onto the theoretical trend, aligning with the laminar Ekman thickness δ_{Ek}^{lam} when $N_{turb}/N_{ek} = 40\%$. When $N_{turb}/N_{ek} = 100\%$, the extrapolation allows the determination of a turbulent viscosity ν_t, which, surprisingly, decreases with Ro. This result is probably an artefact of the thickness determination method.

Finally, we confirm the linear Ekman theory presented in Sous et al. 2013[95], as linear regressions obtained from the three tested methods has led to linear relations between $\frac{\langle\overline{V_{max}}\rangle}{u^*}$ and $\sqrt{Re_\delta}$.

The dynamics of the bottom boundary layer play a crucial role in sediment transport. In particular, Maggi et al. 2025[57] identify the friction velocity u^* as a key parameter governing sediment resuspension and transport. Their experiments show that sediment transport is primarily driven by Ekman transport, resulting in a net cross-channel movement of sediments. Additionally, Ekman pumping enhances vertical sediment suspension, increasing the effective thickness of the suspended sediment layer. Observed patterns of erosion, deposition, and asymmetry in bedform development closely follow the predicted Ekman transport and shear stress distributions, strongly linking sediment dynamics to Ekman processes.

Bottom boundary mixing is also fundamental in shaping large-scale ocean circulation (see Munk and Wunsch 1998[65] and Marotzke 1997[58]). Marotzke 1997[58] conducted large-scale numerical simulations of the meridional overturning circulation (MOC), incorporating a simple parameterisation of the diapycnal diffusivity k_y near boundaries. These simulations demonstrated a strong dependence of both MOC strength $\Psi_{\max}$ (in Sverdrups, $1\,\mathrm{Sv} = 10^6\,\mathrm{m^3\,s^{-1}}$) and associated heat transport $Q_{\max}$ (in Petawatts, $1\,\mathrm{PW} = 10^{15}\,\mathrm{watts}$) on k_y, with scaling laws $\Psi_{\max} \propto k_y^{2/3}$ and $Q_{\max} \propto k_y^{1/2}$. These results highlight the critical influence of near-boundary dynamics on large-scale circulation. Notably, the study concludes that lateral boundary mixing alone can sustain a realistic MOC in the absence of interior mixing. Our findings, demonstrating the recurrent occurrence of a turbulent Ekman bottom layer, fit within this paradigm, as such dynamics leave a marked imprint on the ocean's interior structure (see Rétif et al. 2024[84]).

Our results are potentially important for representing bottom dynamics in realistic numerical simulations of ocean circulation, as they show that finer vertical resolution is required than that estimated from laminar Ekman theory. The representation of bottom dynamics is key to accurately capturing the bottom shear, unlike at the surface where the shear is largely imposed by atmospheric forcing.

Chapter 7

General conclusion and perspectives

7.1 Conclusions

This thesis aims to advance our understanding of the dynamics of rotating downslope gravity currents that play a crucial role in the ventilation of the deep ocean and in the redistribution of tracers such as heat, salt, nutrients, mass, and momentum. Such dense overflows, although localised, contribute significantly to the global thermohaline circulation and thus to the climate system. Yet, their small spatial scales and the complexity of their interactions with rotation, stratification, and turbulence make them difficult to represent accurately in numerical ocean models. The central objective of this work was therefore to investigate, through controlled large scale laboratory experiments at the Coriolis platform (LEGI, Grenoble), the physical mechanisms governing the structure, evolution, and internal dynamics of rotating gravity currents, particularly the mechanisms of intrusion into a stratified ambient and the formation of the near-bottom Ekman friction layer.

Summary of the main developments. Chapter 2 recalled the theoretical foundations necessary for the analysis of rotating stratified flows, including the Brunt–Väisälä frequency, the governing equations in a rotating frame, and the fundamental balances that characterise geophysical flows, geostrophic, hydrostatic, and Ekman dynamics, highlighting the main assumptions made in ocean dynamics. The chapter also presented the Sverdrup relation linking wind stress and large-scale gyre circulation, briefly introduced the global thermohaline circulation, and reviewed classical observational and experimental techniques. This theoretical groundwork provided the basis for interpreting both the literature review and experimental results.

Chapter 3 reviewed the major observational, theoretical, numerical, and experimental studies relevant to rotating downslope gravity currents. Observational campaigns such as the Mediterranean Overflow, Denmark Strait Overflow, and Weddell Sea overflows were discussed, highlighting how dense over-flows develop on continental slopes under the combined action of buoyancy, rotation, and friction. The chapter also revisited key theoretical developments, from early analytical models (Bowden 1960[6], Smith 1975[92], Killworth 1977[44]) to more sophisticated entrainment parameterisations (Price and Baringer 1994[77], Shapiro and Hill 1997[89]) and the inclusion of the underlying Ekman friction layer (Wåhlin and Walin 2001[110], Wirth 2009[113], Ungarish 2022[106]).

Chapter 4 described the experimental campaign *TUBE (Turbulent Life of Downslope Intruding Gravity Current)* performed on the 13-metre diameter Coriolis rotating platform. The axisymmetric conical slope geometry, two-layer density stratification, and distributed injection system were detailed, along with the three primary measurement techniques: (i) a

conductivity probe for vertical density profiles, (ii) an Acoustic Doppler Velocimetry Profiler (ADVP) for near-slope velocity measurements, and (iii) Particle Image Velocimetry (PIV) for horizontal velocity fields. Calibration procedures, acquisition parameters, and post-processing methods were also presented.

Chapter 5 analysed the vertical density profiles obtained within the central deep area of the tank. Two distinct intrusion regimes were identified: laminar and turbulent. A criterion based on the Peclet number was established to discriminate between them, and an analytical model was developed to predict the thickness of turbulent intrusions thickness. The model successfully reproduced the experimental observations over a range of Rossby numbers, demonstrating that the layer thickness is governed by a balance between buoyancy, inertia, and diffusive effects. This analysis established a quantitative link between the density structure, flow regime, and turbulent mixing intensity, providing the basis for understanding the structural imprint left in deep waters by the intrusion of oceanic gravity currents.

Chapter 6 focused on the characterisation of the near-bottom Ekman layer using ADVP velocity profiles. Three independent methods were proposed to estimate the Ekman-layer thickness: (i) a method based on velocity fluctuations and their asymptotic decay, (ii) a method based on the local velocity maxima and asymptotic values, and (iii) a differential method using the third vertical derivative of the velocity profile, for which estimating far-field asymptotic velocities is no longer required. The results were compared to classical laminar predictions, $\delta_{Ek}^{lam} = \sqrt{2\nu/f}$, and yielded consistent magnitudes and trends with rotation rate. The friction velocity derived from the measured thickness exhibited a linear relation with the Reynolds number based on the laminar Ekman scale, in agreement with the scaling proposed by Sous et al. 2013[95]. These findings demonstrated that the laminar Ekman theory can describe the mean structure of the flow even in the presence of intermittent turbulence.

7.2 Perspectives

Inspired by the work of Decamp 2005[17], an ongoing investigation focuses on the time evolution of the vertical density profiles measured in the central deep area, with the aim of characterising the mixing induced by rotating downslope gravity currents. The approach consists in analysing the density profiles recorded after the injection has stopped. A dedicated set of experiments performed in 2021 includes near-slope density measurements at a fixed elevation: the CTD was mounted on the ADVP and recorded density over 21 horizontal positions along the slope. Combined with the Ekman-layer thickness estimates obtained in Chapter 6, the analysis of this extended density dataset is expected to provide new insights into the structure and variability of Ekman dynamics beneath rotating gravity currents.

Several directions for future research naturally arise from this work. First, the results obtained here could be extended by increasing both the temporal and spatial resolution of measurements, particularly the vertical resolution of the ADVP, in order to capture finer-scale features of the Ekman dynamics and improve the detection of transient turbulent bursts. Second, additional experiments varying the slope angle or including a wider range of rotation rates would help to quantify their influence on the boundary-layer structure and on the transition between laminar and turbulent regimes. One of the main limitations of the present experiments lies in their transient behaviour. Designing a configuration that achieves a steady-state downslope current would be challenging but highly valuable, as it would allow for longer observation times and improve the statistical reliability of the measurements. Finally, the analytical model developed in Chapter 5 for the turbulent intrusion thickness should be further tested against *in situ* oceanographic observations, to assess its applicability

beyond the laboratory and to refine parameterisations of dense overflows in large-scale ocean models. The question of how my results persist in ocean gravity currents on rough boundaries and with topographic features is widely open.

Chapter 8

Appendix

8.1 A) Numerical error from Method 3.

When the Method 3 is used to determine δ_{Ek}, the discretised version of eq. 6.7 involves numerical schemes for first and third z derivatives. Let consider $h = \Delta z$ $u_n = u(z + nh)$ so eq. 6.9 and eq. 6.8 becomes:

$$\widehat{u_z} = \frac{u_1 - u}{h}, \tag{8.1}$$

and

$$\widehat{u_{zzz}} = \frac{-u + 3u_1 - 3u_2 + u_3}{h^3}, \tag{8.2}$$

both with an error of order $O(h^2)$. To quantify this error, we define the truncation error for both schemes using Taylor expansions. For $\widehat{u_z}$ we get:

$$u_1 = u + hu_z + \frac{h^2}{2}u_{zz} + O(h^3) \Rightarrow \widehat{u_z} = u_z + \frac{h}{2}u_{zz} + O(h^2). \tag{8.3}$$

For the third derivative we need to expand further:

$$u_0 = u, \tag{8.4}$$

$$u_1 = u + hu_z + \frac{h^2}{2}u_{zz} + \frac{h^3}{6}u_{zzz} + \frac{h^4}{24}u_{zzzz} + O(h^5), \tag{8.5}$$

$$u_2 = u + 2hu_z + 2h^2u_{zz} + \frac{4h^3}{3}u_{zzz} + \frac{2h^4}{3}u_{zzzz} + O(h^5), \tag{8.6}$$

$$u_3 = u + 3hu_z + \frac{9h^2}{2}u_{zz} + \frac{9h^3}{2}u_{zzz} + \frac{27h^4}{3}u_{zzzz} + O(h^5). \tag{8.7}$$

and equation eq. 8.2 reduces to

$$\widehat{u_{zzz}} = u_{zzz} + \frac{3h}{2}u_{zzzz} + O(h^2). \tag{8.8}$$

Setting $A = u_z^2 + v_z^2$, $B = u_{zzz}^2 + v_{zzz}^2$, we define

$$\widehat{A} = \widehat{u_z}^2 + \widehat{v_z}^2 = A + h(u_z u_{zz} + v_z v_{zz}), \tag{8.9}$$

and

$$\widehat{B} = \widehat{u_{zzz}}^2 + \widehat{v_{zzz}}^2 = B + 3h(u_{zzz}u_{zzzz} + v_{zzz}v_{zzzz}). \tag{8.10}$$

Now if we consider $R = \frac{A}{B}$ and $\widehat{R} = \frac{\widehat{A}}{\widehat{B}}$; thus the approached Ekman layer thickness is $\widehat{\delta_{Ek}} = \sqrt{2}\widehat{R}^{1/4}$ and the true value is $\delta_{ek} = \sqrt{2}R^{1/4}$. We need to determine the relative error $\frac{\widehat{\delta_{Ek}} - \delta_{Ek}}{\delta_{Ek}}$. First let compute the ratio $\frac{\widehat{R}}{R} = \frac{\widehat{A}}{A}\frac{B}{\widehat{B}}$. As

$$\frac{\widehat{A}}{A} = 1 + \frac{h}{A}(u_z u_{zz} + v_z v_{zz}), \tag{8.11}$$

and

$$\frac{B}{\widehat{B}} = \frac{1}{1 + 3\frac{h}{B}(u_{zzz}u_{zzzz} + v_{zzz}v_{zzzz})} \approx 1 - 3\frac{h}{B}(u_{zzz}u_{zzzz} + v_{zzz}v_{zzzz}) + O(h^2), \tag{8.12}$$

from a first-order Taylor expansion, we find that

$$\begin{aligned} \frac{\widehat{R}}{R} &= (1 + \frac{h}{A}(u_z u_{zz} + v_z v_{zz}))(1 - 3\frac{h}{B}(u_{zzz}u_{zzzz} + v_{zzz}v_{zzzz})) + O(h^2) \\ &= 1 + h(\frac{u_z u_{zz} + v_z v_{zz}}{A} - 3\frac{u_{zzz}u_{zzzz} + v_{zzz}v_{zzzz}}{B}) + O(h^2). \end{aligned} \tag{8.13}$$

We define the relative error $\epsilon = \frac{\widehat{R}-R}{R} \Rightarrow \widehat{R} = R(1+\epsilon)$. As $\widehat{\delta_{Ek}} = \sqrt{2}\widehat{R}^{1/4}$, we identify that

$$\widehat{\delta_{Ek}} = \delta_{Ek}(1+\epsilon)^{1/4} \Rightarrow \frac{\widehat{\delta_{Ek}}}{\delta_{Ek}} = (1+\epsilon)^{1/4} \approx 1 + \frac{\epsilon}{4} + O(h^2), \tag{8.14}$$

from a first-order Taylor expansion. Thus

$$\frac{\widehat{\delta_{Ek}} - \delta_{Ek}}{\delta_{Ek}} = \frac{\epsilon}{4} = \frac{h}{4}(\frac{u_z u_{zz} + v_z v_{zz}}{A} - 3\frac{u_{zzz}u_{zzzz} + v_{zzz}v_{zzzz}}{B}). \tag{8.15}$$

The z-derivatives obtained from eq. 6.1 and eq. 6.2 are:

$$\begin{aligned} u_z &= \frac{U_\infty - V_\infty}{\delta_{Ek}}, & v_z &= \frac{U_\infty + V_\infty}{\delta_{Ek}}, \\ u_{zz} &= \frac{2}{\delta_{Ek}^2}V_\infty, & v_{zz} &= -\frac{2}{\delta_{Ek}^2}U_\infty, \\ u_{zzz} &= -\frac{2}{\delta_{Ek}^3}(U_\infty + V_\infty), & v_{zzz} &= \frac{2}{\delta_{Ek}^3}(U_\infty - V_\infty), \\ u_{zzzz} &= \frac{4}{\delta_{Ek}^4}U_\infty, & v_{zzzz} &= \frac{4}{\delta_{Ek}^4}V_\infty. \end{aligned} \tag{8.16}$$

Injecting in eq. 8.15 leads to

$$\begin{aligned} \frac{\widehat{\delta_{Ek}} - \delta_{Ek}}{\delta_{Ek}} = \frac{h}{4}\Bigg[& 2\frac{(U_\infty - V_\infty)V_\infty - (U_\infty + V_\infty)U_\infty}{\delta_{Ek}^3}\frac{\delta_{Ek}^2}{(U_\infty - V_\infty)^2 + (U_\infty + V_\infty)^2} \\ & - 3\frac{-8(U_\infty + V_\infty)U_\infty + 8(U_\infty - V_\infty)V_\infty}{\delta_{Ek}^7}\frac{\delta_{Ek}^6}{4(U_\infty + V_\infty)^2 + 4(U_\infty - V_\infty)^2}\Bigg] + O(h^2). \end{aligned} \tag{8.17}$$

After rearranging, it reduces to

$$\frac{\widehat{\delta_{Ek}} - \delta_{Ek}}{\delta_{Ek}} = \frac{h}{2\delta_{Ek}} + O(h^2). \tag{8.18}$$

8.2 B) Predicting the vertical density structure of oceanic gravity current intrusions

scientific reports

Check for updates

OPEN

Predicting the vertical density structure of oceanic gravity current intrusions

Sévan Rétif✉, Maria Eletta Negretti & Achim Wirth

Understanding the dynamics and structures in the deep ocean is one of the remaining challenges in oceanography and climate sciences. We present results from large-scale laboratory experiments of rotating down-slope gravity currents intruding into a two-layer stratified ambient, performed in the largest rotating tank in the world, the Coriolis Rotating Platform in Grenoble. By means of velocity and density measurements, we show that no mixing occurs once the current has detached from the boundary. The shape of the vertical density profile in the stratified receiving ambient enables to identify two distinct regimes: the first issued by laminar transport through Ekman dynamics, the second by turbulent transport due to intermittent dense water cascading. Vertical density gradients reveal a piece-wise linear dependence on the density anomaly for the turbulent transport, suggesting an advection-diffusion process. For the turbulent regime, the scale height is deduced and an analytical model based on the critical Froude number is proposed to predict its value. Results show that the total thickness of the intruding current is on average 2.5 times the scale height. For laminar intrusions the scale height diverges whereas the thickness of the intrusion is a few times the Ekman layer thickness. Comparing the intrusion scale height with its measured vertical extension has led to a criteria to distinguish between laminar and turbulent regimes, which is corroborated by two additional independent criteria, one based on the sign of the local vorticity and the other based on the local maxima of the vertical density gradient. The model allows us to connect laboratory experiments to deep sea observations, gravity currents and Meddies and emphasizes the importance of laboratory experiments in understanding climate dynamics.

Ocean circulation is one of the most affecting dynamics for the Earth's climate system, because of the huge amount of heat and CO_2 stored in, and transported by, the ocean and also exchanged with the atmosphere and the cryosphere, see i.e. the sixth IPCC report[1]. The global circulation is driven by wind forcing at the surface and influenced by buoyancy and the Coriolis force. While near surface ocean circulation is well observed, understood and modeled, deep ocean dynamics is remote and enigmatic[2,3]. Ocean gravity currents are known to transport salty and cold water from a coastal environment towards the deeper ocean. They are up to 20 km large and 200 m thick[4] and have been observed in many places around the world. An example is the strait of Gibraltar, where saltier water from the Mediterranean reaches the Atlantic ocean water of lower salinity, creating the Mediterranean outflow[5]. Other examples are: The Bab el Mandeb strait at the exit of the Red Sea[6], the strait of Hormouz at the exit of the Persian Gulf[7] and the Denmark strait overflow[8]. The same mechanism has been observed where the density anomaly is ensured by temperature differences, for example at the Filcimer Ice Shelf outflow into the Weddell Sea[9]. In their pioneering work, Cooper and Vaux[10] showed that cooling by surface radiation and evaporation during winter is responsible for a heavy water mass descending down a continental slope to a depth of several hundred meters. This phenomena was observed in the Celtic Sea and in the English Channel and expected to be seen widely, especially in winter at shallow banks. These currents have an impact on the concentration of nutrients and iron in the Celtic Sea. The importance of geostrophic balance in the case of down-slope gravity currents is raised in Gill[11], discussing a larger scale gravity current in the Weddell Sea.

A well established scheme is proposed by Shapiro and Hill[12], where the gravity current is geostrophically adjusted along-slope within a day, while due to friction, part of this dense water mass is transported downslope. Two mechanisms are pointed out for describing this downslope transport: a near slope Ekman balance between friction, Coriolis force and buoyancy, and an Ekman drainage due to upper-layer friction. Stream-tubes models are derived[13], in which it is assumed that physical properties vary in the stream-wise direction of the gravity

CNRS, Grenoble INP, LEGI, Univ. Grenoble Alpes, 38000 Grenoble, France. ✉email: sevan.retif@univ-grenoble-alpes.fr

current, while cross-stream variations are integrated over the cross section of the gravity current. The downstream position, thickness and density anomaly of the stream tube is calculated based on physical laws and parametrisations of the unresolved processes. These models are able to include parameterised turbulent fluxes such as entrainment, mixing, detrainment, and turbulent friction. Wirth[4], Wåhlin and Walin[14] as well as Ungarish[15] suggested instead to consider the rotating gravity current as composed by two interacting parts: the main flow, the "vein", geostrophically adjusted moving along slope at the geostrophic velocity[16], and a friction layer in which the geostrophic balance is perturbed by friction, non linearity and turbulent fluxes. Therefore, part of the water mass escapes the vein and feeds a friction layer. All these approaches are based on a continuous down-slope evolution of the gravity current, a property which is here challenged based on laboratory experiments.

Several studies have been carried out in order to characterise the mixing involved in geophysical flows, see the review of Legg et al.[17], but it still remains a challenging task. Considering the vertical stratification of the ocean interior Munk and Wunsch[18,19] assumed a balance between vertical advection and diffusion, obtaining a vertical turbulent diffusivity of $\kappa_z \approx 10^{-4}$ m^2 s^{-1}. In the work of Kunze and Smith[20], from ocean observations in three different regions (on topography, interior, surface), the diffusivity is measured and compared with a value of 10^{-4} m^2 s^{-1}, obtained from the steady vertical advective–diffusive balance of Munk[18]. These comparisons have shown that mixing does not occur in the interior but rather at the bottom slope, and that the topography variation can boost for the diapycnal eddy diffusivity. Van Haren and Gostiaux[21] derived turbulent vertical eddy diffusivities, κ_z, and dissipation rates, ϵ, above the Great Meteor Seamount in the Canary Basin. They found that tidal flows are the dominant factor influencing temperature variations in the area, but the local bottom slope played a crucial role in semi-diurnal frequency motions. When averaging over a fortnight (2-weeks period), the estimated overall mean values were found as: $\kappa_z = 3 \pm 10^{-3}$ m^2 s^{-1} and $\epsilon = 1.5 \pm 0.7 \times 10^{-7}$ W kg^{-1}. The role of boundary mixing with respect to interior mixing for the ocean remains largely debated[20]. Negretti et al.[22] measured the gravity current structure on the slope area confirming the dual components, the vein and the friction layer, and characterized the induced cyclonic vortices generated in the upper layer, as already observed by previous authors (e.g. Lane-Serff and Baines[23]). Wirth and Negretti[24] and Negretti et al.[22] explained the induced basin scale circulation of a down-slope gravity current and its intrusion into a two-layer configuration, using potential vorticity conservation. In the present paper we focus on the temporal evolution of the density structure issued by intruding oceanic gravity currents which, to the best of our knowledge, has not been considered before. This is astonishing as most gravity currents in the ocean intrude into the ambient when reaching their neutral buoyancy level.

We present results from the high quality and fine scale dataset collected during the experimental campaign TUBE[22]. In the experiment, dense saline water is injected on an inclined plane in the Coriolis rotating platform. Due to the Coriolis force ($f > 0$), the down-slope current is deviated to the right approaching geostrophy. Bottom friction and auto-advection of momentum (non-linearity) lead to down-slope motion. When the neutral buoyancy is reached, at the halocline, the down-slope motion stops and the Coriolis force channels the injected water into a deep boundary current (hereafter DBC) along the slope. Part of the injected water propagates offshore. This intrusion leaves an imprint in the density and vorticity structure in the ocean interior. Studying the features of this sequence, from injection to intrusion, is important to further our understanding of the thermohaline structure, circulation, oxygenation and CO_2 sequestration in the world's oceans. We identify two regimes for the intrusion based on the shape of the vertical density profiles and vorticity contours, then we determine the scale height[25] using an advection–diffusion model[18]; a new model based on the critical Froude number is proposed to predict the averaged value of the scale height as a function of the experimental parameters; we end by showing that no mixing takes place in the interior but rather on the slope during the descent.

Methods

The experiments have been conducted in the Coriolis Rotating Platform, the largest rotating tank in the world (13 m wide). For the experiments, the tank has a rotation period T and was filled with a two-layer stratification: a layer of fresh water at a density ρ_t, and a thickness h_t, above a second layer of salty water at a density ρ_b, and thickness h_b. During an experiment, at a fixed Coriolis parameter f, water with a density ρ_j, such that $\rho_t < \rho_j < \rho_b$, was injected at a constant flow rate Q_j, through 32 injectors circularly placed around the tank's circumference just above a sloping boundary ($s = \tan\theta = 0.1$) and directed at 45° towards the right to accelerate geostrophic adjustment (see Fig. 1a). A vertically moving conductivity probe was used for recording vertical density profiles, every 60 s, in the central deep area (at a distance of 105 cm from the center) throughout the experiment duration (up to 220 rotational days). particle image velocimetry (PIV) is performed on 16 horizontal levels in order to record horizontal velocity data. The volume is scanned every 85 s (as seen in Fig. 1b). More details are given in the work of Negretti et al.[22].

The relevant parameters are the slope $s = \tan\theta = 0.1$ the Coriolis parameter f, the difference between the injected density and the density of the top layer in the receiving ambient expressed in terms of the buoyant acceleration $g' = g\frac{\rho_j - \rho_t}{\rho_t}$, where g is gravity, and the kinematic viscosity ν. The characteristic velocity scale is the geostrophic velocity $V_g = g's/f$ and the characteristic vertical scale is given by a overall intrusion thickness $H = \gamma h_b$, where $\gamma = (\rho_j - \rho_t)/(\rho_b - \rho_t)$ measuring the portion of intruding water in the bottom layer. The characteristic horizontal scale $\mathscr{L}$ required for the Ekman transport $T_{Ek} = V_g\delta_{Ek}/2$, ($\delta_{Ek} = \sqrt{2\nu/f}$ is the thickness of the Ekman layer) to transport the total injected flux Q_j downward, is given by the relation $\mathscr{L} = Q_j/T_{Ek}$.

The relevant non-dimensional numbers, defined with the external parameters known prior to the experiment, are: the Froude numbers in the vertical $F_v = V_g/(g'H) = \mathcal{O}(10^{-1})$ and in the horizontal $F_h = V_g/(g'\mathscr{L}) = \mathcal{O}(10^{-2})$, the Rossby number $Ro = V_g/(f\mathscr{L})$, the Reynolds number $Re = V_g\mathscr{L}/\nu = \mathcal{O}(10^5)$ and the buoyancy Reynolds number $Re_b = ReF_h^2 = \mathcal{O}(10^4)$. The experimental parameters g', f, Q_j, T_{Ek}, H and

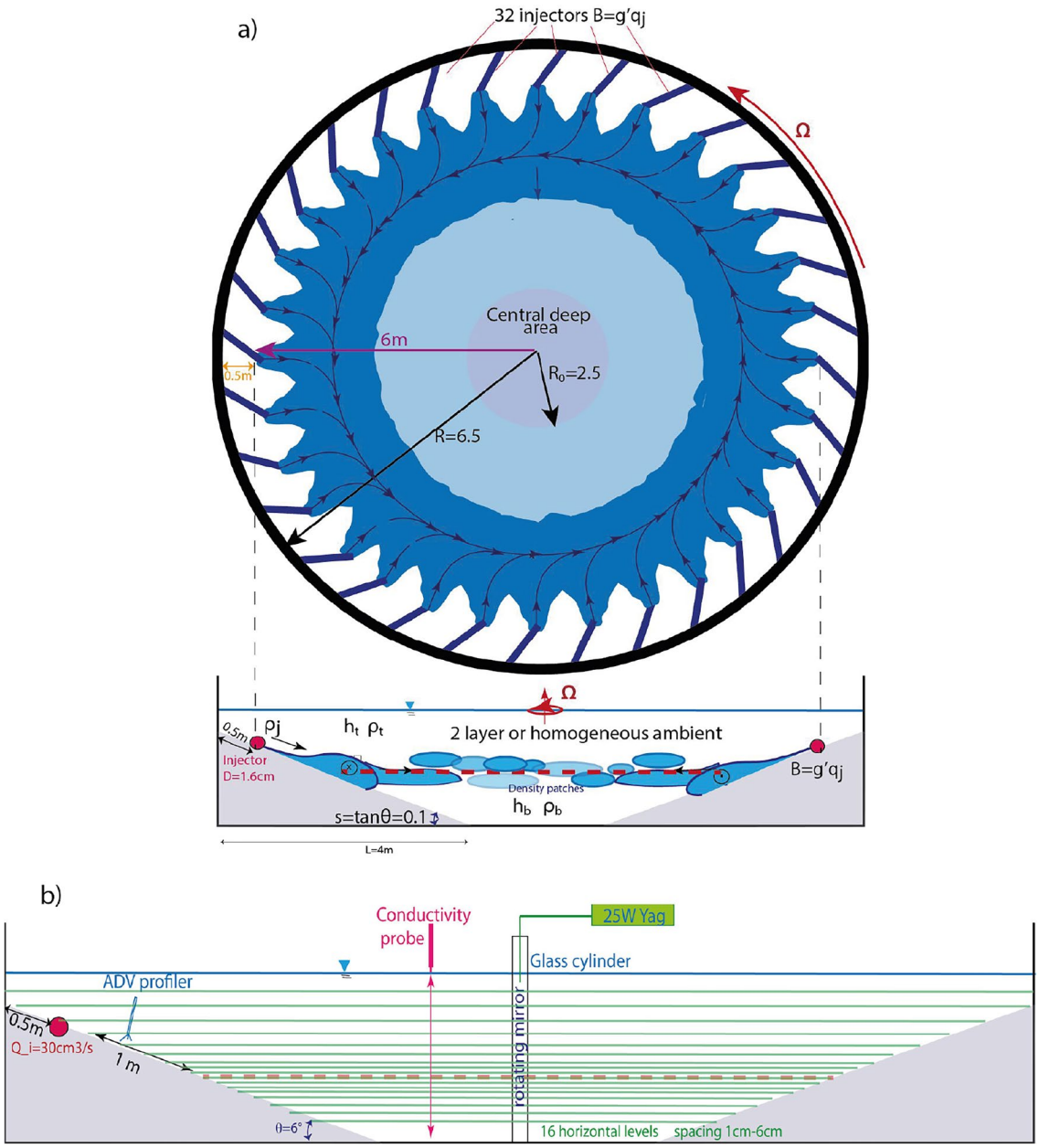

Figure 1. Sketch of the experimental set-up[22]. (**a**) Schematic top and side views of the experimental design. $N = 32$ pipes positioned 0.5 m from the tank edge and inclined by 45° inject continuously saline solutions at a density of ρ_j and with a constant flow rate ranging as $q_j = 32$–43 cm^{3}s^{-1} into a homogeneous or stably two-layer stratified ambient. The axisymmetric conical slope has an inclination of $\theta = 6°$ ($s = \tan\theta = 0.1$) and a total length of 4 m. The central deep area has a diameter of 5 m. (**b**) Enlarged side view sketch showing the 16 horizontal slices for the PIV measurements, along with the ADV position and the conductivity probe mounted on a 1 m scanning axe.

the values of the relevant non-dimensional numbers Ro, F_v and F_h for the different experiments considered are presented in Table 1. In the following sections, most of the results are presented for Case 1, but results from all other experiments presented in Table 1 are similar.

Results

Laminar versus turbulent intrusion

The temporal evolution of the vertical density profile allows to observe the intrusion of salty water into the initially two-layer stratified ambient at one horizontal location (cf. Fig. 1b) and to monitor its development. Figure 2a and c present the vertical density profiles (red lines) as well as the vertical density gradients (black stars) as a function of the density anomaly at different times ($t/T = 84$, $t/T = 140$, respectively) for Case 1. At $t/T = 84$ (Fig. 2a) a zone with a linear variation of the density with depth (red curve) can be distinguished, visible as a plateau between 1 kg^3 m^{-1} and 5 kg^3 m^{-1} for the vertical density gradient (black stars). At $t/T = 140$ (Fig. 2c),

Experiment	g' (cm/s^2)	f (s^{-1})	Q_j (l/s)	T_{Ek} (m^2/s)	H (cm)	Ro (–)	F_v (–)	F_h (–)
Case 1	5.1	0.14	1.39	6.95×10^{-5}	0.058	1.3×10^{-2}	0.67	0.04
Case 2	5.79	0.21	0.69	4.29×10^{-5}	0.063	8.2×10^{-3}	0.46	0.02
Case 3	6.09	0.21	1.19	4.51×10^{-5}	0.042	5.2×10^{-3}	0.57	0.02
Case 4	5.5	0.21	1.15	4.07×10^{-5}	0.063	4.4×10^{-3}	0.44	0.02
Case 5	5.1	0.1	1.35	1.07×10^{-4}	0.056	3.7×10^{-2}	0.91	0.06
Case 6	4.81	0.14	1.37	6.54×10^{-5}	0.073	1.2×10^{-2}	0.58	0.03
Case 7	5.5	0.21	1.36	4.07×10^{-5}	0.052	3.7×10^{-3}	0.49	0.02
Case 8	9.63	0.21	0.6	7.13×10^{-5}	0.11	2.6×10^{-2}	0.45	0.05
Case 9	7.17	0.42	0.6	1.83×10^{-5}	0.1	1.2×10^{-3}	0.20	0.01
Case 10	5.5	0.21	1.35	4.07×10^{-5}	0.082	8.5×10^{-3}	0.39	0.03
Case 11	4.51	0.21	1.11	3.34×10^{-5}	0.073	2.2×10^{-3}	0.37	0.01
Case 12	6	0.14	1.36	8.17×10^{-5}	0.083	1.0×10^{-2}	0.61	0.03
Case 13	9.16	0.21	2.54	6.78×10^{-5}	0.106	5.6×10^{-3}	0.44	0.02
Case 14	6.97	0.42	1	1.88×10^{-5}	0.105	7.5×10^{-4}	0.19	0.01
Case 15	5.3	0.05	1.2	3.14×10^{-4}	0.076	5.1×10^{-1}	1.60	0.23

Table 1. Experimental parameters and non-dimensional numbers. The buoyant acceleration is defined as $g' = g\frac{\rho_j - \rho_t}{\rho_t}$, with g being the gravitational acceleration, the Coriolis parameter is $f = 4\pi/T$, where T is the tank's rotating period, the injection rate Q_j, the Ekman transport is given by $T_{Ek} = (g's/f)\delta_{Ek}/2$, where δ_{Ek} is the thickness of the Ekman layer, the Rossby number $Ro = V_g/(f\mathscr{L})$, vertical and horizontal Froude numbers $F_v = V_g/(g'H)$ and $F_h = V_g/(g'\mathscr{L})$.

a curved shape is localised above the halocline and at density anomalies smaller than about $\Delta\rho \approx 5$ kg^3 m^{-1}, leading to a double saw-tooth structure for the vertical density gradient. The corresponding vorticity field at the halocline is presented in Fig. 2b and d. At the location of the conductivity probe (Green dot in Fig. 2b,c) a positive vorticity is present at $t/T = 84$ in Fig. 2b, while a negative vorticity is registered for $t/T = 140$ in Fig. 2d.

Two mechanisms of intrusion are so identified: in the first, the dense water flows down the slope through laminar Ekman transport which feeds the DBC forming at the halocline. The second mechanism of intrusion, taking the form of dense water cascading, pushes the original DBC toward the central deep area, making it meander, as visible in Fig. 2b characterized by high positive vorticity values. This second mechanism of intrusion performs inertial overshoots characterised by negative relative vorticity and is visible in Fig. 2b where strong negative vorticity zones (dark blue) are located where the DBC is meandering. The horizontal dynamics and its spatio-temporal structure will be published in Tassigny et al.[26].

At $t/T = 140$ (Fig. 2d), the turbulent intrusions have broken the original DBC confining the positive vorticity to a few cyclones and are captured by the conductivity probe, which is now located in a zone where ζ is negative.

The Hovmöller diagram for Case 1 is given in Fig. 3. Laminar intrusions characterised by local linearly varying vertical density profiles lead to a uniform and slow thickening of the halocline. They are highlighted by the vertical green lines in Fig. 3. Intrusions from dense water cascading, characterised by an exponential shape of the vertical density profile, on the other hand, lead to an abrupt vertical expansion of the halocline thickness, a close to homogeneous core and are highlighted by vertical red lines in Fig. 3. We observe that after periods of purely laminar intrusions, periods of purely turbulent intrusions can follow as in experiment Case 1 (Fig. 3), or turbulent intrusions can happen intermittently as observed on other experiments. No apparent correlation between the varied experimental parameters and this behavior has been found. Vorticity contours have shown that this intermittent behavior is due to the meandering shape of the DBC.

To quantitatively discriminate between the two regimes of intrusions, laminar versus turbulent, we considered three independent criteria. The first consists in detecting a pronounced local maxima in the vertical density gradient distribution at the injected density anomaly ρ_j as shown in Fig. 2c (black stars). This local maxima criteria detects a sharp density gradient, which is translated in an accumulation of low vertical density gradient values as highlighted in Fig. 2c by the red box. The sign of the vorticity ζ measured at the probe location can also be used as a criteria. A last criteria, our principal, is based on the exponential variation of density with depth as given in Fig. 2a and c. Munk and Wunsch[18,19] state that the vertical structure of the deep ocean is a consequence of a balance between upward advection w and downward diffusion κ. This approach has also been applied to smaller scale, time-dependent motion in the Adriatic[3]. It was furthermore observed through potential vorticity conservation[24] that there is an overall upward velocity above the slope. In a stationary state the equation governing the vertical density distribution is:

$$\partial_z(w\rho) - \partial_z(\kappa\partial_z\rho) = 0. \tag{1}$$

With a constant vertical velocity and diffusivity, this equation shows a linear relation between the density and its vertical gradient and has exponential solutions, with κ/w as the e-folding length scale.

Figure 4a and b represents the profiles as given in Fig. 2a and c, fitted with four exponential functions whose boundaries are determined by the local extremes of the vertical density gradient: the transition from the upper layer to the intrusion (magenta), the intrusion (red), the transition to the bottom layer (blue) and the bottom layer (green). Solutions of Eq. (1) are calculated by imposing a starting vertical position z_1 and the corresponding

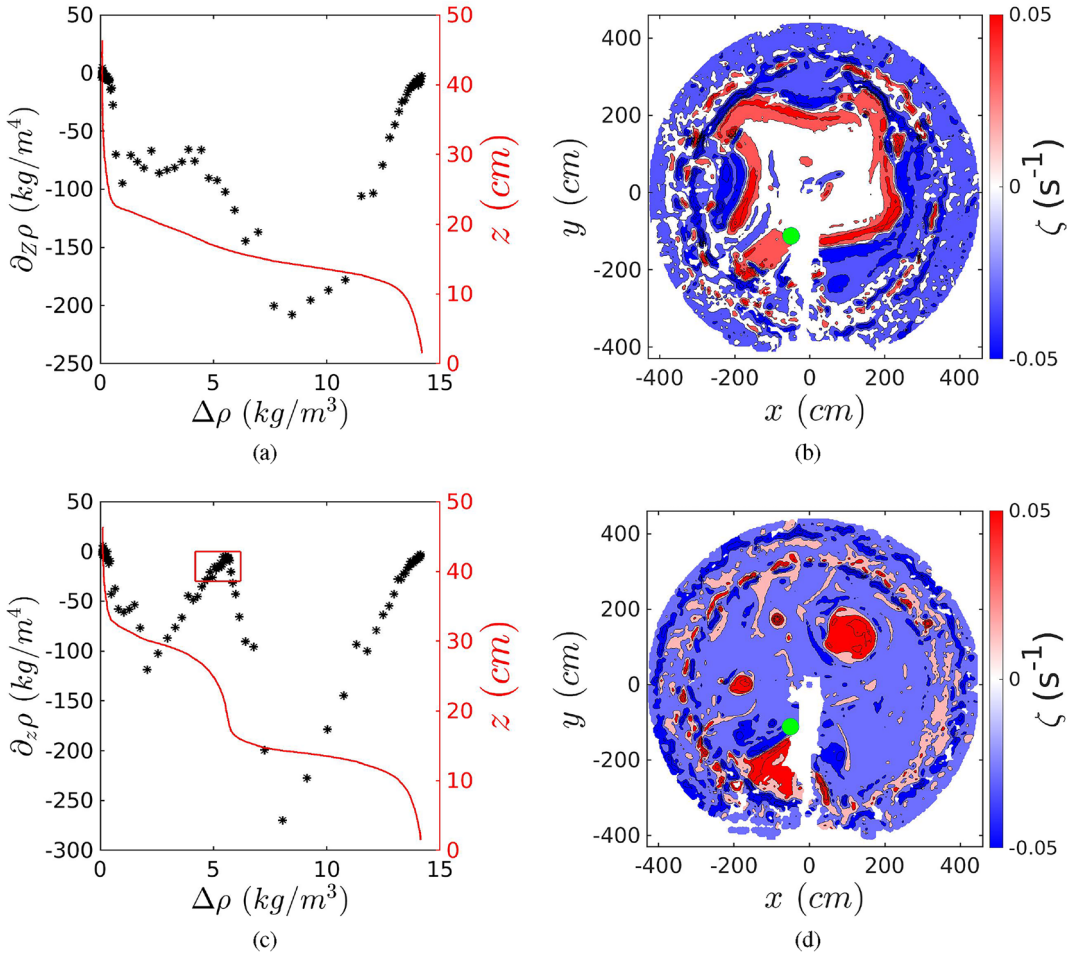

Figure 2. Vertical density profiles (red line), and the corresponding vertical density gradient (black stars) for $t/T = 84$ (**a**) and $t/T = 140$ (**c**), for Case 1. The red box in (**c**) highlights an accumulation of low values of the vertical density gradient for the local maxima criteria and it is bounded as $\rho = \rho_i \pm 1$ and $-30 \leq \partial_z\rho \leq 0$ (**b**, **d**). In (**b**) and (**d**), horizontal vorticity fields is computed from PIV measurements at $z = 15$ cm corresponding to the intrusion level, for Case 1. Green dot gives the location of the conductivity probe.

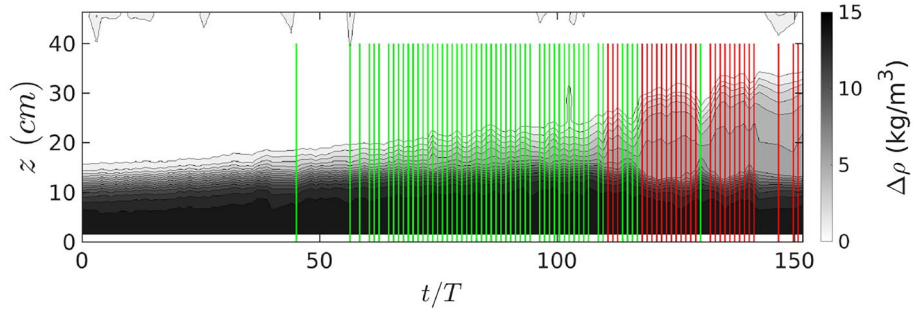

Figure 3. Hovmöller diagrams of the vertical density profile for Case 1. Detection of intrusion regimes: vertical green and red lines represent the detected laminar and turbulent intrusions, respectively.

density anomaly ρ_1 and stopping for $z_2 < z_1$ and $\rho_2 > \rho_1$, based on the four zones described here-above. These exponential fits are pertinent in each zone (see Fig. 4), here we focus on the intrusion zone. Note that the data disappears behind the piece-wise fit.

The exponential shape of the turbulent intrusion delivers the scale height $\tilde{h} = \kappa/w$[25], which is the inverse of the e-folding coefficient. The thickness h of the intrusion is represented by the vertical extension z of the red line in Fig. 4a and b, determined as the vertical distance between the two extrema of the vertical density gradient of

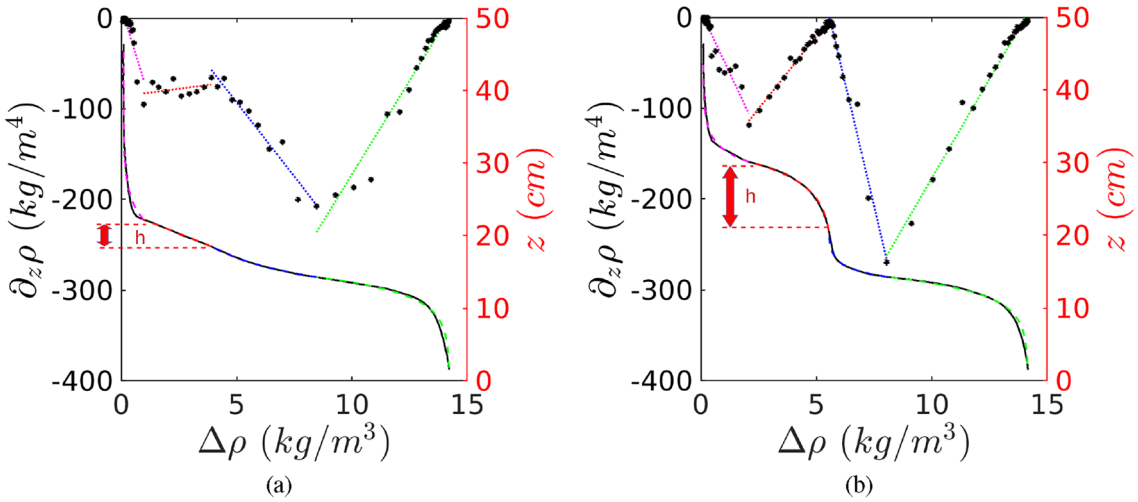

Figure 4. Same as Fig. 2a and c, with dashed lines representing piece-wise linear fits and continues lines the corresponding piece-wise exponential fits for $t/T = 84$ (**a**) and $t/T = 140$ (**b**) for Case 1. Red arrows in (**a**) and (**b**) show the thickness h measured from the vertical extension of the red exponential fit.

this portion of the density profile. Note that the ratio $h/\tilde{h}$ represents the Peclet number $Pe = Re_w Sc = h/\tilde{h}$, with $Re_w = wh/\nu$ and $Sc = \nu/\kappa$ and is a measure of the importance of diffusivity with respect to upward advection. If $Pe > 1$, the upward advection w plays a significant role in the near-slope dynamics resulting in the observed exponential shape and the intrusion is turbulent. $Pe = h/\tilde{h}$ has an averaged value of 2.5 for turbulent intrusions, which demonstrates that $\tilde{h}$ is well defined. If $Pe < 1$, the advective term becomes negligible compared to diffusion, giving rise to the observed linear shape and the intrusion is laminar. A histogram of all events for all the experiments considered is given in Fig. 5a. The local maxima criteria is given in the same figure by green and red coloring. The two independent criteria show a fair agreement. The vorticity sign criteria corroborates the observations from the $h/\tilde{h}$ criteria, with 84% of events with $\zeta < 0$ corresponding to turbulent intrusions, and 82% of laminar intrusions corresponding to $\zeta > 0$. We point out that $\tilde{h}$ is only meaningful in the case of turbulent intrusions where $\tilde{h} < h$, i.e. when $Pe > 1$. In the next subsection we derive a theoretical model based on the critical Froude number which enables to predict $\tilde{h}$ as a function of the overall experimental parameters.

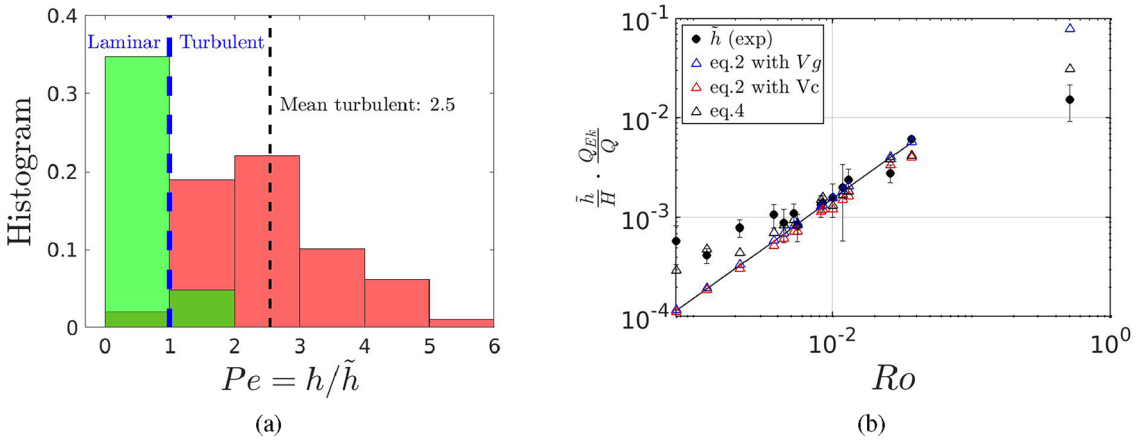

Figure 5. (**a**) Histogram of laminar and turbulent intrusions using the criteria $Pe \lessgtr 1$. The local maxima criteria is given in the same figure by green and red coloring. The averaged value for the turbulent intrusions is 2.5. (**b**) Measured scale height $\langle\tilde{h}\rangle$ obtained from averaged values of all the turbulent intrusions of a given experiment, for all the experiments (black dots) except for experiment Case 15 with a very low rotation ($Ro = 0.51$), compared to the geostrophic model (blue triangles), geostrophic/cyclostrophic model with $R = 4$ m (red triangles), geostrophic/cyclostrophic model and Poincaré waves with $k = 10$ m. The continuous line represents a linear regression with a slope of s/F^2 and $F \approx 0.8$.

Model for the scale height

To obtain an analytical expression for the scale height, the definition of the Froude number $F = V_g/\sqrt{g'\tilde{h}}$ can be used, where V_g is the characteristic velocity scale which we first assume to be the geostrophic velocity. When the Froude number is subcritical a moving fluid layer can be laminar, when it becomes supercritical hydraulic jumps occur leading to turbulent dynamics. The turbulence leads to increased vertical mixing of density and momentum and thickens the moving layer until its Froude number becomes subcritical.

Setting the critical value $F = 0.8$ for a rotating gravity current[27,28], the scale height is given by

$$\tilde{h} = \frac{V_g^2}{g'F^2} = \frac{g'}{F^2 f^2}s^2 \qquad \text{and in non-dimensional form} \qquad \frac{\tilde{h}}{H} = \frac{Q_j}{Q_{Ek}}Ro\frac{s}{F^2}, \tag{2}$$

where $Q_{Ek} = 2\pi R T_{Ek}$, with the intrusion radius R =4 m and $T_{Ek} = v_g\delta_E$ the Ekman transport and $\delta_E = \sqrt{2\nu/f}$. The Rossby number Ro is based on the horizontal scale $\mathscr{L} = Q_j/T_{Ek}$ with $\mathscr{L}$ representing the distance needed to drain the initial flux Q_j through the Ekman layer, already defined by Lane-Serff and Baines[23]. Since the term s/F^2 is constant, the normalized relation in Eq. (2) states that the variation of the scale height $\tilde{h}$ is directly proportional to the ratio between the injected volume Q_j and the total Ekman transport Q_{Ek} multiplied by the Rossby number Ro. This proportionality can be observed in Fig. 5b, where the normalized and compensated scale heights are plotted as black symbols, for all the experiments. The experimental data (except Case 15 with a low rotation) can be fitted with a linear relation (continuous line) which slope corresponds to s/F^2 with $F = 0.8$ as given in Eq. (2) and, consequently, in agreement with the literature[27,28].

A more sophisticated model can be obtained taking into account the cyclostrophy, when the relative vorticity ζ becomes comparable to the planetary vorticity f. The effect of both geostrophy and cyclostrophy gives an alternative relation for the velocity scale, now V_c, to be included in Eq. (2) rather than V_g, which can be derived using the gradient balance[29]

$$fV_c + \frac{2V_c^2}{R} = g's. \tag{3}$$

To further improve the prediction of $\tilde{h}$ for higher rotation rates, the effect of dispersive Poincaré waves should be considered, which replace shallow water waves in rotating flows. Their group velocity is given by $C_{PC} = \frac{g'\tilde{h}k}{\sqrt{f^2+g'\tilde{h}k^2}}$ (see[30]), to be used in a revised definition of the Froude number. This leads to

$$\tilde{h} = \frac{V_c^2}{2F^2g'} + \sqrt{\frac{V_c^4}{4g'^2F^4} + \frac{V_c^2f^2}{g'^2k^2F^2}}, \tag{4}$$

where k is the horizontal wave number characteristic of the Poincaré waves which is estimated to be of the order $k = 10\ \mathrm{m}^{-1}$.

These two revised models are plotted in Fig. 5b and compared to the purely geostrophic model using V_g (blue symbols) and the experimental data (black circles). The purely geostrophic model fails to predict $\tilde{h}$ for a low rotation rate, whereas the cyclostrophic model [Eq. (2), red symbols] enables to improve the prediction. These models do not predict well the experimental data for high rotation rates. Instead, Eq. (4) (black triangles in Fig. 5b) well predicts the full range of experimental data over 3 decades of the Rossby number Ro.

Interior or boundary mixing?

Topographic features are known to strongly increase the mixing in the deep ocean[31], but quantitative estimates are scant. An implicit hypothesis made so far is that the turbulent fluxes occur in the gravity current phase and that the vertical density structure of the intrusion is conserved after the current has detached from the boundary, i.e. that no mixing occurs in the interior. In order to ascertain that no mixing takes place in the interior, we compute the Richardson number defined as:

$$Ri = -\frac{g}{\rho_t}\frac{\partial_z\rho}{(\partial_z U_h)^2} = \frac{N^2}{(\partial_z U_h)^2}, \tag{5}$$

where U_h is the horizontal component of the velocity and N the Brunt–Väissälä frequency. To combine the velocity and density measurement having different spatial and temporal resolutions, a discretised calculation of the Richardson number has been performed, using upward and central approximations for the density and horizontal velocity, respectively.

The lowest Richardson numbers are located at the lower interface of the intrusion, but remain well above the critical condition $Ri = 0.25$ for all the considered experiments. This can be seen in Fig. 6a where we superpose the temporal variation of the density anomaly (blue lines), the strain $S^2 = (\partial_z U_h)^2$ and the locations where $1 < Ri < 10$ (green dots) and $0.8 < Ri < 1$ (red dots) for experiment Case 1. For the same experiment, the instantaneous vertical profiles of N^2 and S^2 (black and blue curves, respectively) at $t/T = 84$, representative of a laminar intrusion, are plotted in Fig. 6b. The highest density gradients are located at the upper and lower boundaries of the intrusion layer. The strain S^2 has the largest value close to the bottom of the intruding layer, explaining the observed low values of the Richardson number in this region. Note that low Richardson numbers are not detected at the upper interface, neither for the laminar nor for the turbulent intrusions.

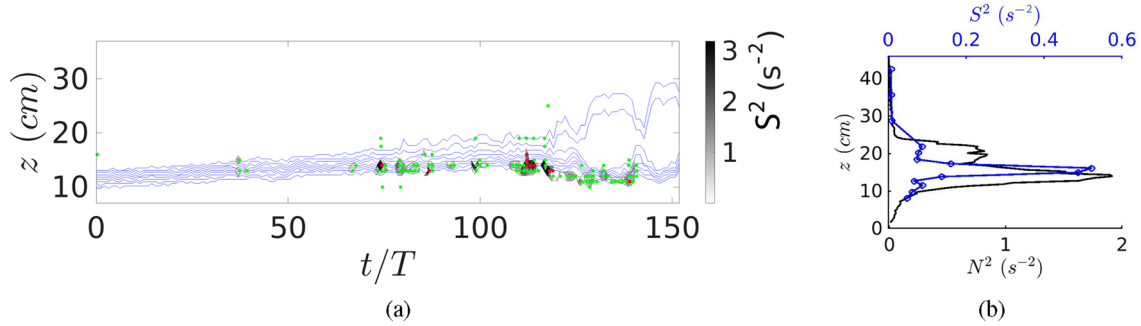

Figure 6. (**a**) Hovmöller diagram showing haloclines (blue lines) and the strain $S^2 = (\partial_z U_h)^2$ concentrated at the lower boundary of the intrusion for Case 1. The green dots are relative to $1 < Ri < 10$ and the red dots to $0.8 < Ri < 1$. (**b**) For the same experiment, instantaneous vertical profiles of N^2 and S^2 (black and blue curves, respectively) at $t/T = 84$ representative of a laminar intrusion.

To corroborate the fact that the saline water has mixed on the slope area rather than during the intruding phase in the ocean interior, mostly through dense water cascading, we consider in Fig. 7 the vertical density profile of the laminar (black curves) and turbulent (red curves) intrusions for experiment Case 10 at different times after the initial density structure has been subtracted. For this experiment, the injected density is exactly the average of the top and bottom densities ($\rho_b = 1009$ kg m^{-3}, $\rho_j = 1004.2$ kg m^{-3}, $\rho_t = 999.6$ kg m^{-3}), and is hence initially symmetric. The vertical shape for laminar intrusions (black curves) is close to symmetric and this suggests that very low mixing happened on the slope. Turbulent intrusions, instead, present a pronounced asymmetry: a strong gradient is present at the lower boundary and a smoother gradient at the upper boundary. This is also in accord with observations[32].

Discussion and conclusions

Two distinct regimes for the intrusion of rotating gravity currents from the slope into the interior have been identified: laminar intrusions driven by Ekman dynamics and turbulent intrusions subject to turbulent mixing on the slope. The former gives rise to a local close-to-linear variation of the density with depth, whereas the latter leads to an exponential shape for the density structure of the intrusion. The computed Richardson number is well above the critical value of 0.25 demonstrating that no turbulent mixing takes place in the interior, but rather during the gravity current phase on the slope.

Using the diffusion–advection model[19], the e-folding coefficient w/κ of the exponential fits (also called the scale height) has been obtained, showing a balance between upward advection and downward diffusion of dense water. The two distinct intrusion regimes have been detected using the scale height: for laminar intrusions, the e-folding scale height w/κ is small, the diffusivity is hence predominant over the upward velocity. For turbulent intrusions, a significant e-folding scale height underlines the influence of a strong upward advection w in the dynamics above the slope, resulting in the characteristic exponential shape. For turbulent intrusions, we derive a relationship which permits to determine the e-folding scale height from the variables s, Ro, Q_j and T_{Ek} which are set from the initial experimental parameters.

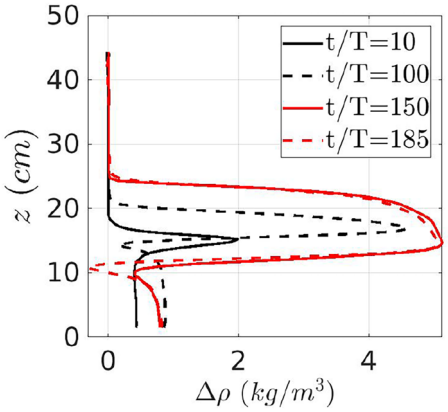

Figure 7. Vertical intrusion profiles for Case 10 with the injected density initially symmetric with respect to the densities of the top and bottom layers, plotted at different times for laminar (black lines) and turbulent (red lines) intrusions corrected by the measured halocline elevation. The laminar intrusions exhibit a symmetric shape, while the turbulent intrusions has a pronounced asymmetric shape.

The e-folding scale height delivers a criteria to discriminate between turbulent and laminar intrusions: the intrusion is laminar when $h/\tilde{h} < 1$, whereas it is turbulent when $h/\tilde{h} > 1$ and $\tilde{h}$ is well defined. Further criteria based on the local maxima of the vertical density gradient and on the vorticity sign corroborate the results obtained with the first criteria. For turbulent intrusions we found that the thickness of the current h is, in average, 2.5 times the scale height $\tilde{h}$. An analytical model for predicting the scale height $\tilde{h}$ has been derived, which is able to predict its value over three decades of the Rossby number.

The motivation for this work was to understand the dynamics of intruding dense water on slopes in the ocean and we compare how this work relates to observations. The external parameters of the experiment where chosen so that the relevant non-dimensional parameters cover a wide range of scales so that they are representative of a large variety of oceanic intruding gravity currents, e.g. the downslope flow dominating as the Adriatic Outflow into the Ionian Sea[33] and the rotation dominating as the Gibraltar outflow[34]. The similarity could not be achieved for the Reynolds number, which is many orders of magnitude larger in the ocean, although the size of the Coriolis platform allows for turbulent dynamics. We first consider observational data relative of the intrusion of dense water into the Weddell Sea. Recent investigations conducted between 2017 and 2019, and analyzed in 2023, have determined the thickness of a gravity current to about 150 m[9,35]. For a slope of 3.2×10^{-2} (typical for the Weddell Sea), our model predicts a scale height of $\tilde{h} \approx 45$ m which translates to a thickness of $h \approx \tilde{h} \cdot 2.5 \approx 112.5$ m. Intruding gravity currents of Mediterranean water at the Strait of Gibraltar, lead to intrusions further downstream giving rise to anti-cyclonic Mediterranean Eddies (Meddies). In 1992, Meddy Bobby was discovered southeast of the Azores, far from the Strait of Gibraltar, at approximately 34.75° N, 23.5° W. Its water properties, density structure, and velocity field have been studied by Pingree and Le Cann[36]. They suggest that Meddy Bobby remained relatively stable during its journey, with only minor mixing observed at its edges. With a radius of about 30 km, its vertical structure (cf. Fig. 9 in[36]) shows a dense water mass moving anti-cyclonically, with isopycnals condensed at the lower surface which is in accord with what we observed. Its thickness of about 900 m suggests, using our model, a slope of 1.5×10^{-2}, which is typical for the shelf off-shore of the Portuguese coast where the gravity current evolves before it intrudes into the interior. Note that in this case of a rapidly rotating Meddy, the cyclostrophy dominates over geostrophy. The results shows clearly that our model enables to connect directly laboratory experiments and deep sea observations, and emphasizes the importance of laboratory experiments in understanding climate dynamics.

Data availability

All data used is available upon request (eletta.negretti@legi.cnrs.fr, LEGI/CORIOLIS).

Received: 19 January 2024; Accepted: 29 April 2024
Published online: 04 May 2024

References

1. IPCC, A. W. Ar6 climate change 2021: The physical science basis. *Agenda* **6**, 333 (2021).
2. Vic, C. *et al.* Eddy topography interactions and the fate of the Persian Gulf outflow. *J. Geophys. Res. Oceans* **120**, 6700–17. https://doi.org/10.1002/2015JC011033 (2016).
3. Cardin, V., Wirth, A., Khosravi, M. & Gacic, M. South adriatic recipes: Estimating the vertical mixing in the deep pit. *Front. Mar. Sci.* **7**, 565982. https://doi.org/10.3389/fmars.2020.565982 (2020).
4. Wirth, A. On the basic structure of oceanic gravity currents. *Ocean Dyn.* **59**, 551–563. https://doi.org/10.1007/s10236-009-0202-9 (2009).
5. Baringer, M. & Price, J. A review of the physical oceanography of the Mediterranean outflow. *Mar. Geol.* **155**, 63–82 (1999).
6. Hartmut, P., Johns, W., Bower, A. & Fratantoni, D. Mixing and entrainment in the red sea outflow plume. Part I: Plume structure. *J. Phys. Oceanogr.* **35**, 569–583 (2005).
7. Johns, W. *et al.* Observations of seasonal exchange through the straits of Hormuz and the inferred heat and freshwater budgets of the Persian gulf. *J. Geophys. Res. Oceans* **108**, 1–18. https://doi.org/10.1029/2003JC001881 (2003).
8. Bruce, J. Eddies southwest of the Denmark strait. *Deep Sea Res. Part I Oceanogr. Res. Pap.* **42**, 13–29 (1995).
9. Price, J. & Baringer, M. Outflows and deep water production by marginal seas. *Prog. Oceanogr.* **33**, 161–200 (1994).
10. Cooper, L. & Vaux, D. Cascading over the continental slope of water from the Celtic sea. *J. Mar. Biol. Assoc. U.K.* **28**, 719–750. https://doi.org/10.1017/S0025315400023547 (1999).
11. Gill, A. Circulation and bottom water production in the Weddell sea. *Deep Sea Res. Oceanogr. Abstr.* **20**, 111–140. https://doi.org/10.1016/0011-7471(73)90048-X (1973).
12. Shapiro, G. I. & Hill, A. E. Dynamics of dense water cascades at the shelf edge. *J. Phys. Oceanogr.* **27**, 2381–2394. https://doi.org/10.1175/1520-0485(1997)027<2381:DODWCA>2.0.CO;2 (1997).
13. Emms, P. Streamtube models of gravity currents in the ocean. *Deep Sea Res. Part I Oceanogr. Res. Pap.* **44**, 1575–1610. https://doi.org/10.1016/S0967-0637(97)00047-2 (1997).
14. Wåhlin, A. & Walin, G. Downward migration of dense bottom currents. *Environ. Fluid Mech.* **1**, 257–279. https://doi.org/10.1023/A:1011520432200 (2001).
15. Ungarish, M. On the spinup and spreadout of a cartesian gravity current on a slope in a rotating system. *J. Fluid Mech.* **943**, A31. https://doi.org/10.1017/jfm.2022.447 (2022).
16. Nof, D. The translation of isolated cold eddies on a sloping bottom. *Deep Sea Res. Part A Oceanogr. Res. Pap.* **30**, 171–182. https://doi.org/10.1016/0198-0149(83)90067-5 (1983).
17. Legg, S. *et al.* Improving oceanic overflow representation in climate models: The gravity current entrainment climate process team. *Bull. Am. Meteorol. Soc.* **90**, 657–670 (2009).
18. Munk, W. Abyssal recipes. *Deep Sea Res. Oceanogr. Abstr.* **13**, 707–730 (1966).
19. Munk, W. & Wunsch, C. Abyssal recipes II: Energetics of tidal and wind mixing. *Deep Sea Res. Part I Oceanogr. Res. Pap.* **45**, 1977–2010. https://doi.org/10.1016/S0967-0637(98)00070-3 (1998).
20. Kunze, E. & Llewellyn Smith, S. The role of small-scale topography in turbulent mixing of the global ocean. *Oceanography* **17**, 55–64. https://doi.org/10.5670/oceanog.2004.67 (2004).
21. van Haren, H. & Gostiaux, L. Detailed internal wave mixing above a deep-ocean slope. *Ocean Sci.* **70**, 173–197 (2012).

22. Negretti, M., Tucciarone, F. & Wirth, A. Intruding gravity currents and re-circulation in a rotating frame: Laboratory experiments. *Phys. Fluids* **33**, 096607. https://doi.org/10.1016/j.ocemod.2022.101994 (2021).
23. Lane-Serff, G. & Baines, P. Eddy formation by dense flows on slopes in a rotating fluid. *J. Fluid. Mech.* **363**, 229–252. https://doi.org/10.1017/S0022112098001013 (1998).
24. Wirth, A. & Negretti, M. E. Intruding gravity currents and their recirculation in a rotating frame: Numerical results. *Ocean Model.* **11**, 101994. https://doi.org/10.1016/j.ocemod.2022.101994 (2022).
25. Wunsch, C. A simplified ocean physics? Revisiting abyssal recipes. *J. Phys. Oceanogr.* **53**, 1387–1400 (2023).
26. Tassigny, A., Negretti, M. & Wirth, A. On the turbulent structures generated by intruding and rotating downslope gravity currents. *Phys. Rev. Fluids*https://doi.org/10.5194/egusphere-egu24-5897 *(2023)*.
27. Killworth, P. On the rate of descent of overflows. *J. Geophys. Res.* **106**, 22267–22275. https://doi.org/10.1029/2000JC000707 (2001).
28. Wirth, A. Laminar and weakly turbulent oceanic gravity currents performing inertial oscillations. *Ocean Sci.* **8**, 301–317 (2012).
29. Ioannou, A. *et al.* Cyclostrophic corrections of AVISO/DUACS surface velocities and its application to mesoscale eddies in the Mediterranean sea. *J. Geophys. Res. Oceans* **124**, 8913–8932. https://doi.org/10.1029/2019JC015031 (2019).
30. Pedlosky, J. *Waves in the Ocean and Atmosphere: Introduction to Wave Dynamics* Vol. 260 (Springer, 2003).
31. Polzin, K. & McDougall, T. Chapter 7–Mixing at the ocean's bottom boundary. In *Ocean Mixing* (eds Meredith, M. & Naveira Garabato, A.) 145–180 (Elsevier, 2022).
32. Artale, V. *et al.* Linking mixing processes and climate variability to the heat content distribution of the eastern Mediterranean abyss. *Sci. Rep.* **8**, 1137. https://doi.org/10.1038/s41598-018-29343-4 (2018).
33. Gačić, M. *et al.* Impact of dense-water flow over a sloping bottom on open-sea circulation: Laboratory experiments and an Ionian Sea (Mediterranean) example. *Ocean Sci.* **17**, 975–996. https://doi.org/10.5194/os-17-975-2021 (2021).
34. Roustan, J.-B., Bordois, L., Dumas, F., Auclair, F. & Carton, X. In situ observations of the small-scale dynamics at Camarinal Sill—Strait of Gibraltar. *J. Geophys. Res. Oceans* **128**, e2023JC019738. https://doi.org/10.1029/2023JC019738 (2023).
35. Pinner, O., Janout, M. & Kanzow, T. *Distribution of Kinetic Energy in the Weddell Sea Gravity Current*. Tech. Rep, Copernicus Meetings (2023).
36. Pingree, R. & Le Cann, B. Structure of a meddy (Bobby 92) southeast of the Azores. *Deep Sea Res. Part I Oceanogr. Res. Pap.* **40**, 2077–2103 (1993).

Acknowledgements

The work was funded by SHOM under contract number 20CP03. We thank C. Brun and A. Tassigny for discussions and O. Pinner for sharing observational data.

Author contributions

M.E.N. designed and conducted the laboratory experiments. A.W. participated in the design of the experiment. S.R. and M.E.N. processed and analyzed the experimental data. S.R., M.E.N. and A.W. performed the discussion and interpretation of the results, and wrote the manuscript.

Competing interests

The authors declare no competing interests.

Additional information

Correspondence and requests for materials should be addressed to S.R.

Reprints and permissions information is available at www.nature.com/reprints.

Publisher's note Springer Nature remains neutral with regard to jurisdictional claims in published maps and institutional affiliations.

Open Access This article is licensed under a Creative Commons Attribution 4.0 International License, which permits use, sharing, adaptation, distribution and reproduction in any medium or format, as long as you give appropriate credit to the original author(s) and the source, provide a link to the Creative Commons licence, and indicate if changes were made. The images or other third party material in this article are included in the article's Creative Commons licence, unless indicated otherwise in a credit line to the material. If material is not included in the article's Creative Commons licence and your intended use is not permitted by statutory regulation or exceeds the permitted use, you will need to obtain permission directly from the copyright holder. To view a copy of this licence, visit http://creativecommons.org/licenses/by/4.0/.

© The Author(s) 2024

Bibliography

[1] E. Abrahamsen, A. Meijers, K. Polzin, A. Garabato, B. King, Y. Firing, J. Sallée, K. Sheen, A. Gordon, B. Huber, and M. Meredith. Stabilization of dense antarctic water supply to the atlantic ocean overturning circulation. *Nature Climate Change*, 9: 742–746, 2019. doi: 10.1038/s41558-019-0561-2.

[2] M. Baringer and J. Price. Momentum and energy balance of the mediterranean outflow. *Journal of Physical Oceanography*, 27(8):1678 – 1692, 1997. doi: https://doi.org/10.1175/1520-0485(1997)027%3C1678:MAEBOT%3E2.0.CO;2.

[3] T. B. Benjamin. Gravity currents and related phenomena. *Journal of Fluid Mechanics*, 31(2):209–248, 1968. doi: 10.1017/S0022112068000133.

[4] N. Bindoff, W. Cheung, J. Kairo, J. Aristegui, V. Guinder, R. Hallberg, N. Hilmi, N. Jiao, M. Karim, L. Levin, S. O'Donoghue, S. Purca, B. Rinkevich, T. Suga, A. Tagliabue, P. Williamson, S. Acar, J. Alava, E. Allison, and C. Whalen. *Changing Ocean, Marine Ecosystems, and Dependent Communities (09 SROCC Ch05 FINAL-1)*, pages 447–588. Intergovernmental Panel on Climate Change (IPCC), 2019. doi: https://doi.org/10.1017/9781009157964.007.

[5] K. Borenäs and P. Lundberg. On the deep-water flow through the faroe bank channel. *Journal of Geophysical Research: Oceans*, 93(C2):1281–1292, 1988. doi: https://doi.org/10.1029/JC093iC02p01281.

[6] K. Bowden. The dynamics of flow on a submarine ridge. *Tellus*, 12(4):419–426, 1960. doi: https://doi.org/10.3402/tellusa.v12i4.9415.

[7] A. Bower, H. Hunt, and J. Price. Character and dynamics of the red sea and persian gulf outflows. *Journal of Geophysical Research: Oceans*, 105(C3):6387–6414, 2000. doi: https://doi.org/10.1029/1999JC900297.

[8] D. Boyer, D. Sous, and J. Sommeria. Laboratory experiments on along-slope flows in homogeneous and stratified rotating fluids. *Dynamics of Atmospheres and Oceans*, 46 (1):19–35, 2009. doi: https://doi.org/10.1016/j.dynatmoce.2008.10.002.

[9] K. H. Brink and S. J. Lentz. Buoyancy arrest and bottom ekman transport. part i: Steady flow. *Journal of Physical Oceanography*, 40(4):621 – 635, 2010. doi: 10.1175/2009JPO4266.1.

[10] D. R. Caldwell, C. W. Van Atta, and K. N. Helland. A laboratory study of the turbulent ekman layer. *Geophysical Fluid Dynamics*, 3(2):125–160, 1972. doi: 10.1080/03091927208236078.

[11] C. Cenedese and C. Adduce. Mixing in a density-driven current flowing down a slope in a rotating fluid. *Journal of Fluid Mechanics*, 604:369–388, 2008. doi: https://doi.org/10.1017/S0022112008001237.

[12] C. Cenedese, J. A. Whitehead, T. A. Ascarelli, and M. Ohiwa. A dense current flowing down a sloping bottom in a rotating fluid. *Journal of Physical Oceanography*, 34(1): 188 – 203, 2004. doi: 10.1175/1520-0485(2004)034⟨0188:ADCFDA⟩2.0.CO;2.

[13] J. Davarpanah, M. G. Wells, J. Peakall, R. M. Dorrell, R. E. Thomas, G. M. Keevil, S. E. Darby, J. Sommeria, S. Viboud, and T. Valran. Influence of coriolis force upon bottom boundary layers in a large-scale gravity current experiment: Implications for evolution of sinuous deep-water channel systems. *Journal of Geophysical Research: Oceans*, 125(3):e2019JC015284, 2020. doi: https://doi.org/10.1029/2019JC015284.

[14] G. Dietrich. Überströmung des Island-Färöer-Rückens in Bodennähe nach Beobachtungen mit dem Forschungsschiff "Anton Dohrn". *Deutsche Hydrographische Zeitschrift*, 9(2):78–89, 1956. doi: 10.1007/BF02021146.

[15] H. Dooley and J. Meincke. Circulation and water masses in the Faroese Channels during overflow '73. *Deutsche Hydrographische Zeitschrift*, 34(2):41–55, 1981. doi: 10.1007/BF02226585.

[16] C. O. Dufour, A. K. Morrison, S. M. Griffies, I. Frenger, H. Zanowski, and M. Winton. Preconditioning of the weddell sea polynya by the ocean mesoscale and dense water overflows. *Journal of Climate*, 30(19):7719 – 7737, 2017. doi: 10.1175/JCLI-D-16-0586.1.

[17] S. Décamp. *Étude en laboratoire d'un courant de gravité turbulent sur un talus continental*. PhD thesis, Université Joseph Fourier (Grenoble ; 1971-2015), 2005.

[18] G. Egbert, A. Bennett, and M. Foreman. Topex/poseidon tides estimated using a global inverse model. j of geoph res 99(c12):24821-24852. *Journal of Geophysical Research*, 99, 1995. doi: 10.1029/94JC01894.

[19] V. W. Ekman. On the influence of the earth's rotation on ocean currents. *Arkiv for Matematik, Astronomi och Fysik*, 2(11), 1905.

[20] T. H. Ellison and J. Turner. Turbulent entrainment in stratified flows. *Journal of Fluid Mechanics*, 6:423 – 448, 1959. doi: https://doi.org/10.1017/S0022112059000738.

[21] D. Etling, F. Gelhardt, U. Schrader, F. Brennecke, G. Kühn, G. Chabert d'Hieres, and H. Didelle. Experiments with density currents on a sloping bottom in a rotating fluid. *Dynamics of Atmospheres and Oceans*, 31(1):139–164, 2000. doi: https://doi.org/10.1016/S0377-0265(99)00031-7.

[22] D. Farmer and L. Armi. The flow of atlantic water through the strait of gibraltar. *Progress in Oceanography*, 21(1):1–103, 1988. doi: https://doi.org/10.1016/0079-6611(88)90055-9.

[23] N. Fofonoff and R. Millard Jr. Algorithms for the computation of fundamental properties of seawater. *UNESCO Technical Papers in Marine Sciences*, 44, 1983. doi: DOI:https://doi.org/10.25607/OBP-1450.

[24] A. Foldvik, T. Gammelsrød, S. Østerhus, E. Fahrbach, G. Rohardt, M. Schröder, K. W. Nicholls, L. Padman, and R. A. Woodgate. Ice shelf water overflow and bottom water formation in the southern weddell sea. *Journal of Geophysical Research: Oceans*, 109 (C2), 2004. doi: https://doi.org/10.1029/2003JC002008.

[25] T. Foster and E. Carmack. Frontal zone mixing and antarctic bottom water formation in the southern weddell sea. *Deep Sea Research and Oceanographic Abstracts*, 23(4): 301–317, 1976. doi: https://doi.org/10.1016/0011-7471(76)90872-X.

[26] C. Garrett, P. Maccready, and P. Rhines. Boundary mixing and arrested ekman layers: Rotating stratified flow near a sloping boundary. *Annu. Rev. Fluid Mech.*, 25:291–323, 1993. doi: 10.1146/annurev.fl.25.010193.001451.

[27] A. Gill. Circulation and bottom water production in the weddell sea. *Deep Sea Res. and Oceanogr. Abstracts*, 20(2):111–140, 1973. doi: https://doi.org/10.1016/0011-7471(73)90048-X.

[28] J. Girton and T. Sanford. Descent and modification of the overflow plume in the denmark strait. *Journal of Physical Oceanography*, 33(7):1351 – 1364, 2003. doi: 10.1175/1520-0485(2003)033⟨1351:DAMOTO⟩2.0.CO;2.

[29] J. B. Girton and T. B. Sanford. Velocity profile measurements of the denmark strait overflow. *International WOCE Newslett.*, 37:28–30, 1999.

[30] H. P. Greenspan and L. N. Howard. On a time-dependent motion of a rotating fluid. *Journal of Fluid Mechanics*, 17(3):385–404, 1963. doi: 10.1017/S0022112063001415.

[31] M. Greenwald. Beyond benchmarking—how experiments and simulations can work together in plasma physics. *Computer Physics Communications*, 164(1):1–8, 2004. doi: https://doi.org/10.1016/j.cpc.2004.06.001.

[32] R. W. Griffiths and E. J. Hopfinger. Gravity currents moving along a lateral boundary in a rotating fluid. *Journal of Fluid Mechanics*, 134:357–399, 1983. doi: https://doi.org/10.1017/S0022112083003407.

[33] T. Gross and A. Nowell. Mean flow and turbulence scaling in a tidal boundary layer. *Continental Shelf Research*, 2(2):109–126, 1983. doi: https://doi.org/10.1016/0278-4343(83)90011-0.

[34] B. Hansen and B. Turrell. Decreasing overflow from the nordic seas into the atlantic ocean through the faroe bank channel sinc. *Nature*, 2001. doi: https://doi.org/10.1038/35082034.

[35] P. Hartmut, W. Johns, A. Bower, and D. Fratantoni. Mixing and entrainment in the red sea outflow plume. part i: Plume structure. *J. Phys. Oceanogr.*, 35(5):569–583, 2005. doi: https://journals.ametsoc.org/view/journals/phoc/35/5/jpo2679.1.xml.

[36] J. Harvey. The topography of the south-western faroe channel. *Deep Sea Research and Oceanographic Abstracts*, 12(2):121–127, 1965. doi: https://doi.org/10.1016/0011-7471(65)90018-5.

[37] C. Heuzé. Antarctic bottom water and north atlantic deep water in cmip6 models. *Ocean Science*, 17(1):59–90, 2021. doi: 10.5194/os-17-59-2021.

[38] J. Holton. The influence of viscous boundary layers on transient motions in a stratified rotating fluid. part i. *Journal of Atmospheric Sciences*, 22(4):402 – 411, 1965. doi: 10.1175/1520-0469(1965)022⟨0402:TIOVBL⟩2.0.CO;2.

[39] G. C. Howroyd and P. R. Slawson. The characteristics of a laboratory produced turbulent ekman layer. *Boundary-Layer Meteorology*, 8(2):201–219, 1975. doi: https://doi.org/10.1007/BF00241337.

[40] C. S. HÄRTEL, E. MEIBURG, and F. NECKER. Analysis and direct numerical simulation of the flow at a gravity-current head. part 1. flow topology and front speed for slip and no-slip boundaries. *Journal of Fluid Mechanics*, 418:189–212, 2000. doi: 10.1017/S0022112000001221.

[41] V. Ivanov, G. Shapiro, J. Huthnance, D. Aleynik, and P. Golovin. Cascades of dense water around the world ocean. *Progress in Oceanography*, 60(1):47–98, 2004. doi: https://doi.org/10.1016/j.pocean.2003.12.002.

[42] A. Jagannathan, K. Srinivasan, J. McWilliams, J. Molemaker, and A. Stewart. Evolution of bottom boundary layers on three dimensional topography—buoyancy adjustment and instabilities. *Journal of Geophysical Research: Oceans*, 128(4): e2023JC019705, 2023. doi: https://doi.org/10.1029/2023JC019705.

[43] W. E. Johns, F. Yao, D. B. Olson, S. A. Josey, J. P. Grist, and D. A. Smeed. Observations of seasonal exchange through the straits of hormuz and the inferred heat and freshwater budgets of the persian gulf. *Journal of Geophysical Research: Oceans*, 108 (C12), 2003. doi: https://doi.org/10.1029/2003JC001881.

[44] P. Killworth. Mixing of the weddell sea continental slope. *Deep Sea Research*, 24(5): 427–448, 1977. doi: https://doi.org/10.1016/0146-6291(77)90482-9.

[45] P. Killworth. On the rate of descent of overflows. *J. Geophys. Res.*, 106:22267–22275, 2001. doi: https://doi.org/10.1029/2000JC000707.

[46] W. Krauss and R. Käse. Eddy formation in the denmark strait overflow. *Journal of Geophysical Research: Oceans*, 103(C8):15525–15538, 1998. doi: https://doi.org/10.1029/98JC00785.

[47] E. Kunze and S. Llewellyn Smith. The role of small-scale topography in turbulent mixing of the global ocean. *Oceanography*, 17(1):55–64, 2004. doi: https://doi.org/10.5670/oceanog.2004.67.

[48] G. Lane-Serff and P. Baines. Eddy formation by dense flows on slopes in a rotating fluid. *J. Fluid. Mech.*, 363:229?252, 1998. doi: https://doi.org/10.1017/S0022112098001013.

[49] J. Ledwell, A. Watson, and C. Law. Evidence for slow mixing across the pycnocline from an open-ocean tracer-release experiment. *Nature*, 364:701–703, 1993. doi: https://doi.org/10.1038/364701a0.

[50] A. Lee and D. Ellett. On the contribution of overflow water from the norwegian sea to the hydrographic structure of the north atlantic ocean. *Deep Sea Research and Oceanographic Abstracts*, 12(2):129–142, 1965. doi: https://doi.org/10.1016/0011-7471(65)90019-7.

[51] A. Lee and D. Ellett. On the water masses of the northwest atlantic ocean. *Deep Sea Research and Oceanographic Abstracts*, 14(2):183–190, 1967. doi: https://doi.org/10.1016/0011-7471(67)90004-6.

[52] S. Legg, B. Briegleb, Y. Chang, E. P. Chassignet, G. Danabasoglu, T. Ezer, A. L. Gordon, S. Griffies, R. Hallberg, L. Jackson, et al. Improving oceanic overflow representation in climate models: the gravity current entrainment climate process team. *Bulletin of the American Meteorological Society*, 90(5):657–670, 2009.

[53] P. Linden. *Gravity currents – theory and laboratory experiments*, page 13–51. Cambridge University Press, 2012. doi: https://doi.org/10.1017/CBO9780511920196.002.

[54] P. F. Linden and J. E. Simpson. Gravity-driven flows in a turbulent fluid. *Journal of Fluid Mechanics*, 172:481–497, 1986. doi: 10.1017/S0022112086001829.

[55] D. Liu, K. Alobaidi, and M. Valyrakis. The assessment of an acoustic doppler velocimetry profiler from a user's perspective. *Acta Geophysica*, 70, 2022. doi: 10.1007/s11600-022-00896-3.

[56] Y. Liu, J. K. Moore, F. Primeau, and W. L. Wang. Reduced co2 uptake and growing nutrient sequestration from slowing overturning circulation. *Nature Climate Change*, 13:83–90, 2023. doi: https://doi.org/10.1038/s41558-022-01555-7.

[57] M. Maggi, E. Hopfinger, J. Sommeria, A. C., S. Viboud, T. Valran, and M. Negretti. Laboratory experiments of rotating stratified exchange flows over a sediment bed. *Advances in Water Resources*, 200:104959, 2025. doi: https://doi.org/10.1016/j.advwatres.2025.104959.

[58] J. Marotzke. Boundary mixing and the dynamics of three-dimensional thermohaline circulations. *Journal of Physical Oceanography*, 27(8):1713 – 1728, 1997. doi: 10.1175/1520-0485(1997)027⟨1713:BMATDO⟩2.0.CO;2.

[59] C. Mauritzen, K. L. Polzin, M. S. McCartney, R. C. Millard, and D. E. West-Mack. Evidence in hydrography and density fine structure for enhanced vertical mixing over the mid-atlantic ridge in the western atlantic. *Journal of Geophysical Research: Oceans*, 107(C10):11–1–11–19, 2002. doi: https://doi.org/10.1029/2001JC001114.

[60] C. Mauritzen, J. Price, T. Sanford, and D. Torres. Circulation and mixing in the faroese channels. *Deep Sea Research Part I: Oceanographic Research Papers*, 52(6):883–913, 2005. doi: https://doi.org/10.1016/j.dsr.2004.11.018.

[61] I. McCave. Chapter 8 size sorting during transport and deposition of fine sediments: Sortable silt and flow speed. In *Contourites*, volume 60, pages 121–142. Elsevier, 2008. doi: https://doi.org/10.1016/S0070-4571(08)10008-5.

[62] M. Meredith, O. Schofield, L. Newman, E. Urban, and M. Sparrow. The vision for a southern ocean observing system. *Current Opinion in Environmental Sustainability*, 5(3):306–313, 2013. doi: https://doi.org/10.1016/j.cosust.2013.03.002.

[63] E. Morozov, D. I. Frey, S. Gladyshev, and V. Gladyshev. Hydrodynamics of the bottom-water flow from the arctic to the atlantic through the strait of denmark. *Izvestiya Atmospheric and Oceanic Physics*, 56(5):479–487, 2020. doi: 10.1134/S0001433820050096.

[64] W. Munk. Abyssal recipes. *Deep Sea Res. and Oceanogr. Abstracts*, 13(4):707–730, 1966. doi: https://www.sciencedirect.com/science/article/pii/0011747166906024.

[65] W. Munk and C. Wunsch. Abyssal recipes ii: energetics of tidal and wind mixing. *Deep Sea Res. Part I Oceanogr. Res. Pap.*, 45(12):1977–2010, 1998. doi: https://doi.org/10.1016/S0967-0637(98)00070-3.

[66] Y. Nagata, R. Kimura, H. Honji, Y. Yamazaki, K. Kawaguchi, and T. Hosoyamada. Laboratory experiments of dense water descending on continental slope. *Deep Ocean Circulation*, 59:333–350, 1993. doi: https://doi.org/10.1016/S0422-9894(08)71335-7.

[67] M. Negretti, F. Tucciarone, and A. Wirth. Intruding gravity currents and re-circulation in a rotating frame: Laboratory experiments. *Phys. Fluids*, 33(9), 2021. doi: https://doi.org/10.1016/j.ocemod.2022.101994.

[68] L. Newman, P. Heil, R. Trebilco, K. Katsumata, A. Constable, E. van Wijk, K. Assmann, J. Beja, P. Bricher, R. Coleman, D. Costa, S. Diggs, R. Farneti, S. Fawcett, S. Gille, K. Hendry, S. Henley, E. Hofmann, T. Maksym, M. Mazloff, A. Meijers, M. Meredith, S. Moreau, B. Ozsoy, R. Robertson, I. Schloss, O. Schofield, J. Shi, E. Sikes, I. Smith, S. Swart, A. Wahlin, G. Williams, M. Williams, L. Herraiz-Borreguero, S. Kern, J. Lieser, R. Massom, J. Melbourne-Thomas, P. Miloslavich, and G. Spreen. Delivering sustained, coordinated, and integrated observations of the southern ocean for global impact. *Frontiers in Marine Science*, 6, 2019. doi: 10.3389/fmars.2019.00433.

[69] K. Nicholls, K. Makinson, and S. Østerhus. Circulation and water masses beneath the northern ronne ice shelf, antarctica. *Journal of Geophysical Research: Oceans*, 109 (C12), 2004. doi: https://doi.org/10.1029/2004JC002302.

[70] D. Nof. The translation of isolated cold eddies on a sloping bottom. *Deep Sea Res. Part A Oceanogr. Res. Pap.*, 30(2):171–182, 1983. doi: https://doi.org/10.1016/0198-0149(83)90067-5.

[71] I. P. on Climate Change (IPCC). *Extremes, Abrupt Changes and Managing Risks*, page 589–656. Cambridge University Press, 2022. doi: https://doi.org/10.1017/9781009157964.008.

[72] I. P. on Climate Change (IPCC). *Ocean, Cryosphere and Sea Level Change*, page 1211–1362. Intergovernmental Panel on Climate Change (IPCC), 2023. doi: https://doi.org/10.1017/9781009157896.011.

[73] A. Orsi, G. Johnson, and J. Bullister. Circulation, mixing, and production of antarctic bottom water. *Progress in Oceanography*, 43(1):55–109, 1999. doi: https://doi.org/10.1016/S0079-6611(99)00004-X.

[74] T. Osborn. Dissipation measurements of oceanic turbulence. In J. C. Nihoul, editor, *Marine Turbulence*, volume 28, pages 143–155. Elsevier, 1980. doi: https://doi.org/10.1016/S0422-9894(08)71218-2.

[75] J. Pedloski. Fluctuating winds and the ocean circulation. *Tellus*, 19(2):250–257, 1967. doi: https://doi.org/10.1111/j.2153-3490.1967.tb01480.x.

[76] R. Pingree and B. Le Cann. Structure of a meddy (bobby 92) southeast of the azores. *Deep Sea Res. Part I Oceanogr. Res. Pap.*, 40(10):2077–2103, 1993. doi: https://www.sciencedirect.com/science/article/pii/0967063793900466.

[77] J. Price and M. Baringer. Outflows and deep water production by marginal seas. *Prog. Oceanogr.*, 33(3):161–200, 1994. doi: https://www.sciencedirect.com/science/article/pii/0079661194900272.

[78] J. Price, M. Baringer, R. Lueck, G. Johnson, I. Ambar, G. Parrilla, A. Cantos, M. Kennelly, and T. Sanford. Mediterranean outflow mixing and dynamics. *Science*, 259 (5099):1277–1282, 1993. doi: https://www.science.org/doi/10.1126/science.259.5099.1277.

[79] J. Price, T. Sanford, C. Mauritzen, and P. Prater. Cruise report rrs discovery 247. a process study of the faroe bank channel overflow. *WHOI technical reports*, 44, 2000. doi: https://www.whoi.edu/science/PO/people/jprice/oflow/FBC.pdf.

[80] J. F. Price and M. A. Sundermeyer. Stratified ekman layers. *Journal of Geophysical Research: Oceans*, 104(C9):20467–20494, 1999. doi: https://doi.org/10.1029/1999JC900164.

[81] S. G. Purkey, G. C. Johnson, L. D. Talley, B. M. Sloyan, S. E. Wijffels, W. Smethie, S. Mecking, and K. Katsumata. Unabated bottom water warming and freshening in the south pacific ocean. *Journal of Geophysical Research: Oceans*, 124(3):1778–1794, 2019. doi: https://doi.org/10.1029/2018JC014775.

[82] M. Rebesco, F. Hernández-Molina, D. Van Rooij, and A. Wåhlin. Contourites and associated sediments controlled by deep-water circulation processes: State-of-the-art and future considerations. *Marine Geology*, 352:111–154, 2014. doi: https://doi.org/10.1016/j.margeo.2014.03.011.

[83] C. Ross. Temperature–salinity characteristics of the "overflow" water in denmark strait during "overflow'73". *Rapp. PV Reun. Cons. Int. Explor. Mer*, 185:111–119, 1984.

[84] S. Rétif, M. Negretti, and A. Wirth. Predicting the vertical density structure of oceanic gravity current intrusions. *Scientific Reports*, 14, 2024. doi: 10.1038/s41598-024-60878-x.

[85] P. Saunders. Cold outflow from the faroe bank channel. *Journal of Physical Oceanography*, 20(1):29 – 43, 1990. doi: 10.1175/1520-0485(1990)020⟨0029:COFTFB⟩2.0.CO;2.

[86] P. Saunders. Combining hydrographic and shipborne adcp measurements. *Deep Sea Research Part A. Oceanographic Research Papers*, 39(7):1417–1427, 1992. doi: https://doi.org/10.1016/0198-0149(92)90077-7.

[87] F. Schott and J. McCreary. The monsoon circulation of the indian ocean. *Progress in Oceanography*, 51(1):1–123, 2001. doi: https://doi.org/10.1016/S0079-6611(01)00083-0.

[88] J. Seabrooke, G. Hufford, and R. Elder. Formation of Antarctic bottom water in the Weddell Sea. *Journal of Geophysical Research*, 76(9):2164–2178, 1971. doi: 10.1029/JC076i009p02164.

[89] G. I. Shapiro and A. E. Hill. Dynamics of dense water cascades at the shelf edge. *J. Phys. Oceanogr.*, 27(11):2381 – 2394, 1997. doi: https://doi.org/10.1175/1520-0485(1997)027⟨2381:DODWCA⟩2.0.CO;2.

[90] J. O. Shin, S. B. Dalziel, and P. F. Linden. Gravity currents produced by lock exchange. *Journal of Fluid Mechanics*, 521:1–34, 2004. doi: 10.1017/S002211200400165X.

[91] D. A. Smeed, S. A. Josey, C. Beaulieu, W. E. Johns, B. I. Moat, E. Frajka-Williams, D. Rayner, C. S. Meinen, M. O. Baringer, H. L. Bryden, and G. D. McCarthy. The north atlantic ocean is in a state of reduced overturning. *Geophysical Research Letters*, 45(3):1527–1533, 2018. doi: https://doi.org/10.1002/2017GL076350.

[92] P. Smith. A streamtube model for bottom boundary currents in the ocean. *Deep Sea Research and Oceanographic Abstracts*, 22(12):853–873, 1975. doi: https://doi.org/10.1016/0011-7471(75)90088-1.

[93] P. Smith. Experiments with viscous source flows in rotating systems. *Dynamics of Atmospheres and Oceans*, 1(3):241–272, 1977. doi: https://doi.org/10.1016/0377-0265(77)90009-4.

[94] K. Snow, A. Hogg, B. Sloyan, and S. Downes. Sensitivity of antarctic bottom water to changes in surface buoyancy fluxes. *Journal of Climate*, 29:151023105856005, 2015. doi: 10.1175/JCLI-D-15-0467.1.

[95] D. Sous, J. Sommeria, and D. Boyer. Friction law and turbulent properties in a laboratory ekman boundary layer. *Physics of Fluids*, 25(4):046602, 2013. doi: https://doi.org/10.1063/1.4802045.

[96] M. Spall. Dynamics of downwelling in an eddy-resolving convective basin. *Journal of Physical Oceanography*, 40(10):2341 – 2347, 2010. doi: 10.1175/2010JPO4465.1.

[97] J. Swallow. A deep eddy off cape st vincent. *Deep-Sea Research*, 16:285–295, 1969.

[98] A. Tassigny, M. Negretti, and A. Wirth. On the turbulent structures generated by intruding and rotating downslope gravity currents. *Phys. Rev. Fluids*, page 15, 2023.

[99] A. Tassigny, M. Negretti, and A. Wirth. Dynamics of intrusion in downslope gravity currents in a rotating frame. *Physical Review Fluids*, 9, 2024. doi: 10.1103/PhysRevFluids.9.074605.

[100] J. Taylor and S. Sarkar. Direct and large eddy simulations of a bottom ekman layer under an external stratification. *International Journal of Heat and Fluid Flow*, 29(3):721–732, 2008. doi: https://doi.org/10.1016/j.ijheatfluidflow.2008.01.017.

[101] S. Thorpe and G. Deacon. Turbulence and mixing in a scottish loch. *Philosophical Transactions of the Royal Society of London. Series A, Mathematical and Physical Sciences*, 286(1334):125–181, 1977. doi: 10.1098/rsta.1977.0112.

[102] J. H. Trowbridge and S. J. Lentz. Asymmetric behavior of an oceanic boundary layer above a sloping bottom. *Journal of Physical Oceanography*, 21(8):1171 – 1185, 1991. doi: 10.1175/1520-0485(1991)021⟨1171:ABOAOB⟩2.0.CO;2.

[103] L. Umlauf and L. Arneborg. Dynamics of rotating shallow gravity currents passing through a channel. part i: Observation of transverse structure. *Journal of Physical Oceanography - J PHYS OCEANOGR*, 39, 2009. doi: 10.1175/2009JPO4159.1.

[104] L. Umlauf and L. Arneborg. Dynamics of rotating shallow gravity currents passing through a channel. part ii: Analysis. *Journal of Physical Oceanography - J PHYS OCEANOGR*, 39, 2009. doi: 10.1175/2009JPO4159.1.

[105] L. Umlauf, W. D. Smyth, and J. N. Moum. Energetics of bottom ekman layers during buoyancy arrest. *Journal of Physical Oceanography*, 45(12):3099 – 3117, 2015. doi: 10.1175/JPO-D-15-0041.1.

[106] M. Ungarish. On the spinup and spreadout of a cartesian gravity current on a slope in a rotating system. *J. Fluid Mech*, 943:A31, 2022. doi: https://doi.org/10.1017/jfm.2022.447.

[107] H. van Haren and L. Gostiaux. Detailed internal wave mixing above a deep-ocean slope. *Ocean Sci.*, 2012. doi: https://api.semanticscholar.org/CorpusID:131159153.

[108] W. Von Appen, D. Mastropole, R. Pickart, H. Valdimarsson, S. Jónsson, and J. Girton. On the nature of the mesoscale variability in denmark strait. *Journal of Physical Oceanography*, 47(3):567 – 582, 2017. doi: 10.1175/JPO-D-16-0127.1.

[109] T. Von Kármán. The engineer grapples with nonlinear problems. *Bulletin of the American Mathematical Society*, 46(8):615 – 683, 1940.

[110] A. Wåhlin and G. Walin. Downward migration of dense bottom currents. *Environ. Fluid Mech.*, 1:257–279, 2001. doi: https://doi.org/10.1023/A:1011520432200.

[111] G. Walin. Some aspects of time-dependent motion of a stratified rotating fluid. *Journal of Fluid Mechanics*, 36(2):289–307, 1969. doi: 10.1017/S0022112069001662.

[112] G. Weatherly and P. Martin. On the structure and dynamics of the oceanic bottom boundary layer. *Journal of Physical Oceanography*, 8(4):557 – 570, 1978. doi: 10.1175/1520-0485(1978)008⟨0557:OTSADO⟩2.0.CO;2.

[113] A. Wirth. On the basic structure of oceanic gravity currents. *Ocean Dyn.*, 59(4):551–563, 2009. doi: https://doi.org/10.1007/s10236-009-0202-9.

[114] A. Wirth. Laminar and weakly turbulent oceanic gravity currents performing inertial oscillations. *Ocean Sci.*, 8(3):301–317, 2012. doi: https://os.copernicus.org/articles/8/301/2012/.

[115] A. Wirth. A guided tour through physical oceanography. Lecture, Jan. 2015. URL `https://hal.science/cel-01134110`.

[116] A. Wirth and M. Negretti. Intruding gravity currents and their recirculation in a rotating frame: Numerical results. *Ocean Modelling*, 173:101994, 2022. doi: https://doi.org/10.1016/j.ocemod.2022.101994.

[117] L. Worthington. An attempt to measure volume transport of norwegian sea overflow water through denmark strait. *Deep-Sea Research*, page 421, 1969.

[118] L. Worthington. The norwegian sea as a mediterranean basin. *Deep Sea Research and Oceanographic Abstracts*, 17(1):77–84, 1970. doi: https://doi.org/10.1016/0011-7471(70)90088-4.

[119] C. Wunsch. A simplified ocean physics? revisiting abyssal recipes. *J. Phys. Oceanogr.*, 53(5):1387 – 1400, 2023. doi: https://journals.ametsoc.org/view/journals/phoc/53/5/JPO-D-22-0229.1.xml.

[120] X. Xie, Y. Wang, Z. Liu, X. Liu, D. Chen, D. Zhang, and J. Wang. Observation of near-inertial waves in the bottom boundary layer of an abyssal seamount. *Journal of Physical Oceanography*, 53(2):635 – 645, 2023. doi: 10.1175/JPO-D-22-0026.1.

[121] C. Yin. *Dynamics of Nonhomogeneous Fluids*. Macmillan Series in Advanced Mathematics and Theoretical Physics, 1965.

[122] S. Zhou, A. Meijers, M. Meredith, E. Abrahamsen, P. Holland, A. Silvano, J. Sallée, and S. Østerhus. Slowdown of antarctic bottom water export driven by climatic wind and sea-ice changes. *Nature Climate Change*, 2023. doi: 10.1038/s41558-023-01695-4.